REFLECTION SPECTROSCOPY OF METAL SURFACES

THESIS SUBMITTED TO THE UNIVERSITY OF LONDON
FOR THE DEGREE DOCTOR OF PHILOSOPHY

by

Laurence.S.Julien B.Sc.

April 1973

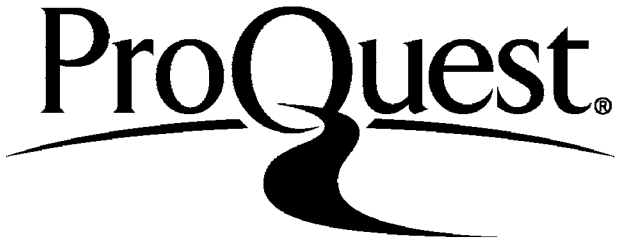

ABSTRACT

New techniques have been developed for the analysis of reflection data obtained from metal surfaces. An optimization study has been carried out and it has been shown that for n and k values observed for metals optimization becomes critical. Optimized reflection techniques have been used in experimental studies on terbium and gadolinium films prepared in ultra high vacuum, and the resulting optical conductivity curves are shown to be in good agreement with the predictions of a simple theory based on interband optical transitions.

INTRODUCTORY REMARKS

The overall objective of the work described here was to gain information about the electronic band structures of the rare earth metals, terbium and gadolinium. The theoretical importance of these metals is discussed in Chapter VI. It was decided to use optical techniques for this study as these can yield, directly, energy absorption coefficients for incident photons of known energy. The way in which optical studies relate to the electronic band structures of metals is described in Chapter I. The studies were made in reflection so that properties characteristic of the bulk metals could be observed. (Transmission studies require thin film samples.) The analysis of reflection data is discussed in Chapters II and III and the results of these chapters form the basis of the design of reflectometer systems described in Chapter IV. The results of optical studies on terbium and gadolinium are given in Chapter VI and these are interpreted in terms of recent energy band structure calculations. Chapter VII describes some work on copper and gold; this work is of a somewhat tentative nature and was performed largely as a control for the more important work on the rare earths. Chapter V is devoted to a description of the techniques used in the preparation of samples suitable for optical studies.

CONTENTS

CHAPTER III

CHAPTER IV

CHAPTER VI (Contd.)

CHAPTER VII

CHAPTER VIII

CHAPTER I

THE ROLE OF OPTICAL CONSTANT DETERMINATIONS IN SOLID STATE PHYSICS

1.1. Introduction

This work will be primarily concerned with the behaviour of light waves incident on a vacuum-metal interface. Maxwell's electromagnetic theory of light provides the basis of an understanding of such an interaction, and one of the most remarkable results of Maxwells theory may be expressed in the following relationship for a non magnetic medium:-

$$n = \sqrt{\epsilon} \quad - - - - - - - - (1)$$

ϵ is the dielectric constant of the medium and n is the refractive index defined as the ratio of the velocity of light in the medium to the velocity of light in vacuum.

The quantity ϵ is a material constant so that equation (1) provides a relationship between the behaviour of light in a medium and a property of that medium. This is of fundamental importance; we know that ϵ must be related to the electronic properties of the medium, therefore a study of the propagation of light in a medium should ultimately lead to information about those properties. The phenomenon of optical dispersion shows immediately that ϵ , and therefore n, is frequency dependent. Application of Maxwell's equations to a conducting medium further shows that n must, in general, be a complex quantity. In principle a knowledge of the refractive index of a material is

sufficient to define the subsequent behaviour of a light wave incident on that material. We shall therefore be concerned with the frequency dependence of the complex refractive index. If the refractive index of a system can be calculated from a model of that system, then an incident light wave may be used as a probe to test the validity of that model, and possibly to obtain measurements of some of the parameters used in constructing the model.

1.2. Definition of Optical Constants

From the outset we assume the metal to be homogeneous, isotropic and linear in its response to electro-magnetic waves. Justification of the isotropy assumption will be given where necessary. A light wave incident on a vacuum-metal interface undergoes two changes on transmission: the wave velocity changes, and the electric amplitude is attenuated. These two effects are broadly characterized by the quantities n (real part of refractive index which is often referred to as simply "refractive index") and k (extinction coefficient) which emerge when Maxwell's equations are applied to a system having non-zero electrical conductivity. In such a system the alternating electric vector will produce an electric current other than the displacement current.

Within the framework of the assumptions given in 1.2. the current will be described by an equation of the form:-

$$j = \sigma(\omega) E_0 \exp(i\omega t) \text{ - - - - - - (2)}$$

where:-

$\sigma(\omega)$ = The frequency dependent conductivity.

E_o = The electric amplitude of the incident wave.

ω = The angular frequency of the incident wave.

It is desirable to obtain a relationship between $\sigma(\omega)$ and the quantities n and k, since this will in principle enable one to explore electronic behaviour via the observable optical parameters.

If we arbitrarily define the spatial and temporal origins x = o and t = o respectively, we can represent a plane wave incident on the vacuum-metal interface by:-

$$E = E_o \exp i\omega\left\{t - \frac{x}{c}\right\} \quad \text{---(3)}$$

The transmitted wave can be completely described by:-

$$E = E_o \exp i\omega t \exp -\frac{i\omega n x}{c} \exp -\frac{k\omega x}{c} \quad \text{---(4)}$$

Where:-

n = c/v,

k is a constant

and v = velocity of light in the metal.

k clearly gives a measure of spatial attenuation within the medium. We can therefore write:-

$$E = E_o \exp i\left\{\omega t - \frac{\omega x \hat{n}}{c}\right\} \quad \text{---(5)}$$

where:

$$\hat{n} = n - ik \quad (6)$$

n is defined to be the complex refractive index of the metal.

n and k are referred to collectively as the optical constants of the medium.

Other definitions of complex refractive index are sometimes used, for example:-

$$\hat{n} = n(1 - ik)$$

$$\hat{n} = n + ik$$

The relationships between optical constants based on the different definitions of n and k are simple, but some standardization would seem desirable. Throughout this work the definition stated in equation (6) will be used, since this seems, from a survey of the literature, to be gaining ascendancy over other definitions.

1.3. Optical Conductivity and Absorption Coefficient

From electromagnetic theory it can be shown that:- (Mott and Jones 1936)

$$\frac{\text{Rate of loss of energy/unit volume}}{\text{Square of Electric vector}} = nk\nu$$

where:-

ν = frequency of incident radiation.

By analogy with the flow of direct electric current we see that the quantity:-

$$nk\nu = \sigma(\nu)$$

can be appropriately called the optical conductivity.

Furthermore, the absorption coefficient of the medium can be shown to be:-

$$2nk/\lambda$$

Thus the optical conductivity is directly proportional to absorption coefficient and both give a measure of the capacity of the metal to absorb energy at the frequency ν .

At this stage we note that the quantity $(n^2 - k^2)$ forms the real part of the dielectric constant. If $(n^2 - k^2) < 0$ for a medium then an electromagnetic wave cannot propagate in that medium and the optical behaviour is said to be "metallic".

1.4. Classical Models for the Calculation of Optical Constants

Thus far the discussion has been based on purely phenomenological electromagnetic theory. In order to obtain information about the electronic properties of the material a detailed microscopic analysis of the interaction between electromagnetic waves and electrons in a solid is required. Lorentz (1906) carried out a classical analysis of the optical properties of dielectrics. Drude (1900) carried out the first analysis for metals. Classical calculations determine the quantities 2nk and $(n^2 - k^2)$ directly. Drude suggested that the optical properties of metals might be explained by assuming the existence of a free electron gas moving through ions which form the crystal lattice of the material. An applied electric field accelerates the electrons which are impeded by collisions with the lattice ions. The motion of an electron can then be described by a mean drift velocity $\bar{v}$ and a relaxation time τ . This theory

allows a calculation of the optical conductivity as a function of frequency:-

$$\sigma(\omega) = \frac{\sigma(0)}{1 + \omega^2\tau^2} \quad ---(7)$$

where $\sigma(0)$ is the d.c. conductivity

Equation (7) may be expected to hold under conditions such that the mean free path, defined as the quantity $\bar{v}\tau$, is short compared with the wavelength of the incident light.

This equation is therefore most often used in the infra-red region of the spectrum and is useful when a low energy extrapolation is required for use with the dispersion relationships developed by Kramers and Kronig, and described by Landau and Lifshitz (1960). The free electron theory predicts that the quantities $(n^2 - k^2)$ and $2nk$ are linearly related. A Plot of these quantities on an Argand diagram gives a useful indication of the validity of the Drude theory and in addition an estimate of the quantity τ . The high frequency limit of applicability of the Drude theory has formed the major interest in a large volume of experimental work, of which that performed by Bennet et al (1963) is typical. The free electron theory was used by Zener (1933) to explain the transparency of the alkali metals to ultra-violet radiation. This work allows an estimate to be made of the frequency at which the onset of collective oscillations of electrons occurs (the plasma frequency ω p).

1.5. Calculations of Electronic Band Structure

Although successful in many respects, the above theory takes no account of the quantum mechanical absorption processes which are known to be intimately involved in the photon-electron interactions within the metal. More realistic calculations require the use of the band model of electrons in solids. The electronic band structure describes the energy-momentum relationship of electrons in a material in terms of the distribution of their wave vectors throughout the reciprocal lattice of the crystal structure of that material. The calculation of electronic band structures is very much a specialist task and the techniques employed have been reviewed by Pincherle (1960) Harrison (1970) and Kittel (1963). The calculations are necessarily approximate since the results will depend on many-body effects and these must be handled in an average sense. In order that the calculations remain tractable, the energy-momentum relationships are calculated along lines, and at points, of high symmetry in the reciprocal lattice. Considerable limitations are then placed on the form of the eigenstates by group theoretical considerations. The problem may then be considered in two parts. The Hamiltonian for an electron is constructed ideally, containing a potential representing the effect of all the electrons in the material, including exchange effects. The next part of the calculation involves the solution of the resulting Schrödinger equation. A self consistent approach is necessary since, in order to calculate the exchange interactions to be included in the potential,

a knowledge of the states to be determined is required, and the potential is in turn needed to calculate the states. The way in which the final computed states depend on the initially assumed form of potential is not well understood and at this point an appeal to experiment is useful. Any experiment, the interpretation of which depends on the electronic band structure of the material, may be ultimately considered a test of the potential used for the calculation of the band structure. Bloch's theorem allows the calculations to be restricted to the unit cell of the reciprocal lattice, often called the Brillouin zone. The notation used most frequently for the description of symmetry points and lines in the Brillouin zone is that used by Bouckaert, Smoluchowski and Wigner (1936). Figure (1) shows the reciprocal lattices for the face centred cubic and hexagonal close packed crystal structures, with symmetry points and lines according to the above notation. Calculations have been carried out for a large number of crystalline solids, but these have been largely restricted to symmetry directions and points. This deficiency may be important when considering the optical properties of solids.

1.6. Interpretation of Optical Data in Terms of Electronic Band Structure

A very general expression relates the optical conductivity to the electron states throughout the Brillouin zone (Kubo 1957), (Greenwood 1958). In general we do not know all these states, and

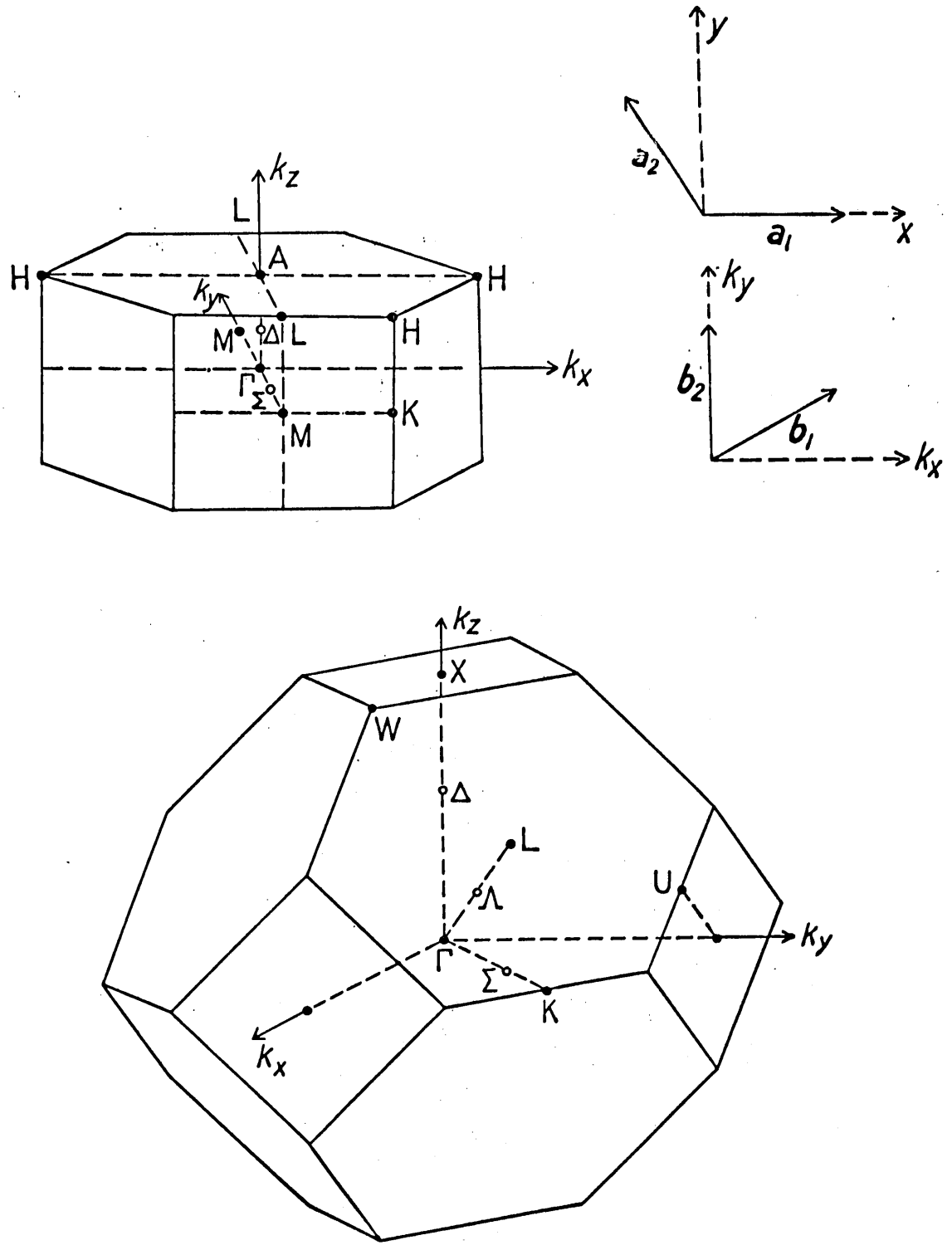

Figure 1. Labelled first Brillouin zones for the f.c.c. and h.c.p. lattices.

any experimental results depend strongly on the properties of the optical surface and other effects not accounted for in the Kubo-Greenwood furmula. For these reasons it is not considered worthwhile to attempt comparisons between experimental data and the Kubo-Greenwood formula. The experimentally determined numerical values of optical constants n and k are probably most useful for comparison purposes, to give an indication of specimen surface conditions. At this point it must be mentioned that optical constants determined by different observers are not generally in good numerical agreement. Of greater interest is the shape of the optical conductivity dispersion curve which ought to be interpretable in terms of the electronic band structure of the material. We expect from symmetry considerations that electron transitions will occur vertically in the Brillouin zone and such transitions will cause an increase in the optical conductivity. We would expect pronounced structure in the optical dispersion curve to occur at energies for which there exists a high joint density of states between bands, i.e. where bands are parallel. We know from symmetry conditions that the bands will be flat at symmetry interband points (Peierls 1955) so that they must be parallel at these points. Thus it is reasonable to assume that the energy at which structure occurs in an optical conductivity dispersion curve is likely to correspond to an energy gap at a symmetry interband point.

The assignment of observed structure to calculated band gaps is always somewhat tentative in the absence of independent experimental data, e.g. De Haas-Van-Alphen effect and photo-emission data. At present it is often found that the above procedure is incapable of completely describing the optical properties of materials and it may be necessary to consider effects which are not included in the band calculations. Clearly, transitions may occur in regions of the Brillouin zone for which calculations have not been performed. Non-vertical transitions are possible via phonon creation, or electron-electron interactions not included in the band structure calculation. The effect of the surface may be important in so far as it can effectively absorb momentum and allow non vertical transitions. The effects of impurity centres and lattice faults have not been considered in this context. It has been suggested by Blodgett and Spicer (1966) that the optical absorption of nickel can be explained almost entirely in terms of non-vertical electron transitions. This would involve the use of an equation of the form:-

$$nk\omega = \frac{B}{\omega} \int_{E_f}^{E_f + \hbar\omega} N_c(E)\, N_v(E - \hbar\omega)\, dE \quad \text{-----} \quad (8)$$

where:-

B = an arbitary constant

and $N_c(E)$ and $N_v(E - \hbar\omega)$ are the density of states in the conduction and valence bands respectively.

This view has not gained wide acceptance however, and attempts by Shiga and Pells (1969) to interpret optical data using (8) were unsuccessful. The view adopted here in interpreting experimental results will be that the general shape of the optical absorption curve may be determined by one or more of the above-mentioned non-k-conserving processes, whereas any structure superimposed on this 'background' is likely to be due to transitions at symmetry interband points.

CHAPTER II

THE DETERMINATION OF OPTICAL CONSTANTS FROM REFLECTANCE MEASUREMENTS

2.1. Introduction

Optical constants may be deduced from various sets of experimental observables. In this chapter we are concerned primarily with determining optical constants by measuring changes in light intensity on reflection from a surface. Other common methods involve the changes in polarisation on reflection (ellipsometry) or changes in the light wave on transmission (restricted to thin films) and these methods have been recently reviewed by Taylor (1972). The reflectance method has been chosen for a detailed study because recent work has made it computationally the most convenient. In addition it is more suited to the determination of optical constants of materials maintained in a vacuum system than are ellipsometric determinations where strain effects in the entrance and exit windows become important.

2.2. The Fresnel Reflectance Equations

The reflection coefficients $R_{\perp}$ and $R_{\parallel}$ may be defined as follows. $R_{\perp}$ for a surface at a wavelength λ is the ratio of the intensity of an electromagnetic wave reflected from that surface to the intensity of the incident wave having its E-vector

perpendicular to the plane of incidence. $R_{//}$ is similarly defined for an incident wave with its E-vector parallel to the plane of incidence. These reflection coefficients can be expressed in terms of the optical constants n and k, and θ , the angle of incidence. The resulting relationships are called the Fresnel reflectance equations. Prior to 1969 it had not been possible to solve these equations to yield n and k explicitly in terms of $R_{\perp}$, $R_{//}$ and θ . Querry (1969) achieved such a solution as follows:- Making the substitutions:-

$$F = \frac{R_{\perp} + 1}{R_{\perp} - 1} \qquad (1)$$

$$G = \frac{R_{//} + 1}{R_{//} - 1} \qquad (2)$$

and putting

$$Q = \frac{(F - G) \sin\theta \cot 2\theta}{GF + (1 - F^2) \cos^2\theta - 1} \qquad (3)$$

$$P^2 = Q^2 - 2FQ \cos\theta - \cos^2\theta \qquad (4)$$

into the Fresnel reflectance equations written in the form:-

$$R_{\perp} = \frac{(Q - \cos\theta)^2 + P^2}{(Q + \cos\theta)^2 + P^2} \qquad (5)$$

$$R_{//} = R_{\perp} \frac{(Q - \sin\theta \tan\theta)^2 + P^2}{(Q + \sin\theta \tan\theta)^2 + P^2} \qquad (6)$$

then:-

$$Q^2 - P^2 = n^2 - k^2 - \sin^2\theta \qquad (7)$$

$$Q P = n k \qquad (8)$$

F and G are functions of $R_\perp$ and $R_{//}$ only. Thus P and Q can be calculated for a given θ and by substituting in (7) and (8) n and k may be found. Clearly, as $\theta \to 45^\circ$ $\text{Cot}2\theta \to 0$ and therefore $Q \to 0$ and the solution fails.

2.3. The Regions in ($R_\perp$, $R_{//}$) Space for which Real Solutions to the Fresnel Equations Exist.

At normal incidence $R_\perp \equiv R_{//}$. Thus at $\theta = 0$ all solutions to the Fresnel reflectance equations must lie on a straight line in ($R_\perp$, $R_{//}$) space. The following analysis shows that, at general angles of incidence, solutions are restricted to bounded regions in ($R_\perp$, $R_{//}$) space.

Equation (3) shows Q to be a real quantity. Therefore, for real n and k, from equation (8) we see that P must be real. It follows that real solutions to the Fresnel equations are obtained if, and only if, $P^2 > 0$. The condition $P^2 = 0$ delineates a boundary outside which no real solutions to the reflectance equations exist. It is readily shown that on one side of the boundary P is in fact imaginary and that $P^2 = 0$ is not a zero minimum. Substituting for Q from (3) into (4) we get:-

$$P^2 = -\left(\frac{(F - G)\,\text{Sin}\,\theta\,\text{Cot}2\theta}{GF + (1 - F^2)\,\text{Cos}^2\theta - 1}\right)^2 - \frac{2F\,\text{Cos}\,\theta\,(F - G)\,\text{Sin}\,\theta\,\text{Cot}2\theta}{GF + (1 - F^2)\,\text{Cos}^2\theta - 1} - \text{Cos}^2\theta \qquad (9)$$

Rearranging:-

$$P^2 = G^2\{\sin^2\theta \cot^2 2\theta + F^2 \cos\theta (\cos\theta - 2\sin\theta \cot 2\theta)\}$$
$$+ G[2F\cos\theta(\cos\theta - \sin\theta\cot 2\theta)\{(1-F^2)\cos^2\theta - 1\}$$
$$+ 2F\sin\theta\cot 2\theta(F^2\cos\theta - \sin\theta\cot 2\theta)]$$
$$+ F^2\sin^2\theta\cot^2 2\theta + 2F^2\cos\theta\sin\theta\cot 2\theta$$
$$\{(1-F^2)\cos^2\theta - 1\} + \cos^2\theta\{(1-F^2)\cos^2\theta - 1\} \quad \text{——(10)}$$

Fortunately this equation simplifies to:-

$$P^2 = \{G^2\{\cot^2 2\theta + F\} - G[(1+\cot^2 2\theta)F - F^3]$$
$$+ F^2\{\sin^4\theta + \cos^4\theta + \cot^2 2\theta\}$$
$$+ \cos^2\theta\sin^2\theta(1+F^4)\}\sin^2\theta \quad \text{——————————} \quad (11)$$

Thus P^2 may be written

$$P^2 = aG^2 + bG + c \quad \text{——————————} \quad (12)$$

where a, b, and c are the functions of F and θ implied by equation (11)

The values of G for which $P^2 = 0$ may be calculated from equation (12) and the solutions when transformed, via equation (2), will bound the region for which all real n and k may be obtained. The boundaries generated in this way also represent the condition $k = 0$, since if

$$P^2 = \tfrac{1}{2}[\{(n^2 - k^2 - \sin^2\theta)^2 + 4n^2k^2\}^{\frac{1}{2}}$$
$$- (n^2 - k^2 - \sin^2\theta)] = 0 \quad \text{——————————} \quad (13)$$

then

$$4n^2k^2 = 0 \quad \text{——————————} \quad (14)$$

and therefore

$$k = 0 \quad \text{——————————} \quad (15)$$

i.e. the boundary values of $R_{\perp}$ and $R_{//}$ are those corresponding to perfect dielectrics. Figure (2) shows the boundaries for various angles of incidence. Figures (3) and (4) show the distribution of n and k values throughout the valid regions for $\theta = 16^{\circ}$ and $\theta = 74^{\circ}$. It was found that "bunching" of the n, k loci occurs near to the upper boundary for $0 < \theta < 45^{\circ}$ and near to the upper boundary for $45^{\circ} < \theta < 90^{\circ}$. This bunching is associated with high values of n, and arises from the rapid approach of Q to $+\infty$ as Q changes sign:

$$(Q^2)_{P^2 = 0} = n^2 - k^2 - \sin^2\theta \qquad (16)$$

If the $Q^2 > 0$ boundary is close to one of the $P^2 = 0$ conditions, then $k^2 \to 0$ in (15). For $(Q^2)_{P^2=0}$ to go to $+\infty$, n^2 must $\to +\infty$

2.4. Sensitivity of n and k to $R_{\perp}$ and $R_{//}$.

All points $(R_{\perp}, R_{//})$ for which there exist real n and k, are enclosed in the area defined by the $P^2 = 0$ condition transformed to the $(R_{\perp}, R_{//})$ plane. It is reasonable to assume that sensitive determinations of n and k are most likely to be made at angles of incidence for which the bounded regions have a maximum area. Numerical integration shows that maxima in area as a function of θ occur at $\theta = 16^{\circ}$ and $\theta = 74^{\circ}$. Empirical observation, rather than exact analysis, has previously indicated that a maximum in the sensitivity occurs for angles close to 70° (Humphreys-Owen 1961).

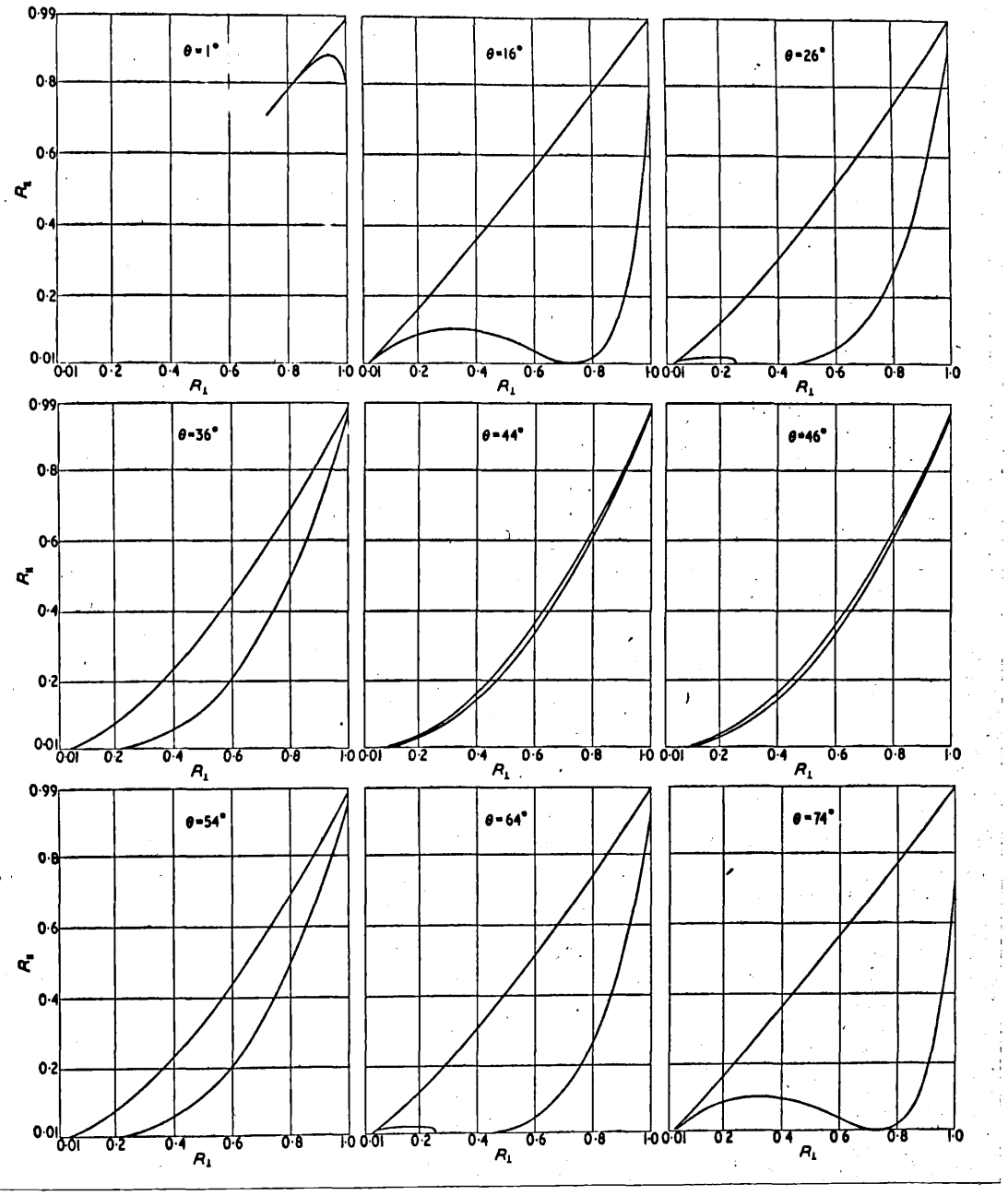

Figure 2. Bounded regions in $(R_{\perp}, R_{\parallel})$ space for various angles of incidence.

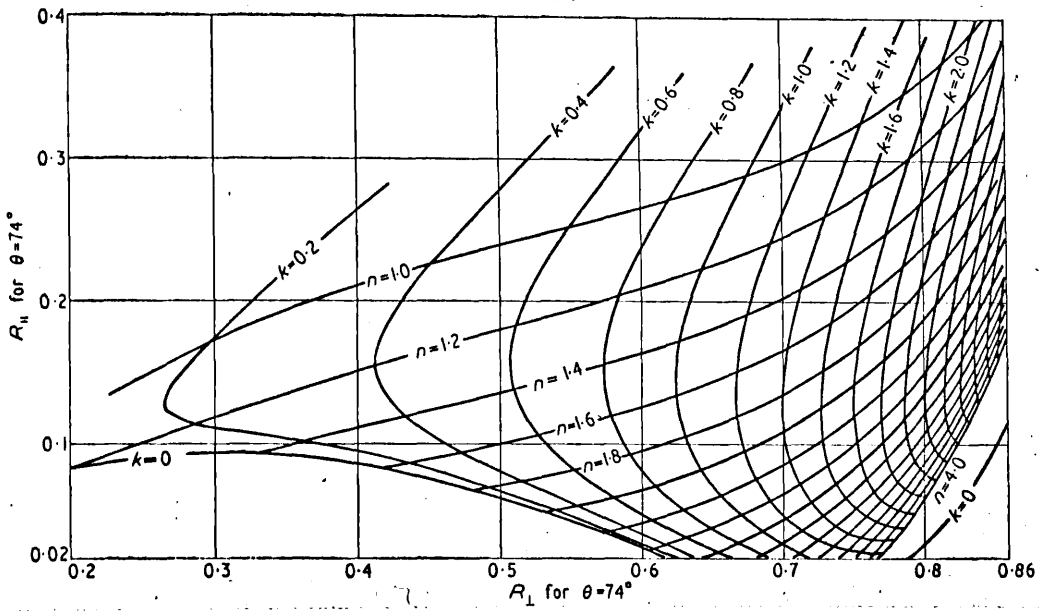

Figure 3. Distribution of (n,k) values for an angle of incidence of 74.

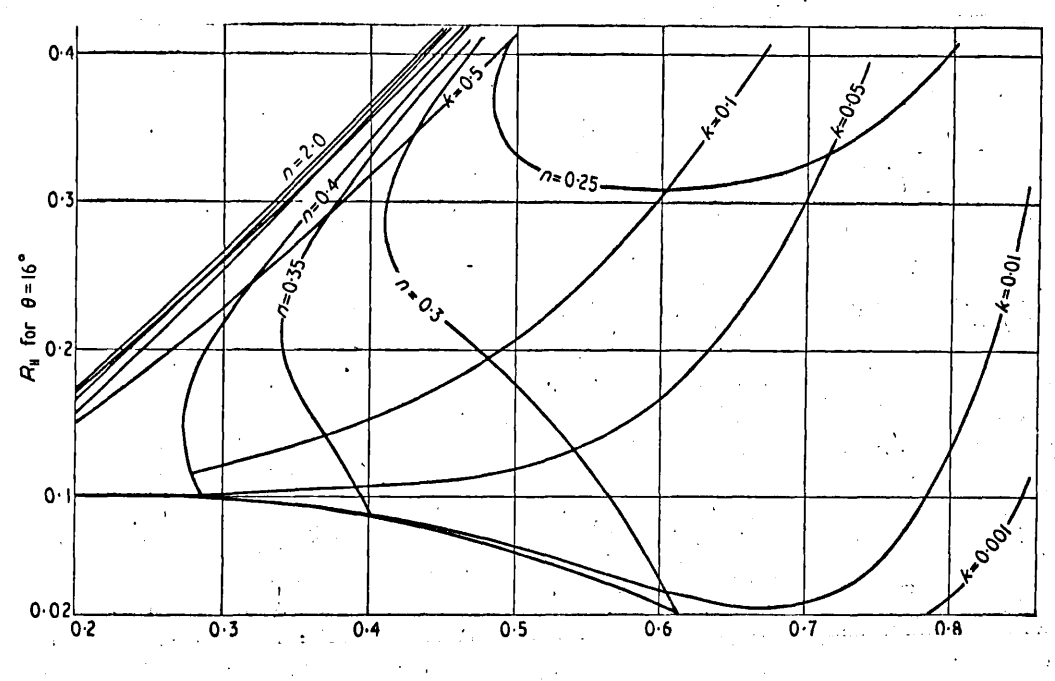

Figure 4. Distribution of (n,k) values for an angle of incidence of 16.

According to the above criterion, the optimum angles of incidence for determining optical constants from reflectance measurements are 16° and 74°. Inspection of figures (3) and (4) shows that for n and k values typical of most metals 74° is the better angle.

Clearly, since the distribution of (n, k) points varies with angle of incidence, it should not be expected that one angle of incidence should prove optimum for all combinations of n and k. Therefore a computer-based numerical technique was developed to investigate the sensitivity of the method in more detail.

2.5. Numerical Technique for Error Investigation

The basis of the method is illustrated in figure (5). This shows a typical region in $(R_{\perp}, R_{//})$ space. A point P within the bound region defines unique values of the optical constants (n_o, k_o) via the Fresnel reflectance equations. If there is an uncertainty $\pm\delta R$ in the reflection coefficients, then the extreme deviant values of optical constants will occur for points lying on the perimeter of a square of side $2\delta R$ drawn with P as the centre. These values are calculated at 400 equally spaced points on the perimeter. We assume $\delta R_{\perp} = \delta R_{//} = \delta R$ independent of $R_{\perp}$ and $R_{//}$. The product of the optical constants was chosen as a suitable parameter for the investigation because of its relevance to the electronic properties of materials. The fractional error in the product n k for a point on the square is given by:-

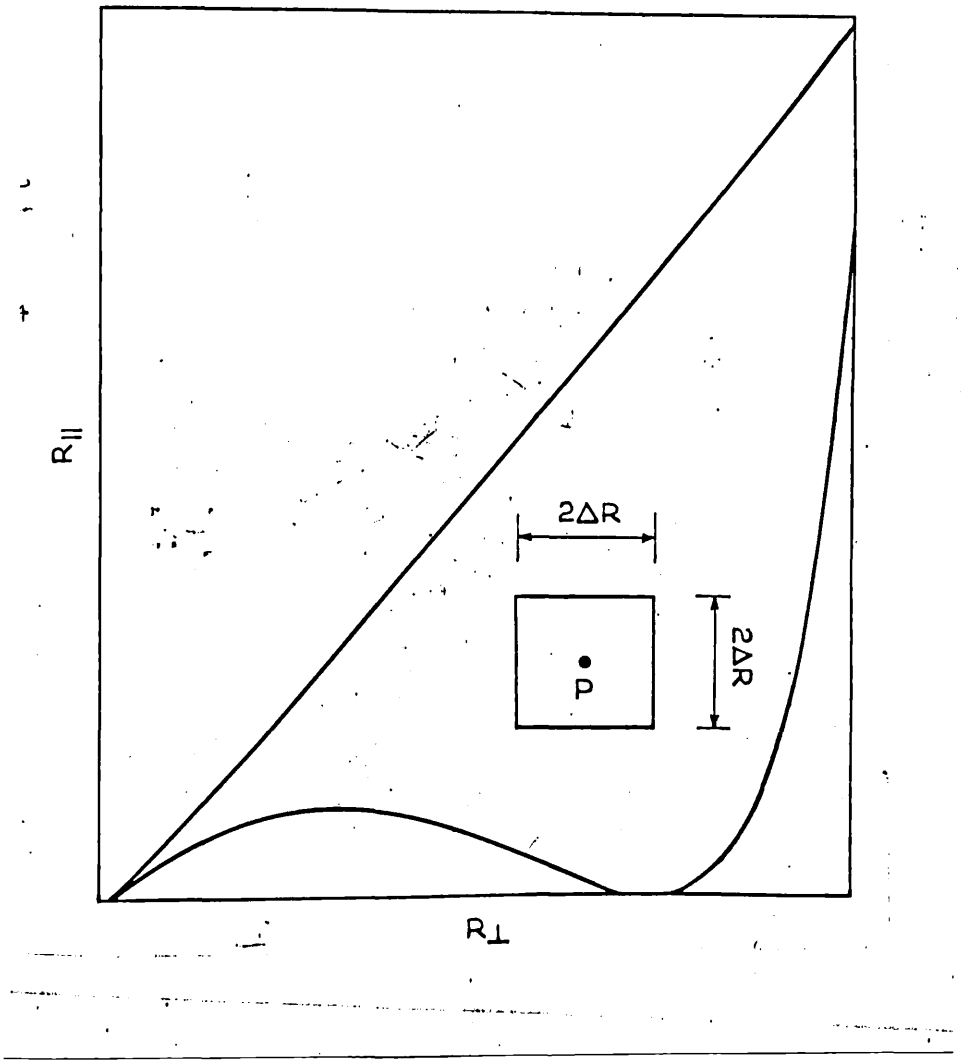

Figure 5.

$$\sigma = \frac{n_0 k_0 - nk}{n_0 k_0} \qquad (17)$$

Products nk for which σ took maximum positive and negative errors were determined using the technique described below. These values of σ represent the largest positive and negative errors resulting from uncertainties $\pm\delta R$ in the reflection coefficients.

2.6. The Computer Programme used for Error Investigation

The studies were carried out on the University of London C.D.C. 6600 Computer. The flow diagram of the computer programme used in this investigation is shown in figure (6). This programme relies on several subroutines. The subroutine called SOLVE uses the analytic solutions to the Fresnel equations as described in (2.2.) to return n and k for input parameters $R_\perp$, $R_{//}$ and θ. The subroutine called CHECK performs the reverse calculation (i.e. returns $R_\perp$ and $R_{//}$ for input parameters n, k and θ.) The subroutine called GENAT is called from the main programme and performs the search around a test square. This subroutine is shown in detail on the flow diagram and a listing is given in appendix (1).

2.7. Angular Dependence of σ.

The method described in the previous section was used to calculate σ for a large number of combinations n_0, k_0 in the range $1.0 \leq n \leq 4.0$ and $1.0 \leq k \leq 4.0$ and for angles of

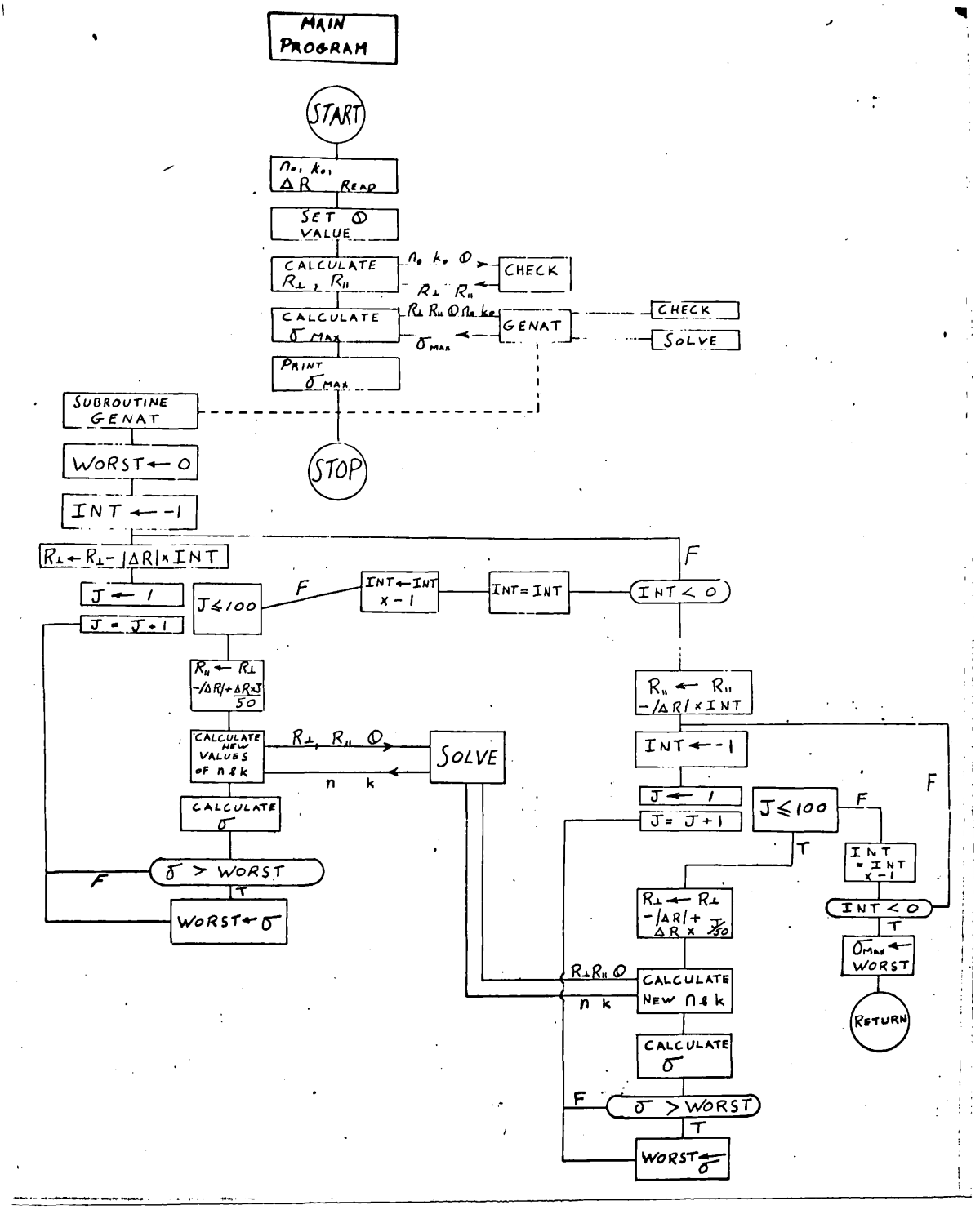

Figure 6. Flow diagram of computer search technique.

incidence in the range $0^\circ < \theta < 90^\circ$, $\theta \neq 45^\circ$. The values $n = 2.000$ and $k = 3.000$ were chosen to typify the results. (These values occur in subsequent studies made on the rare earth metals.) The point $n_0 = 2.000$ $k_0 = 3.000$ lies close to the upper boundaries in $(R_\perp , R_{//})$ space for $\theta < 45^\circ$ and close to the lower boundary $\theta > 45^\circ$ (see figures 3 and 4). Figure (7) shows the variation with θ of the largest positive and negative errors taken by the quantity σ with δR set at 0.00005. The two minima show that the general optimization criterion established in 2.4. is quite good. Figure (8) shows the results obtained using $\delta R = 0.001$ which represents a readily obtainable accuracy. The irregular behaviour of the negative portion of the curve can be associated with portions of the test square falling outside the valid region. The broadness of the minima at high angles of incidence indicates that near optimum conditions can be achieved simultaneously for quite a large range of n and k. For other values of optical constants the general shape of the variation of σ with θ remains the same but the size and position of the minima vary. Always, however, the minimum associated with the optimization is quite broad. The angles at which σ takes a minimum value for various (n, k) values is shown in figure (9). For (n, k) combinations in the range $1 \leq n \leq 4$ and $1 \leq k \leq 4$ the range of θ for optimization is only 10°. Figure (8) shows that a 10° shift from optimum θ will not greatly reduce the sensitivity of the method.

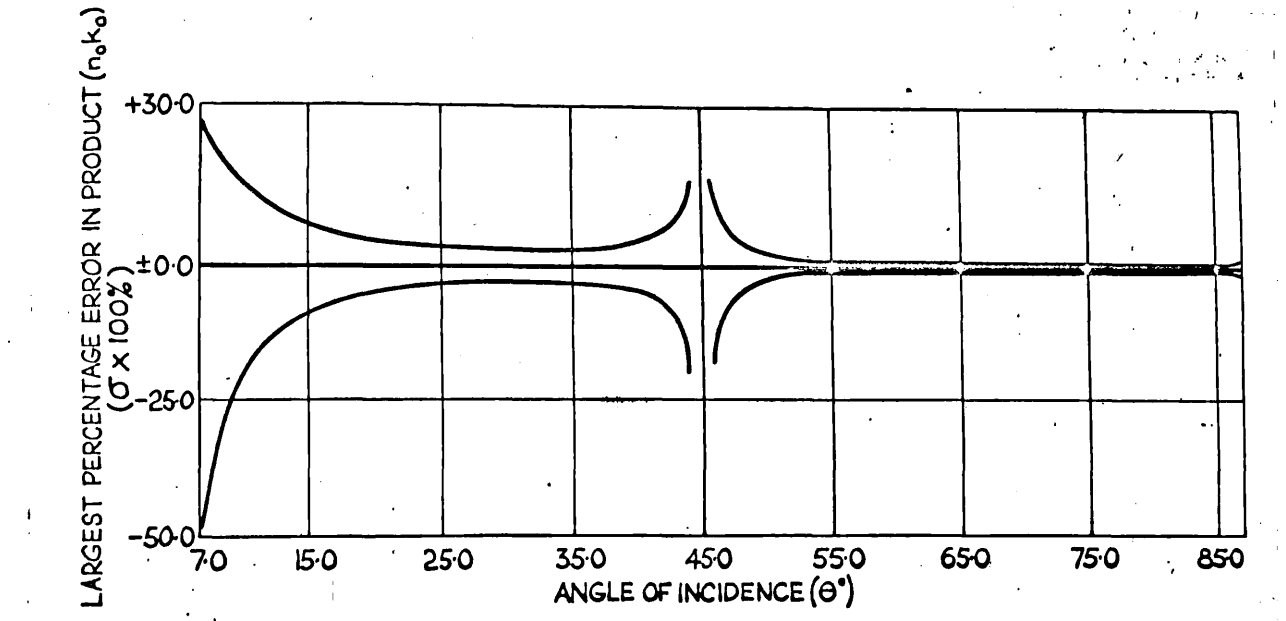

Figure 7. Largest percentage error in product (nk) as a function of angle of incidence with $\S$ R=0.00095

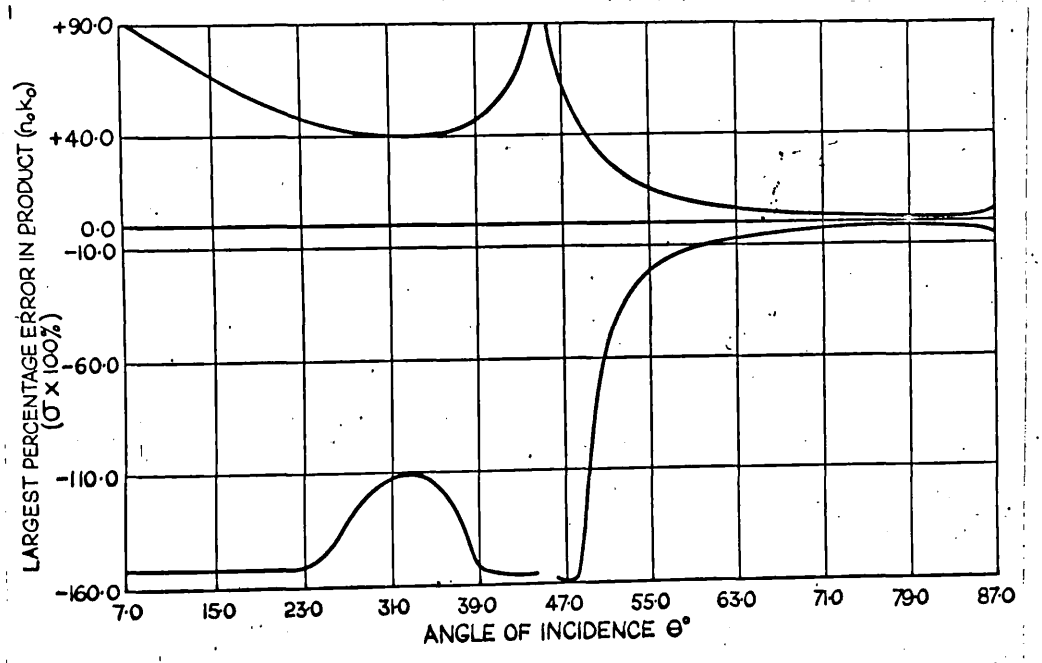

Figure 8. Largest percentage error in product (nk) as a function of angle of incidence with $\S$R=0.001

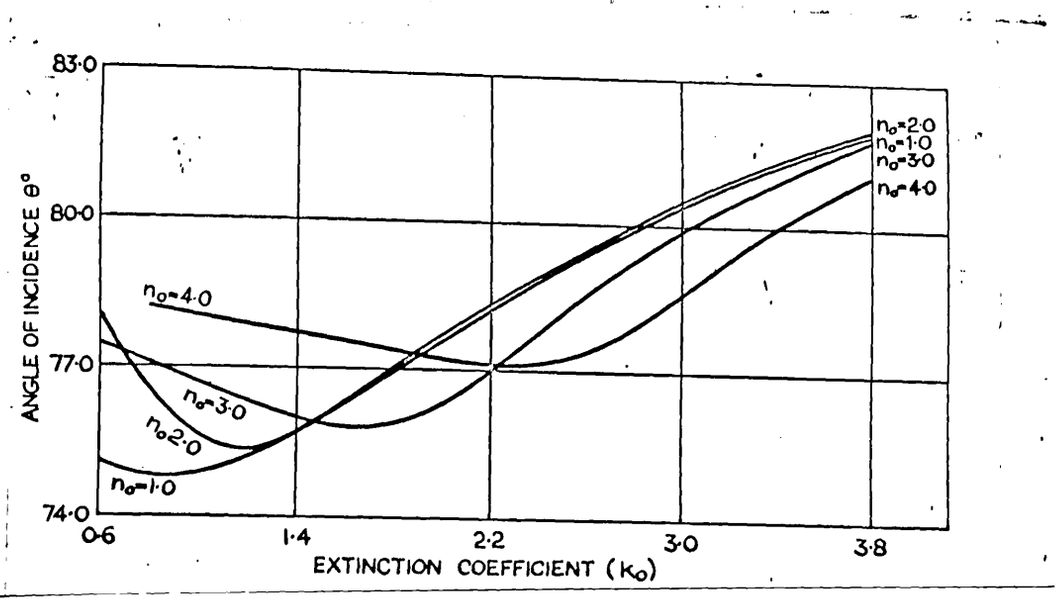

Figure 9. Optimum angles of incidence for various (n,k) combinations.

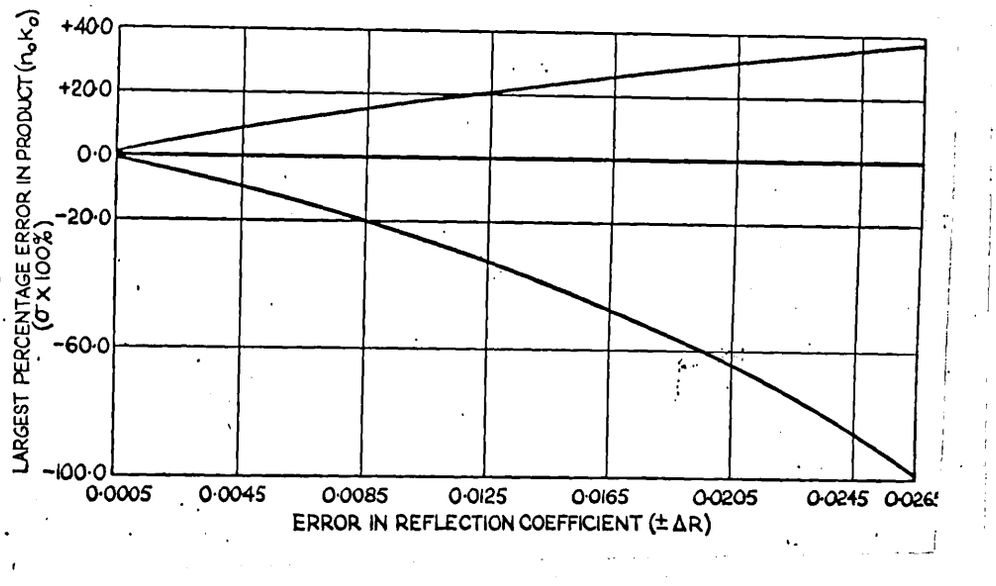

Figure 10. Variation of σ with δR.

2.8. Variation of σ with δR.

It was of practical interest to see how the value of varied with known errors δR in the two reflection coefficients. The results for n = 2.000 and k = 3.000 and $\theta = 74^\circ$ are shown plotted in figure (10.) For $\delta R < 0.005$ the curves are symmetrically placed about the line $\sigma = 0$ and σ varies linearly with δR. These features emerge for all (n, k) in the range $1 \leqslant n \leqslant 4$ and $1 \leqslant k \leqslant 4$, provided that the calculation is made for angles of incidence near to optimum value.

2.9. Precision of Angular Settings

It was also of interest to estimate the effect of small errors in the angle of incidence. Figure (11) shows the effect of using incorrect values for θ in the calculations of n and k. Clearly for this case the errors arising from inaccurate θ may be virtually eliminated by normal procedures for measuring angles of incidence. In any experiment to determine optical constants from reflection coefficients the quantity δR will determine the resulting errors in optical constants.

2.10. Normal Incidence Measurements

The principal reason for making measurements near $\theta = 0$, is that for small angles the following relationship holds appromixately:

$$R_\perp = R_{//} \qquad (18)$$

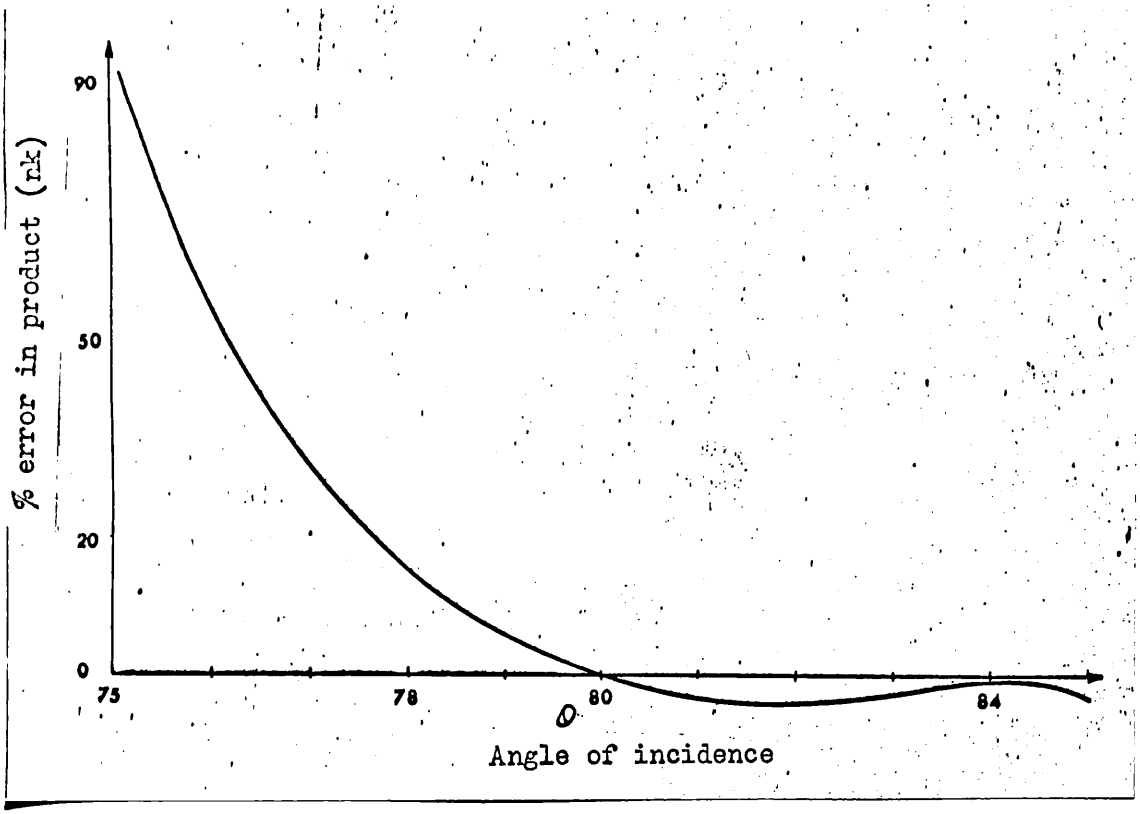

Figure 11. Errors in product (nk) due to incorrect angular settings.

$\delta\theta = (80 \pm \theta)^{\circ}$

and thus the total reflectivity may be written:-

$$\frac{R_{\perp} + R_{//}}{2} = R_{\perp} = R_{//} \qquad (19)$$

Thus, unpolarized light may be used and only one measurement is made for each determination. Clearly, the Fresnel reflectance equations are insufficient to solve the system for n and k. An extra condition is required, an example of which is provided by the Kramers-Kronig relationship.

The equations relevant at normal incidence are:

$$n = \frac{1 - R}{1 + R - 2R^{\frac{1}{2}}\cos\varphi} \qquad (20)$$

and

$$k = \frac{-2R\sin\varphi}{1 + R - 2R^{\frac{1}{2}}\cos\varphi} \qquad (21)$$

These follow directly from the Fresnel reflectance equations if we express the complex reflection amplitude in the form $\sqrt{R}\exp i\varphi$, where φ is the phase change on reflection. The relationship between φ at a particular frequency ω and the measured reflection coefficient may be expressed in the form (Bode 1945).

$$\varphi(\omega_0) = \frac{1}{\pi}\int_0^{\infty} \log_e\left|\frac{\omega+\omega_0}{\omega-\omega_0}\right| \frac{d}{d\omega}\log\sqrt{R(\omega)}\,.\,d\omega \qquad (22)$$

Clearly difficulties arise because (22) is an integral over all frequencies and we only have an incomplete knowledge of the reflectivity spectrum. It will be assumed, however, for the sake of this discussion that the Kramers-Kronig type of analysis is capable of yielding correct optical constants from normal incidence

reflection data. The important question now arises as to how sensitive will a normal incidence reflectivity be to the optical constants n and k.

Normal incidence conditions are assumed to hold for angles of incidence as high as 12°. (Kress and Lapere 1970). At such an angle it is still assumed that $R_{\perp} = R_{//}$ Figure (12) shows the values of $R_{\perp}$ and $R_{//}$ calculated for $n = 2.000$ and $k = 3.000$ for various angles of incidence near zero. This figure shows that any attempt to determine n and k by the direct solutions to the Fresnel equations and assuming $R_{\perp} = R_{//}$ would prove disastrous. We note both from figure (2) and figures (7 and 8) that we would not expect normal incidence reflection coefficients to be sensitive to changes in optical constants. The following example illustrates the point most forcibly:-

When: $n = 2.000$, $k = 3.000$ $\theta = 12^{\circ}$

$$R_{\perp} = 0.563 \qquad R_{//} = 0.548$$

We now consider a small change in reflection coefficients to

$$R_{\perp} = 0.564 \qquad R_{//} = 0.547$$

the optical constants required to produce this change are:-

$$n_0 = 0.760 \text{ and } k_0 = 1.934$$

This again shows that it would be disastrous to attempt to determine optical constants by solving the Fresnel equations at such an angle of incidence. The value of σ corresponding to such a change is 76%. The same calculation performed for $\theta = 74^{\circ}$ yields $\sigma = 2.7\%$. In terms of changes in the reflectivity spectrum the above calculation is significant.

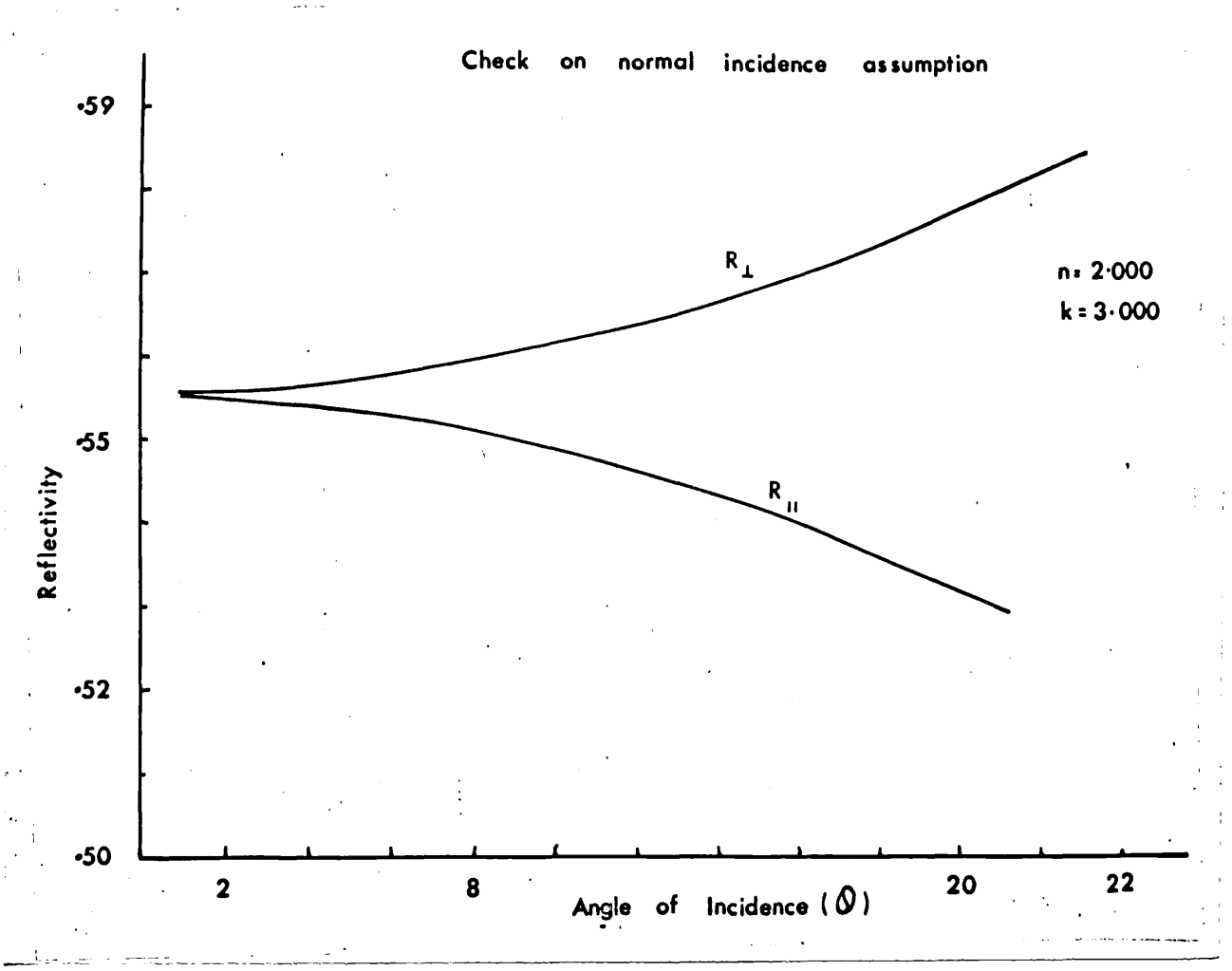

Figure 12. Variation of reflection coefficients with angle of incidence at near normal incidence.

It can be shown by using a large number of significant figures in the above calculation that n and k vary continuously between the two sets of reflectivity data given above. If a material has optical constants such that the reflection coefficients vary in the above way, only small changes will be observed in the normal incidence reflectivity spectrum. To emphasize the point, if the smallest observable change in reflectivity measured on a specific normal incidence reflectometer is 0.001, changes as large as $n = 2.000 \rightarrow n = 0.760$ and $k = 3.000 \rightarrow k = 1.934$ are only just resolved. Thus it would seem that normal incidence methods are not useful for the determination of optical constants.

However, the fact must be faced that normal incidence methods have been used and some reasonably small changes in optical constants have been detected. In particular, optical constants have been determined in this work which produce a reasonably sensitive normal incidence spectrum.

The following goes some way towards resolving the dilemma; an experiment performed at an angle of incidence of 5° is considered. The bounded region in $(R_{\perp}, R_{//})$ space is shown in figure (13). The shaded region represents those values of n and k for which the reflection is metallic (i.e. $(n^2 - k^2) < 0$). A circle of radius ρ is drawn with centre at the point corresponding to $n_o = 2.000$ and $k_o = 3.000$. Radii are then drawn making angles φ with the axis (figure 13). Calculations of n and k are then

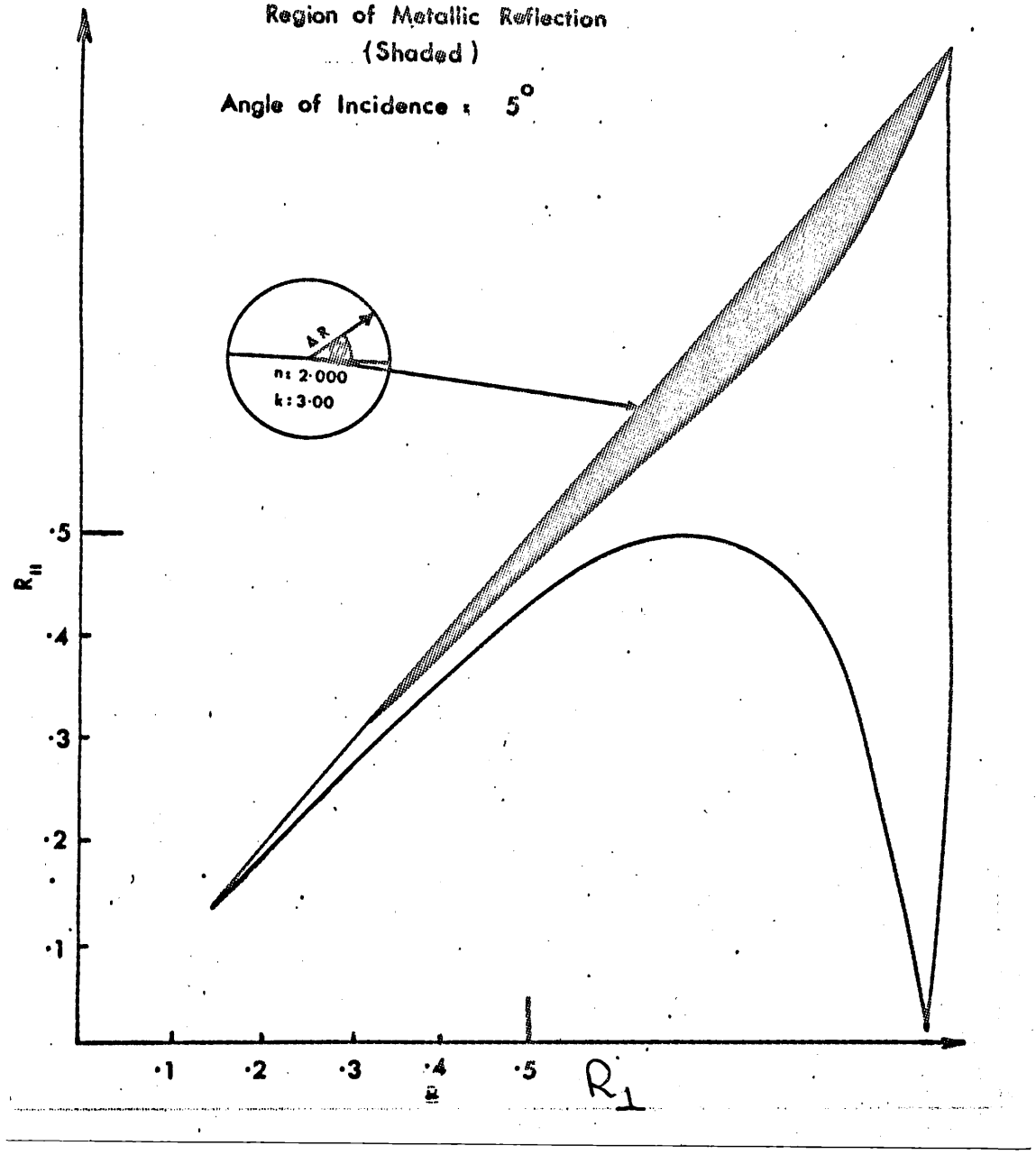
Region of Metallic Reflection
(Shaded)
Angle of Incidence : 5°
ΔR
n: 2·000
k: 3·00
R∥
·5
·4
·3
·2
·1
·1
·2
·3
·4
·5
R⊥

Figure 13.

carried out along the radius vector using:-

$$R_{\perp} = R_{\perp o} + \rho \cos \varphi \qquad (23)$$

$$R_{\parallel} = R_{\parallel o} + \rho \sin \varphi \qquad (24)$$

where $(R_{\perp o}, R_{\parallel o})$ is the point corresponding to $n = 2.000$ $k = 3.000$. The maximum values of ρ was set at 0.001 and it is assumed that this is the smallest detectable change in reflectivity for a given experimental system. Thus the minimum detectable changes in optical constants are of the order of those occuring for $\rho = 0.001$. The results of this calculation are shown in (14). We note the extreme dependance of the minimum detectable change in n and k on φ. In figure (14) the product nk is plotted against ρ. Table (1) shows how n and k vary individually with ρ for $\varphi = 40^{\circ}$ and $\varphi = 45^{\circ}$. Clearly the sensitivity of the reflection spectrum to small changes in optical constants is greatest for $\varphi = 45^{\circ}$. A small change in φ produces a large decrease in sensitivity: for example, with $\varphi = 44^{\circ}$ the minimum detectable % change in the product in $\sim 13\%$. At this stage it is interesting to note that all normal incidence experiments assume that $R_{\perp} = R_{\parallel}$ and therefore $\varphi = 45^{\circ}$. For this reason it will at least appear that the normal incidence reflectivity is sensitive to small changes in optical constants. Further calculations for various n and k indicate that maximum sensitivity always occurs for $\varphi = 45^{\circ}$.

There are two possible conclusions which one may draw from this work. The first is that because of the limited precision of reflectometer systems only certain types of variation

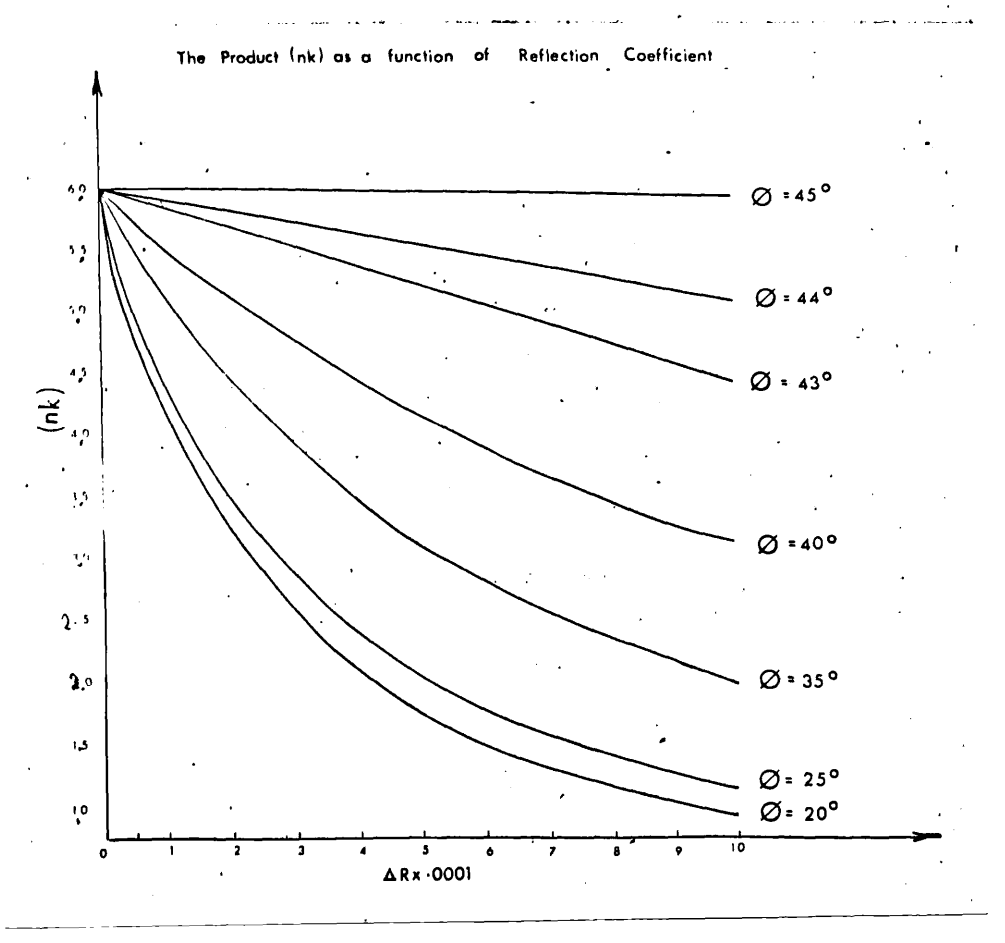

Figure 14. Change in (nk) along radius vector ρ for various ϕ.

	$\varphi = 40^\circ$		$\varphi = 45^\circ$	
ρ	n	k	n	k
0.0000	2.000	3.000	2.000	3.000
0.0001	1.881	2.938	1.998	2.999
0.0002	1.777	2.878	1.995	2.999
0.0003	1.684	2.821	1.993	2.998
0.0004	1.601	2.766	1.990	2.997
0.0005	1.526	2.714	1.988	2.996
0.0006	1.459	2.664	1.985	2.996
0.0007	1.398	2.616	1.983	2.995
0.0008	1.342	2.571	1.981	2.994
0.0009	1.291	2.528	1.978	2.993
0.0010	1.245	2.486	1.976	2.992

TABLE (1)

in optical constants will be detected. (i.e. those for which $\varphi = 45^{\circ}$). In this case normal incidence determinations yield incomplete information about the optical properties of materials. The second possible conclusion is that normal incidence experiments do yield a complete description of the optical properties and therefore optical constants of real materials vary in such a way that conditions of high sensitivity hold. In view of the apparently good agreement obtained between experiment and theory for some normal incidence experiments the last possibility cannot be dismissed. Clearly this conclusion implies a constraint other than the Fresnel equations on the variation of optical constants with wave length. The Kramers-Kronig analysis shows that the behaviour of the reflectivity in the neighbourhood of a particular frequency, is in fact, dependant on its behaviour throughout the spectrum. A survey of optical data is being carried out at the present time in order to establish the sensitivity of normal incidence spectra to the optical constants of several metals.

2.11 Summary of Results

The conditions for real solutions to the Fresnel reflectance equations have been established. The best range of angles for the determination of optical constants has been determined. In particular, it has been shown that results obtained at angles far removed from optimum values are subject to large inherent errors. It has been shown that normal incidence

reflectivity spectra are only sensitive to limited types of variation in optical constants.

CHAPTER III

NUMERICAL TECHNIQUES FOR THE DETERMINATION OF OPTICAL CONSTANTS FROM OBSERVED FUNCTIONS OF $R_\perp$ AND $R_{//}$ MEASURED AT TWO ANGLES OF INCIDENCE.

3.1. Introduction

It is often convenient to measure a function of the reflection coefficients $R_\perp$ and $R_{//}$ rather than the coefficients themselves. In order to obtain n and k this function is measured at two angles of incidence and values of n and k found that will reproduce the function values at both angles of incidence. The solutions to Fresnel equations are used in a numerical technique for the solution of the system and this permits a rapid computation of n and k. Optimization techniques established in Chapter II are then used to obtain optimum experimental conditions.

3.2. Numerical Technique

The technique will be outlined for the general case and described in detail for a particular case.

If for some observable function of $\varphi (R_\perp , R_{//})$ there is a linear relationship:-

$$R_\perp = \alpha R_{//} + \beta \qquad (1)$$

where α and β depend only on φ and/or known constants of the system, then measurement of $\varphi (R_\perp , R_{//})$ at two angles of incidence,

θ_1 and θ_2, allows n and k to be calculated as follows. At angle θ_1, we can write:-

$$R_\perp = \alpha_{\theta 1} R_{//} + \beta_{\theta 1} \qquad (2)$$

Sets of (n, k) pairs are calculated such that the relationship (2) holds. These values are then used to determine $\varphi(R_\perp, R_{//})$ at θ_2. The quantity:-

$$\delta = \left[\varphi(R_\perp, R_{//})_{calc.} - \varphi(R_\perp, R_{//})_{Obs} \right]_{\theta = \theta_2} \qquad (3)$$

is then made arbitrarily small using the (n, k) values generated by (2). The (n, k) pair which minimises δ is the required (n, k) solution.

3.3. Reflectance Ratio Measurements

At this point it is convenient to describe the advantages of measuring reflectance ratios rather than reflection coefficients. If a ratio is measured, no beam normalization is required provided that the incident intensity components, $I_{o\perp}$ and $I_{o//}$, are equal. When measuring absolute reflection coefficients some rearrangement of the system is necessary in order to measure the incident beam under near identical conditions to those for which the reflected intensity is measured. Rearrangement is likely to introduce errors into the determination through small differences in optical path for the two measurements. In addition, the accurate rearrangement of the system is likely to take a long time compared with that required to simply rotate a polariser, and this places strict requirements

on the source and detector stabilities in the system. The ratio method is ideally suited to measurements on samples maintained in a vacuum system. In this situation, for reflection coefficient measurement, two identical windows are needed or else they need to be calibrated at each wavelength. This is because for most systems, not employing standard reflectors, it is impossible to view the incident and reflected beams through the same window. For reflection ratio measurements both components in the ratio can be measured under identical optical conditions provided that the windows are non-dichroic and light is incident on them normally. For these reasons this method is probably the most experimentally convenient for the determination of the optical constants of samples (maintained in ultra-high vacuum systems).

3.4. Calculation of Optical Constants from Reflectance Ratios

In this case:-

$$\Phi (R_\perp , R_{||}) = \frac{R_\perp}{R_{||}} \qquad (4)$$

Therefore equation (1) becomes

$$R_\perp = \left(\frac{R_\perp}{R_{||}}\right)_{\theta_1} R_{||} \qquad (5)$$

In this case we can consider the solutions in terms of straight lines drawn in $(R_\perp , R_{||})$ space. Figure (15a, b,) shows bounded regions in $(R_\perp , R_{||})$ space at the two angles of incidence θ_1 and θ_2.

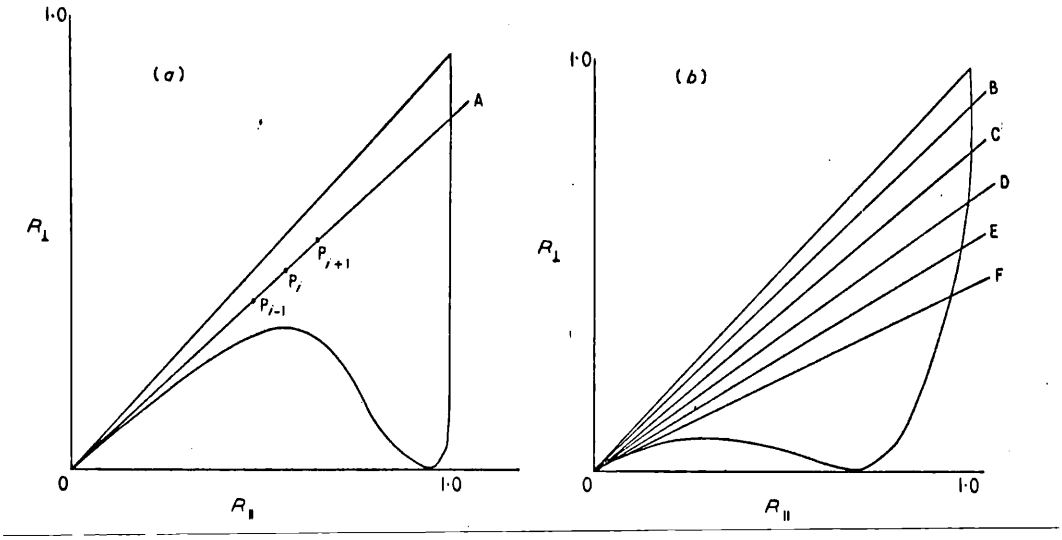
1·0
(a)
A
$R_\perp$
P_{i+1}
P_i
P_{i-1}
0
1·0
$R_\parallel$
1·0
(b)
B
C
D
E
F
$R_\perp$
0
1·0
$R_\parallel$

Figure 15.

The observed ratios $(R_\perp / R_{//})_{\theta_1}$, and $(R_\perp / R_{//})_{\theta_2}$ correspond to the slopes of the lines OA and OB passing through the origins of the $(R_\perp , R_{//})$ diagrams at $\theta_1 \& \theta_2$ respectively. Consider the line OA, of slope $(R_\perp / R_{//})_{\theta_1}$. Each point corresponds to a different (n, k) pair given by solutions to the Fresnel reflectance equations. The ratio $(R_\perp / R_{//})_{\theta_2}$ may be used to calculate n and k in the following way. Pairs of (n, k) values derived from $(R_\perp , R_{//})$ values generated by equation (5) are used to locate a fan of lines such as OC, OD, OE and OF of figure (15b). Each line has a different slope and only one will correspond to the observed reflectance ratio $(R_\perp / R_{//})_{\theta_2}$. The (n, k) pair generating this line is the required solution.

3.5. Computational Details

The method described in (3.4.) is particularly convenient for digital computation. Starting at the origin O, on the line OA, figure (14a), values of n and k are calculated at a number of equispaced points, P_1, P_2, P_3 ----P_n along OA and for each point the slope of the line at θ_2 is computed. The calculation proceeds until the quantity:-

$$\delta = \left[\varphi (R_\perp , R_{//})_{Calc} - \varphi (R_\perp , R_{//})_{Obs}\right]_{\theta = \theta_2}$$

$$= \left[\left(\frac{R_\perp}{R_{//}}\right)_{Calc} - \left(\frac{R_\perp}{R_{//}}\right)_{Obs}\right]_{\theta = \theta_2} \qquad (6)$$

starts to increase. If δ starts to increase at a point P_i on OA the calculation is restarted at a point P_{i-2}. , the step size

defined as the length OA/j is reset to a value $OA/\varsigma j$ where ς is an arbitrary reduction factor. The calculation proceeds in this way until δ reaches an arbitrarily small value. The point on OA at which calculation ceases thus corresponds to the desired solutions for n and k. In practice δ_{min} is set marginally less than the experimental uncertainty in the value of the ratio. Generally the initial step size was set so that $R_\perp$ varied by 1% for each step.

The flow diagram for the computer programme used in the calculation is shown in figure (16) and a listing is given in appendix (1). The subroutines SOLVE and CHECK are those described in (2.6.). In the programme it was necessary to allow for cases where the required point lies close to a [illegible] boundary. This was achieved as follows. If the subroutine SOLVE returned negative values for k a check was made to see if any positive values had been returned previously during the search. If positive values had been returned then this implied that the test point had traversed the valid region. This being the case the calculation was restarted two steps back with a reduced step size. If positive values had not been returned then the search was continued with no adjustment to the stepsize. The following data illustrate the efficiency of the calculation. The values of the ratios imput into the programme were calculated for n = 2.000 and k = 3.000 with $\theta_1 = 67.5$ and $\theta_2 = 75.0$

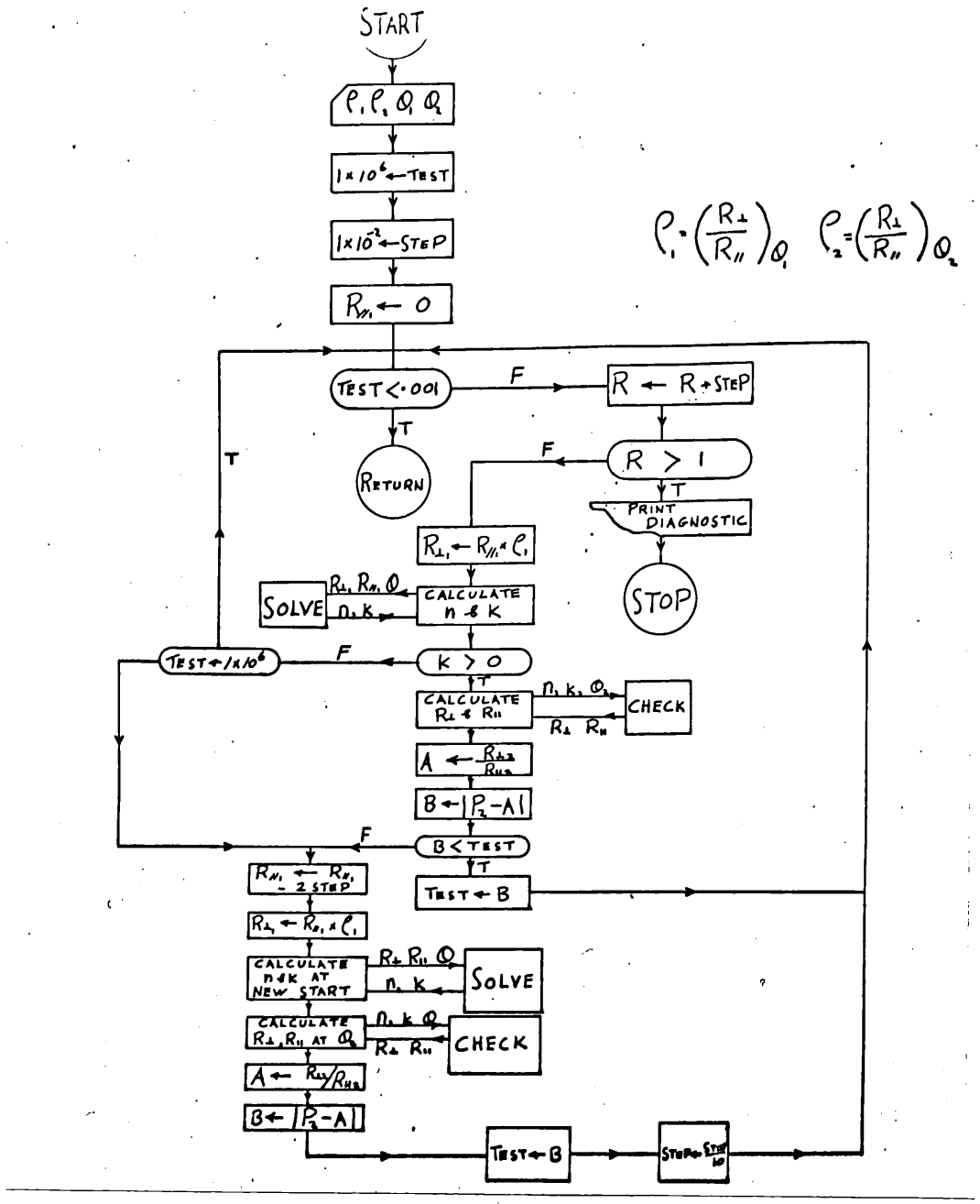

Figure 16. Flow diagram of technique for determination of n and k from ratio measurements.

Value of n	Value of k	Optimum region for θ_1	Optimum region for θ_2	Error in product nk (σ%)
low; ~1	high; ~4	$56° \leqslant \theta_1 \leqslant 69°$	$80° \leqslant \theta_2 \leqslant 85°$	<2·0
mod; ~2	mod; ~3	$58° \leqslant \theta_1 \leqslant 69°$	$78° \leqslant \theta_2 \leqslant 85°$	<1·0
high; ~4	low; ~1	$50° \leqslant \theta_1 \leqslant 69°$	$70° \leqslant \theta_2 \leqslant 85°$	<0·5

Table 2.

Value of n	Value of k	Optimum region for θ_1	Optimum region for θ_2	Error in product nk (σ%)
~1	~4	$50° \leqslant \theta_1 \leqslant 67°$	$77° \leqslant \theta_2 \leqslant 80°$	<1·0
~2	~3	$50° \leqslant \theta_1 \leqslant 67°$	$74° \leqslant \theta_2 \leqslant 81°$	<1·0
~4	~1	$50° \leqslant \theta_1 \leqslant 68°$	$75° \leqslant \theta_2 \leqslant 81°$	<1·0

Table 3.

Step size	n	k
0.01	4.032	5.002
0.001	2.025	3.042
0.0001	2.000	3.000

n and k are the best values obtained for the stepsize indicated. Solutions accurate to 1 part in 3000 are typically obtained in less than 0.05 seconds. (CDC. 6600) (FORTRAN IV) The reflection ratio method has been discussed by Avery (1952) and his analysis improved by Miller and Taylor (1971). The method described here, however, is considered to be far more efficient than any described previously. Kolb (1972) has recently found analytic solutions for the ratio method which are computationally longer and more complicated than the above technique.

3.6. The Sensitivity of the Ratio Method

The rapid convergence of the computational procedure allows a comprehensive study of the reflection ratio method to be made. σ , defined in (2.5.), was calculated for various combinations of θ_1 and θ_2. The results are summarized in tables (2) and (3) for n and k in the ranges $1 \leq n \leq 4$, $1 \leq k \leq 4$. The quantity σ was calculated for all combinations of θ_1 and θ_2 in the ranges $50^\circ \leq \theta_1 \leq 69^\circ$ and $70^\circ \leq \theta_2 \leq 85^\circ$ for each (n, k) pair. In compiling table (2) errors of $\pm$ 0.005 were assumed in the reflection ratio, and no errors in θ_1 and θ_2. An error of $\pm$ 0.005 should not be too difficult to achieve experimentally.

Since there was no dramatic variation of σ with θ_1 and θ_2 it was decided that optimum angular regions could be defined, rather than specific angles. For any values of θ_1 and θ_2 in the ranges indicated the values of σ will be less than the value shown. In the range $\delta\left(\frac{R_\perp}{R_\parallel}\right) = 0.005 \rightarrow 0.01$ it was found that σ varied almost linearly with errors in the reflection ratio. Table (3) was obtained by assuming no errors in reflection ratio and errors of 0.1° in θ_1 and θ_2. Again there was no dramatic variation of σ with θ_1 and θ_2 when these were in error by $\pm 0.1^\circ$, however, σ was found to vary strongly with θ_1 and θ_2 when these were in error by $\pm 0.5^\circ$. For errors of this size the optimum regions were considerably shortened. As an example, for $n = 2.000$, $k = 3.000$ and $\sigma < 2.5\%$ theoptimum region for θ_1 was found to be $50^\circ \leq \theta_1 \leq 60^\circ$ and for the value θ_2 the single value $\theta_2 = 76^\circ$ was obtained. A comparison with the reflection coefficient method will not be made at this stage. We note that an error of 0.005 in the reflectance ratio will represent a smaller percentage error than it will in the separate coefficients and allowance must be made for this before making comparisons on a percentage error basis.

3.7. Two-Angle Methods for Light Incident with Arbitrary Polarisations

If light is incident on a surface with its electric vector polarised at an angle χ to the plane of incidence then the reflection coefficient may be written:-

$$R_\gamma = R_{//}\cos^2\gamma + R_\perp \sin^2\gamma \qquad (7)$$

Thus:-

$$\varphi(R_\perp, R_{//}) = R_{//}\cos^2\gamma + R_\perp \sin^2\gamma \qquad (8)$$

and equation (2) becomes:-

$$R_\perp = \frac{R_\gamma}{\sin^2\gamma} - R_{//}\cot^2\gamma \qquad (9)$$

Therefore the calculation can proceed in precisely the same way as in (3.5.) except that in this case the geometrical interpretation is in terms of intercepts rather than slopes.

We can immediately identify an experimentally interesting case. If $\gamma = 45^\circ$ then:-

$$R_\gamma = \frac{R_\perp + R_{//}}{2} \qquad (10)$$

Thus $R_\gamma = R_T$ (the total reflectivity) and the method may prove suitable for determinations where polarisation of the light beam is either difficult or inconvenient (e.g. for infra-red measurements).

3.8. Sensitivity of Total Reflectivity Methods

With minor modifications the programme described in 3.5. was used to estimate the optimum conditions for the determination of optical constants from total reflectivities measured at two angles of incidence. It was found that small errors occur for small errors in the reflectivity when measurements are made for $\theta_2 < 45^\circ$ and $\theta_1 > 45^\circ$. The sensitivity was found to be almost independent of θ_2. Generally for $k < 2$ the minima associated with the optimization were shallow. Figure (17) shows the variation

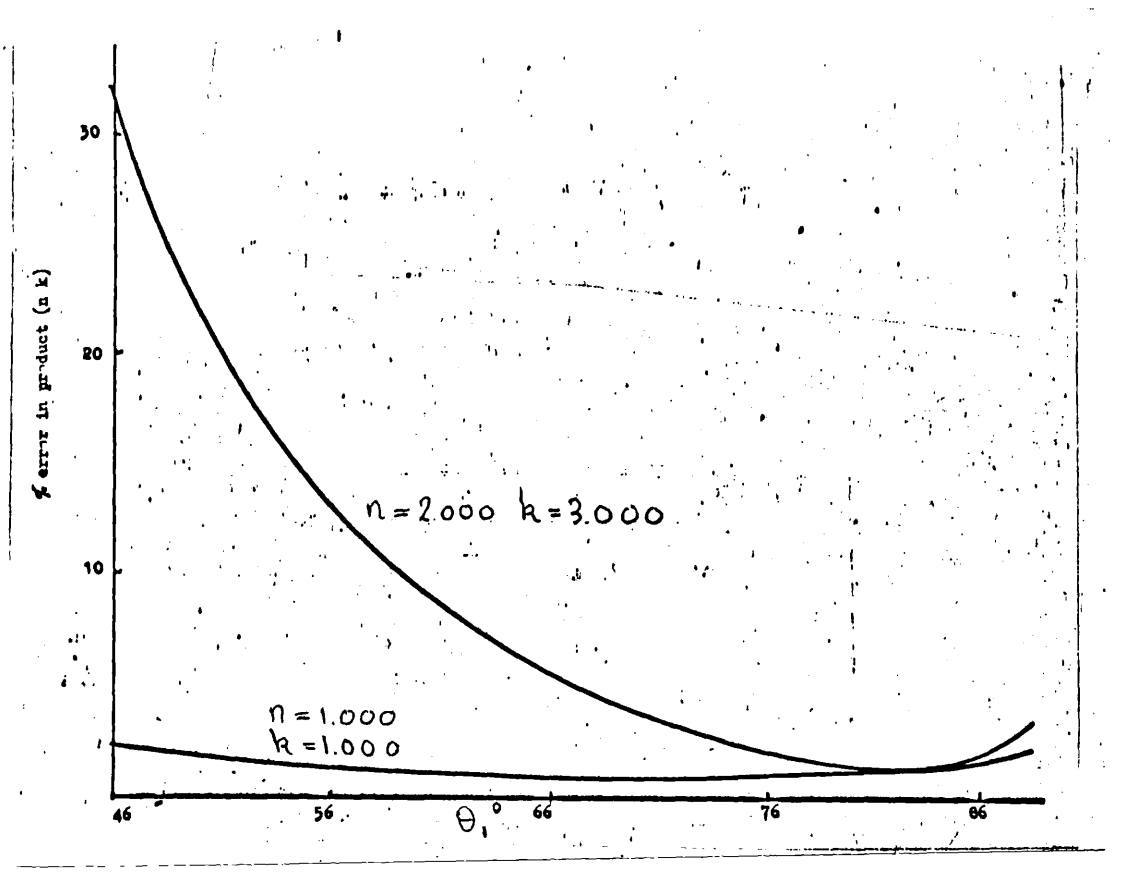

Figure 17. Variation of % error in product (nk) with angle of incidence

n	k	Optimum θ_1°	% Error in Product (n k) Due to errors in intensity measurements	Due to errors in Angular determinations	Shape of Minima
1.000	1.000	70°	0.9	1.2	Shallow
1.000	2.000	79°	1.8	1.7	Shallow
1.000	3.000	81°	2.50	1.8	Sharp
1.000	4.000	85°	3.3	3.1	Sharp
2.000	1.000	75°	0.21	0.04	Shallow
2.000	2.000	83°	1.1	2.0	Shallow
2.000	3.000	85°	1.5	2.5	Sharp
2.000	4.000	89°	1.9	2.8	Sharp
3.000	1.000	83°	0.8	4.9	Shallow
3.000	2.000	84°	0.6	0.9	Shallow
3.000	3.000	84°	1.1	1.8	Sharp
3.000	4.000	85°	1.4	2.4	Sharp
4.000	1.000	78°	3.9	4.7	Sharp
4.000	1.000	73°	0.002	0.070	Shallow
4.000	1.000	85°	0.9	1.32	Sharp
4.000	1.000	86°	1.2	2.52	Sharp

$\theta_2 = 20^\circ$

$\delta R = 0.2\%$ $\delta\theta = 0.1^\circ$

TABLE (4)

of σ with θ_1 for n = 1.000, k - 1.000 and n = 2.000, k = 3.000 Clearly, even for the n = 2.000, k = 3.000, case the range of optimization is quite broad. We note, however, that large errors are likely to occur under non-ideal conditions. The effect of small errors in angle becomes important in this method; however, good angular determinations are probably easier to make than intensity measurements. Table (4) was compiled as follows. δR was set at 0.001 and the change in the product n k calculated, σ was then calculated and the angle, θ_1, at which σ took a minimum value was assumed to be optimum with $\theta_1 = 20^\circ$. The calculations were not affected by changes in $\theta_2 \sim 5^\circ$. With $\delta R = 0$ the effect of small changes in θ_1 and θ_2 was estimated by using $\theta_1 = \theta_1 + \delta\theta$ and $\theta_2 = \theta_2 - \delta\theta$ in the calculation. The results with $\delta\theta = 0.1^\circ$ are shown in the Table (4). Also given in this table is an indication of the shape of the minima of the curve $(\sigma \sim \theta_1)$. Where the minima are shallow, optimization is not generally important, and where the minima are sharp a deviation $\sim 10^\circ$ from the optimum θ_1 results in a significant increase in the errors associated with the determination.

3.9. Variation of σ with Polarisation Azimuth

A computer programme was written to calculate the sensitivity of two-angle methods for various azimuth γ in the range $0 < \gamma < 90^\circ$. The programme was run for many combinations

of n and k and the results always showed that maximum sensitivity occurs for $\chi = 0$. Figure (18) shows a typical variation. Thus if a fixed polarisation is used at two angles of incidence, considerable advantage is to be gained by measuring $R_{//}$. This conclusion is in accordance with figures (3) and (4) (Chapter II).

3.10 Sensitivity of the $R_{//}$ Method

Several modifications to the previously used programme were necessary in order to obtain solutions. This was because the optimum value of θ, occurs near 45°. Figure (2) (Chapter II) shows that the bounded region in ($R_{\perp}$, $R_{//}$) space is narrow. Thus, in order to obtain solutions, a very small step size is needed. This, in turn, causes an increase in computing time. However, the boundary is defined by equation (11, 2) thus we can in principle start the programme with $R_{\perp}$ set at a point on the boundary. Clearly, from (11, 2) P^2 is a quartic function of F so that for a given value of $R_{//}$ four boundary values of $R_{\perp}$ can be calculated. A routine based on Bairstows iterative method of quadratic factorization (Wilkinson 1959) was used to solve the quartic equation. Figure (2) shows that at some angles of incidence for $R_{//} \lesssim 10\%$ four real roots to the quartic equation are possible. This being the case, a warning diagnostic was printed and, if necessary, the calculation restarted at an appropriate value of $R_{\perp}$. If two real roots were obtained, the calculation was started at

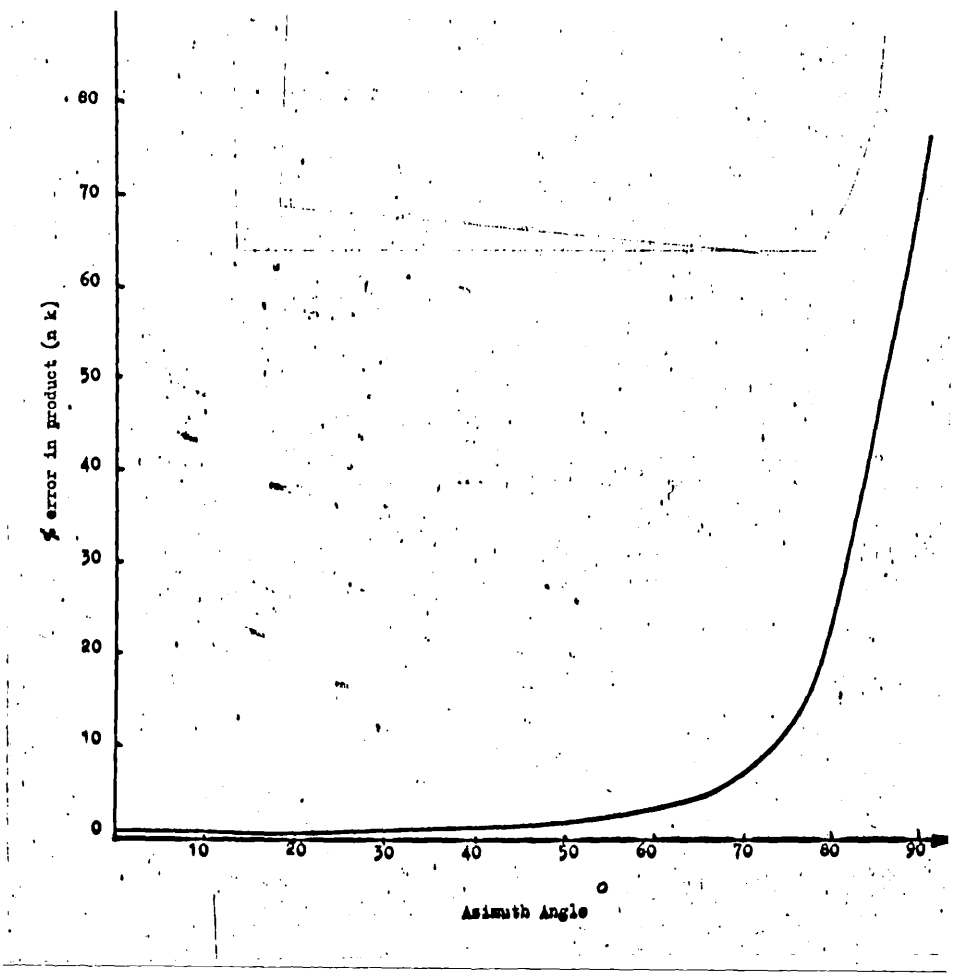

Figure 18. Variation of sensitivity with polarisation asimuth. $n = 2.000$ $k = 3.000$

n	k	Optimum θ_2°	% Error in (n k) Due to Intensity Errors	Due to Angular Errors
1.000	1.000	56 - 67	$\lesssim 1$	<1
1.000	2.000	72 - 76	$\lesssim 1$	<1
1.000	3.000	73 - 79	$\lesssim 2$	<1
1.000	4.000	81	$\lesssim 2$	<1
2.000	1.000	58 - 86	<1	<1
2.000	2.000	66 - 80	<1	<1
2.000	3.000	74 - 81	<1	<1
2.000	4.000	81 - 82	<1	<1
3.000	1.000	69 - 75	<1	<1
3.000	2.000	69 - 85	<1	<1
3.000	3.000	74 - 83	<1	<1
3.000	4.000	79 - 83	<1	<1
4.000	1.000	75 - 76	<1	<1
4.000	2.000	65 - 86	<1	<1
4.000	3.000	75 - 85	<1	<1
4.000	4.000	78 - 84	<1	<1

TABLE (5)

the value which gave the smallest value of R_1 . This procedure allowed two orders of magnitude decrease in the initial step size with no loss in programme efficiency. Again it was found that the sensitivity was almost independent of one of the angles of incidence. For $\theta_1 = 48^\circ$ the errors in the product n k resulting from changes in reflectivity of 0.001 for various θ_2 are shown in Table (5). Also shown is the effect of changes in θ_1 and θ_2 of 0.1°. In general the minima in the curves are shallow. Figure (19) shows the variation for n = 1.000, k = 1.000 and n = 2.000, k = 3.000.

3.11 Comparison of Techniques

At this stage its worthwhile to compare the techniques developed in this and the previous chapter. It is assumed that an accuracy of 0.2% can be achieved in the measurement of all the intensity ratios and no account is taken of the fact that this accuracy is more readily achieved in the ratio system.

The results of this study are shown in Table (6). This table was obtained by calculating the effects of changes $\sim$ 0.2% in intensity ratios measured under optimum conditions.

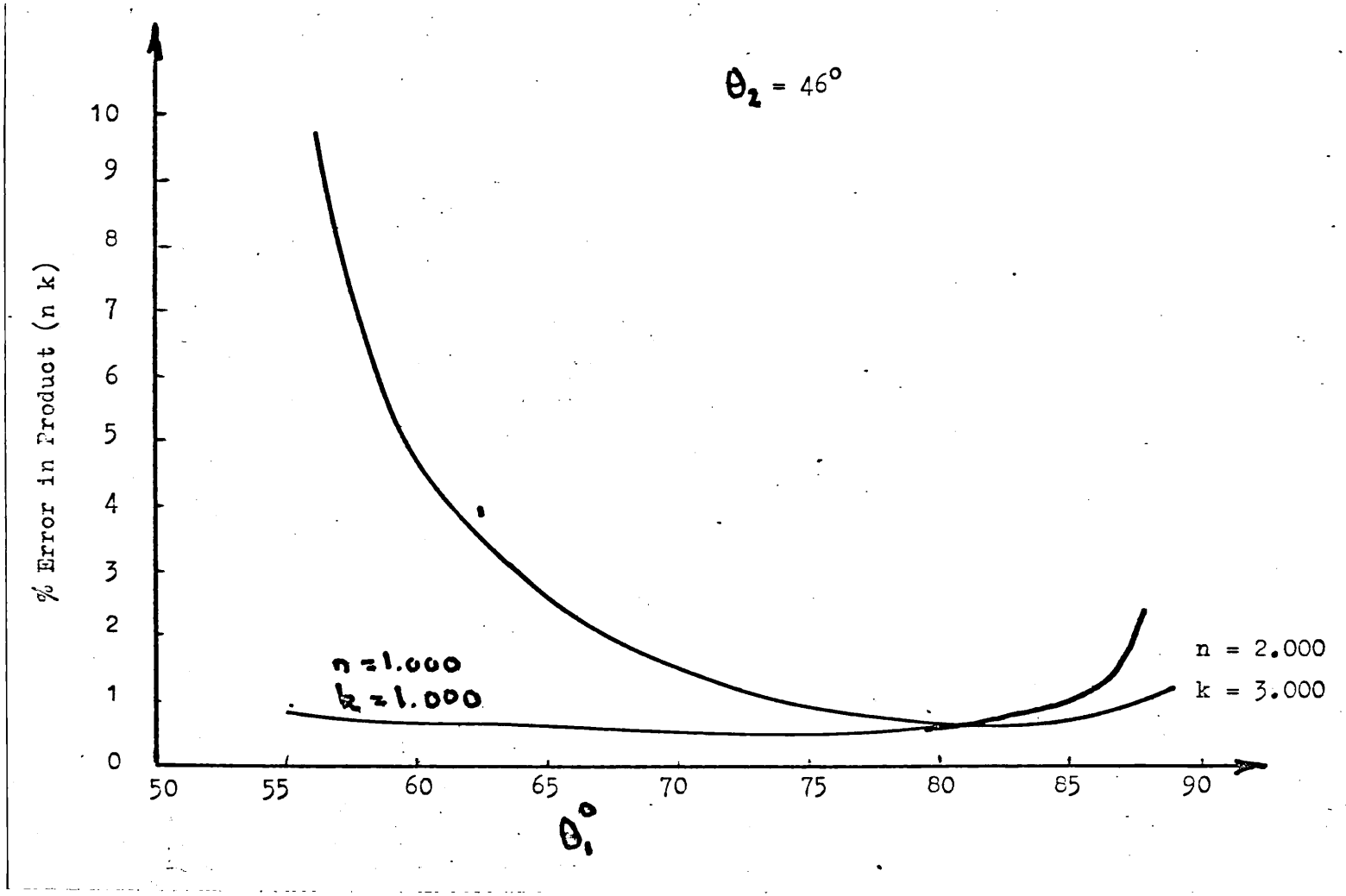

Figure 19. Variation of percentage error in product (nk) with angle of incidence , with R = 0.001

Error %

		Coefficient Method			Ratio Method			Total Reflectivity Method			Parallel Method		
n	k	n	k	(nk)	n	k	(nk)	n	k	(nk)	n	k	(nk)
1.000	1.000	0.347	0.868	1.218	0.039	2.515	2.563	0.590	0.451	1.038	0.297	0.321	0.619
	2.000	0.968	1.504	2.487	0.436	0.617	1.050	1.057	0.714	1.764	0.385	0.365	0.752
	3.000	2.252	2.924	5.242	0.484	0.622	1.103	1.511	1.095	2.589	0.708	0.604	1.317
	4.000	4.054	5.644	9.927	1.257	1.187	2.429	1.904	1.464	3.340	0.955	0.841	1.804
2.000	1.000	0.252	0.747	1.000	0.116	0.130	0.246	0.676	0.383	0.296	0.133	0.045	0.178
	2.000	0.600	1.110	1.716	0.236	0.346	0.581	0.787	0.299	1.083	0.185	0.170	0.356
	3.000	1.130	2.092	3.246	0.377	0.416	0.791	0.955	0.580	1.529	0.308	0.282	0.591
	4.000	2.148	3.453	5.675	0.644	0.565	1.205	1.136	0.814	1.941	1.667	0.924	2.606
3.000	1.000	0.420	1.354	1.780	0.070	0.091	0.161	0.627	1.534	0.898	0.107	0.089	0.197
	2.000	0.793	1.108	1.910	0.183	0.164	0.347	0.714	0.014	0.728	0.188	0.134	0.322
	3.000	1.246	1.869	3.138	0.290	0.249	0.539	0.810	0.374	1.181	0.272	0.223	0.495
	4.000	1.941	3.010	5.009	0.785	0.493	1.274	0.914	0.583	1.492	0.424	0.337	0.763
4.000	1.000	0.498	9.157	9.700	0.104	0.227	0.330	0.991	4.964	3.924	0.231	0.533	0.303
	2.000	0.712	3.814	4.553	0.193	0.134	0.327	1.955	2.028	0.033	0.230	0.080	0.310
	3.000	1.143	3.175	4.353	0.305	0.210	0.514	0.747	0.212	0.957	0.292	0.192	0.484
	4.000	1.906	3.477	5.449	0.404	0.269	0.672	0.813	0.458	1.267	0.336	0.283	0.621

Table 6

CHAPTER IV

REFLECTOMETER SYSTEMS

4.1. Introduction

The difficulties associated with the determination of optical constants from separate reflection coefficients have been discussed in 3.3. However, a one-angle determination of n and k may, under certain circumstances, become necessary. For example a one-angle method is essential when the specimen is optically anisotropic (eg. some epitaxial films). There may also be situations where measurement at two angles is experimentally inconvenient; for example in magneto-optical work where a magnetic field is applied perpendicular to the surface. For these reasons a reflectometer was devised which enables accurate determinations of optical constants to be made at one angle of incidence. In particular the system was constructed so that measurements could be made on samples created and maintained in an ultra-high vacuum chamber. It was decided to build a demountable reflectometer, because a system which remained in position throughout the pumping cycle of the vacuum would have to be either well removed from the chamber, thus introducing excessive path lengths, or would need to be bakable to 300°C. For these reasons a reflectometer was built which could be removed whilst the system is baked. Ideally such a system should be completely reproducible in order to avoid lengthy realignment.

The reflectometer described below fulfils this requirement and overcomes some of the difficulties discussed in (3.3.)

4.2. Reflectometer Principle

The principle of the instrument is similar to that used by Querry et al (1969). However, the number of mirrors has been reduced to two and the reflectometer has been designed to operate under near optimum conditions. The geometry of the system is illustrated in figure (20). A collimated, monochromatic, plane polarized light beam is incident on the window W_1. In the "sample out" configuration, the light passes straight through the chamber, through W_3 and falls on m_1. The beam reflected by m_1, is then reflected by m_2 through an aperture S, onto a diffusing screen, and the intensity is measured by a photomultiplier P.M. In the "sample in" configuration the light, after reflection from the sample Sp, passes through W_2 and then follows a similar path to that described for the "sample out" configuration. Clearly the triangles Sp, m_2, m_1 and Sp, m_2, m_1' are similar if we make the angle Sp, m_1, m_2 equal to the angle of incidence of the light on the sample. The angle of incidence chosen was 75°, this being the closest to the optimum values discussed in Chapter II permitted by the vacuum system. Clearly, the ratio of the signals obtained for the "sample in" and the "sample out" will only represent an accurate reflectivity if the windows W_2 and W_3 are optically identical. This limitation is discussed below.

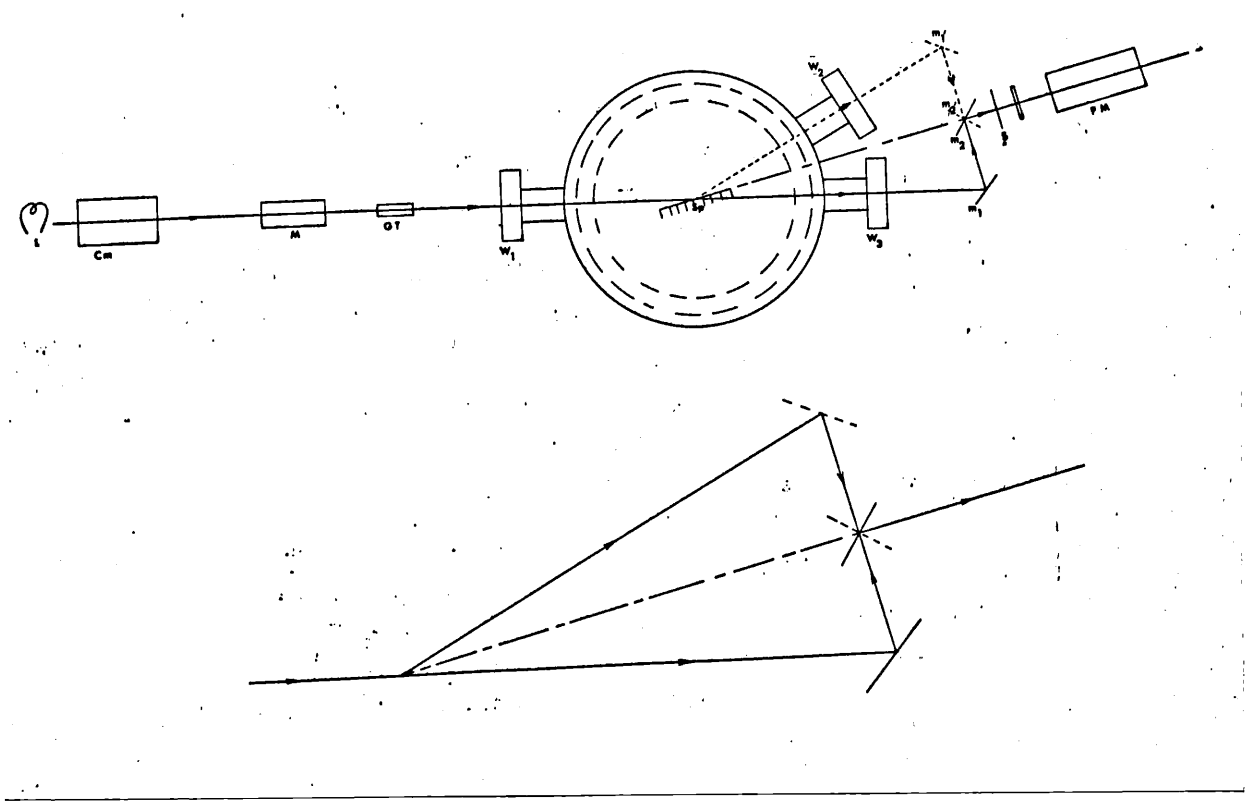

Figure 20.

4.3. Design of Mirror System

The demountable part of the reflectometer is shown in plan and side elevation in figure (21). Unique location is achieved by placing the spherical bases of the legs in the slot configuration shown in figure (21C). The slots, made from invar, remain bolted to the vacuum system during bake-out. It was found that, after the first pumping cycle, exact replacement could be achieved many times before realignment became necessary. The reflectometer consists of two front silvered mirrors, one mounted at the end of an arm and the other fixed centrally above the axis of rotation of the arm. The central mirror can be rotated through 45° and 90° independantly of the arm and the end mirror can be rotated through 75°, again independently of the arm. The rotations of the mirrors are set as accurately as possible by using tapered pins and holes: it is estimated that the rotations are accurate to within 0.05°. The arm moves on a brass bearing and can rotate about an axis A. Stops on a thick back plate define the angle through which the arm rotates. The total system including the stops can again rotate about A on a main bearing of brass set co-axially with the axis of rotation of the arm. The tilt and position of this main bearing can be adjusted and fixed as shown in (21b).

4.4. Alignment of Reflectometer

The first step in the alignment is to ensure that the reflectometer arm rotates through 180°. The photo-multiplier was

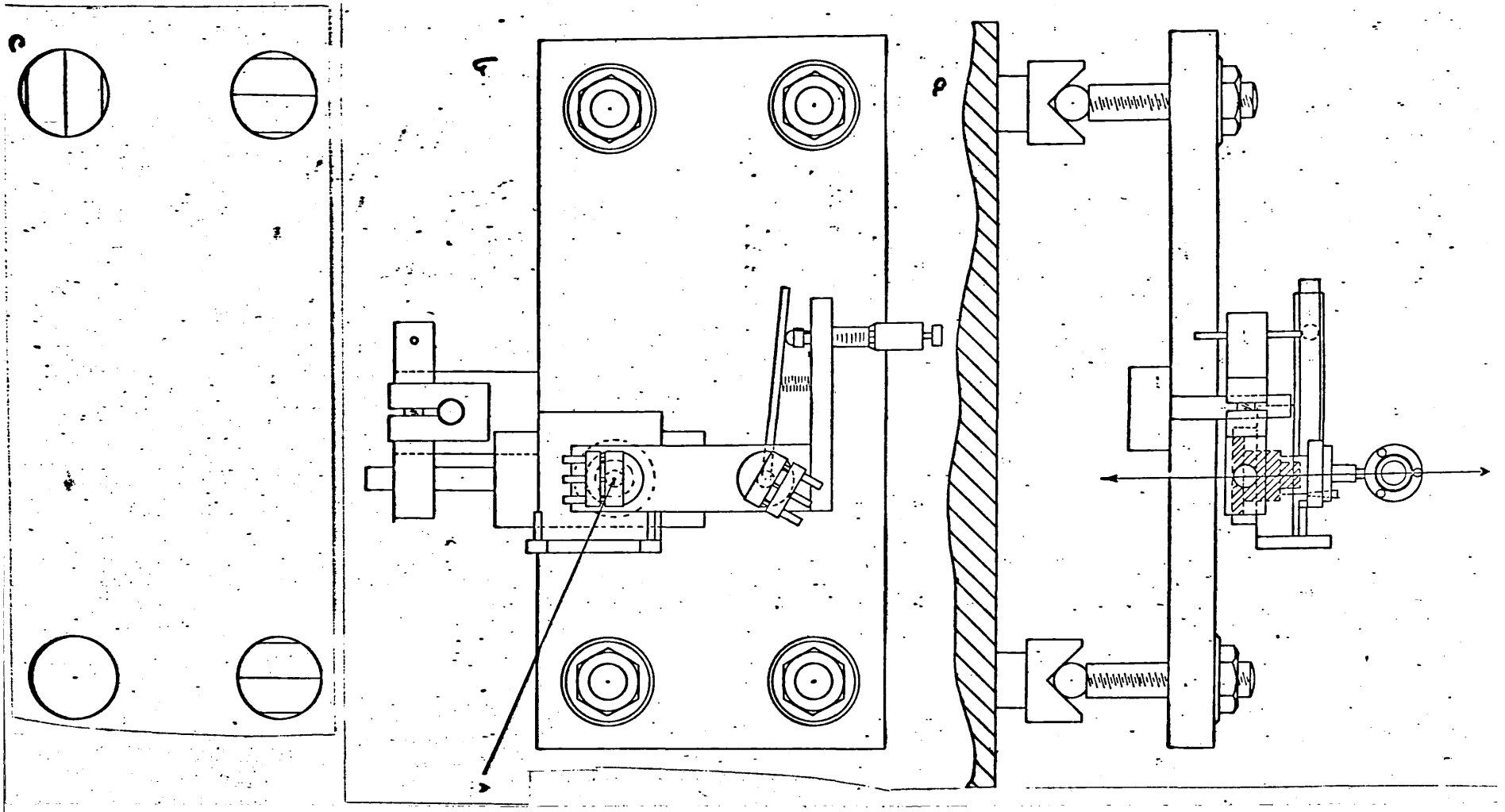

Figure 21.

replaced by a He-Ne laser and a ground glass disc with a 1mm hole drilled centrally is fixed in the position previously occupied by the diffusing screen used for detection. This hole, together with the slit S (figure 20), defines a line which is to be made perpendicular to the line $m_1' m_1$. Light from the laser is used to define this line, and is incident normally on m_2 , this being achieved by making the incident and reflected beams coincident. Using the tapered pins and holes the mirror m_2 is rotated through 45° so that the light is now incident on m_1 . m_1 is set normal to the beam by again making the incident and reflected beams coincident. The reflectometer arm is rotated through approximately 180° and m_2 through 90° to the position m_2' . The arm stop is set in such a position that the incident and reflected beams are coincident with no adjustment of m_2 . This procedure ensures that the angle of rotation is 180° to better than 0.1°, since the beam displacement is $\sim 4r\,\delta\Theta$ where $\delta\Theta$ is the difference from 180°, and r the distance of the laser from m_2 . The line defined by m_2 , S and the screen aperture is now made to coincide with the bisector of the angle $m_1 S p\, m_1'$ as follows. A reflector is placed in the sample position and light from the filament source L is reflected from it at an angle of incidence of 75°. m_1' is now adjusted until the beam passes along the line $m_2' S$. The sample is removed from the beam and the "sample out" configuration obtained as follows. The reflectometer arm is rotated through 180° and m_2' through 90° to the position m_2 ,

m_1' is also rotated, through 75° to the position m_1. If the reflectometer is correctly orientated the beam will now emerge from m_2 along the line $m_2 S$. The whole mirror system is rotated on the main bearing until this condition is achieved. It may be necessary to move the whole system in a direction perpendicular to the line $m_2 S$ in order to ensure that light is incident on the same spot for both positions of m_1. The axis of rotation of the reflectometer arm is made perpendicular to the plane of incidence at this stage by observing the position of the beam on the diffusing screen for the "sample in" and "sample out" configurations. The system is now locked in position. The angle of incidence is set using a horizontal scale calibrated in mm, positioned 1.8 metres from the centre of the sample. The mirror system is shown in position in figure (22).

4.5. Source Optics

The light source used was a quartz halogen lamp enclosed in a water cooled housing. The lamp is powered by two stabilized power supplies (Farnell N30/10) connected in parallel through Zener diodes. The intensity drift using this system was generally found to be less than 1%/hour. However, some lamp instability was found to occur on occasions. A deterioration in bulb quality or oxidation of electrical contacts in the vicinity of the bulb were found to be the most likely causes of this instability. The collimator comprised a slit and a lens of focal length ~20cms manufactured from spectrosil B. The beam divergence was estimated

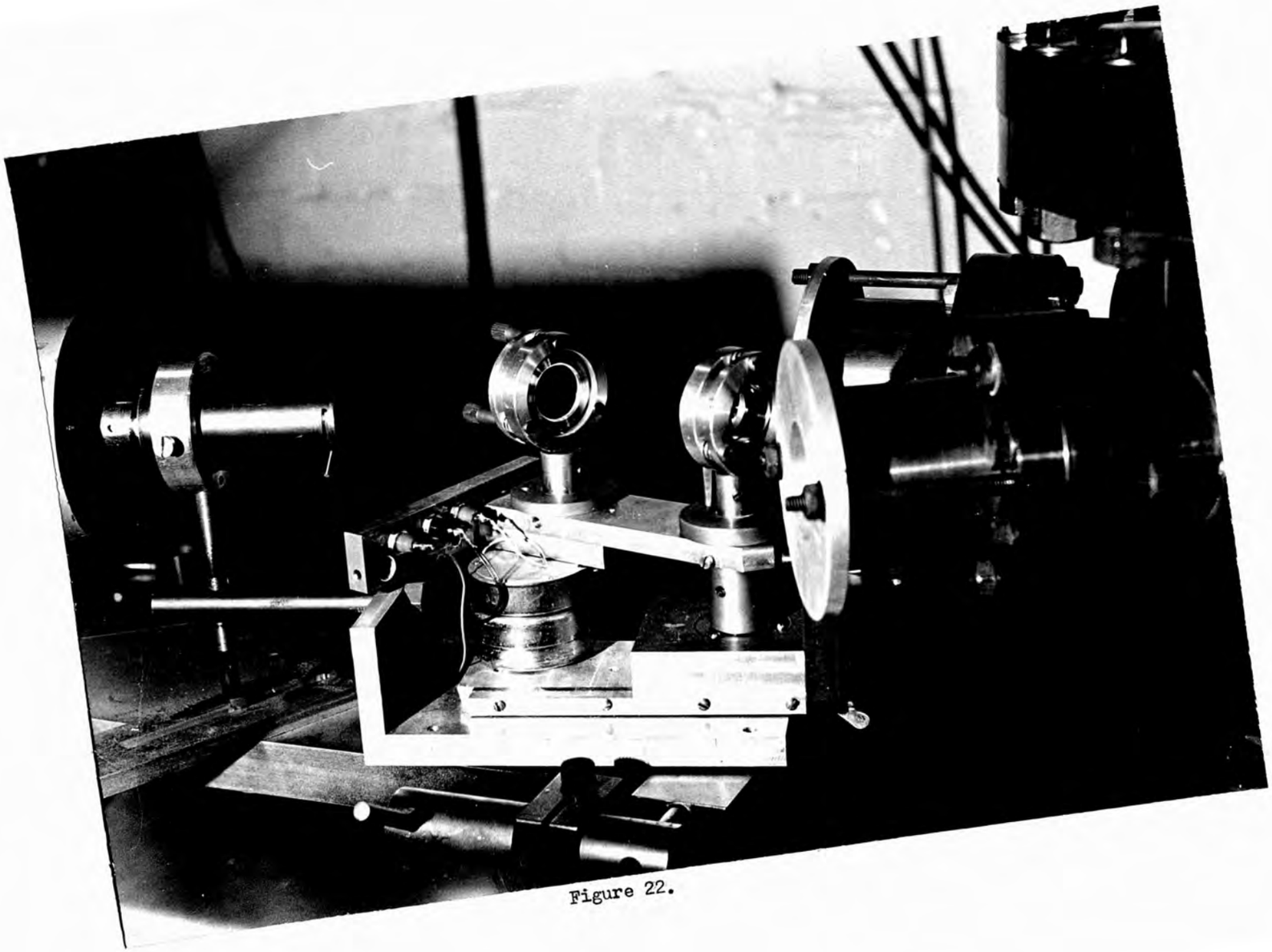

Figure 22.

to be considerably less than 0.1°. The monochromater comprised a circular graded interferance filter (Barr and Stroud type CGS1) which produced monochromatic radiation in the range 4000Å - 7000Å. The band width of the radiation was typically 150Å and the transmission of the filter ~25% throughout the spectral range. The whole range could be obtained for a 300° rotation of the filter. The filter was mounted on a bearing, the axis of which was made parallel to the optical axis of system. The bearing was rotated by a bi-directional electric motor mounted co-axially with a precision circular potentiometer. The speed of the motor was fixed at 0.2 revolutions/minute. The output from the potentiometer indicated the angular setting of the filter to a degree of precision very much better than the band-width of the filter. The light was polarised by a 5mm square Glan Thompson prism fitted with a small circular aperture. The procedure adopted for obtaining polariser settings perpendicular and parallel to the plane of incidence was as follows. The polariser was set approximately to give light polarised perpendicular to the plane of incidence (this setting could be obtained by reflection from a dielectric). The setting was noted and the polariser crossed with an analyser. The analyser was then rotated through 180° about an axis perpendicular to the plane of incidence. The polariser was then adjusted to give extinction and the setting again noted. The mean of the two polariser settings was the required setting for the component perpendicular to the plane of incidence.

The polarizer was set accordingly and the procedure repeated until no resetting of the polarizer was needed on rotation of the analyser. At this stage the errors likely to occur from errors in the polariser settings are considered by noting that the reflection coefficient for light polarised at an angle to the plane of incidence is given by:-

$$R_\phi = R_{\parallel} \cos^2\phi + R_{\perp} \sin^2\phi \qquad (1)$$

Consider now the $\perp$ setting i.e. $\phi = 90^\circ$ and assume $R_{\perp}/R_{\parallel} \sim 4.0$ then if ϕ is in error by 0.5°

$$\frac{R_\phi}{R_{\perp}} = 1.00132$$

Thus the error in the reflection coefficient is less that 0.2%. It was found that the polariser settings were reproducible to within 0.1°, however, errors were likely to occur in setting the plane of rotation of the analyser perpendicular to the plane of incidence. It was also found that the polariser settings varied by less than 0.3° throughout the spectral range. If the same polariser settings were used throughout the spectral range it was assumed that errors of less than 0.2% would arise. The source optics system is shown in figure (23).

4.6. Detection System

Intensity measurements were made with an EMI (type 9558QB) photomultiplier. This tube has, typically, a quantum efficiency of~24% at 3000Å falling to~3% at 7000Å. The dynode chain was designed to give a linear high gain in accordance with the

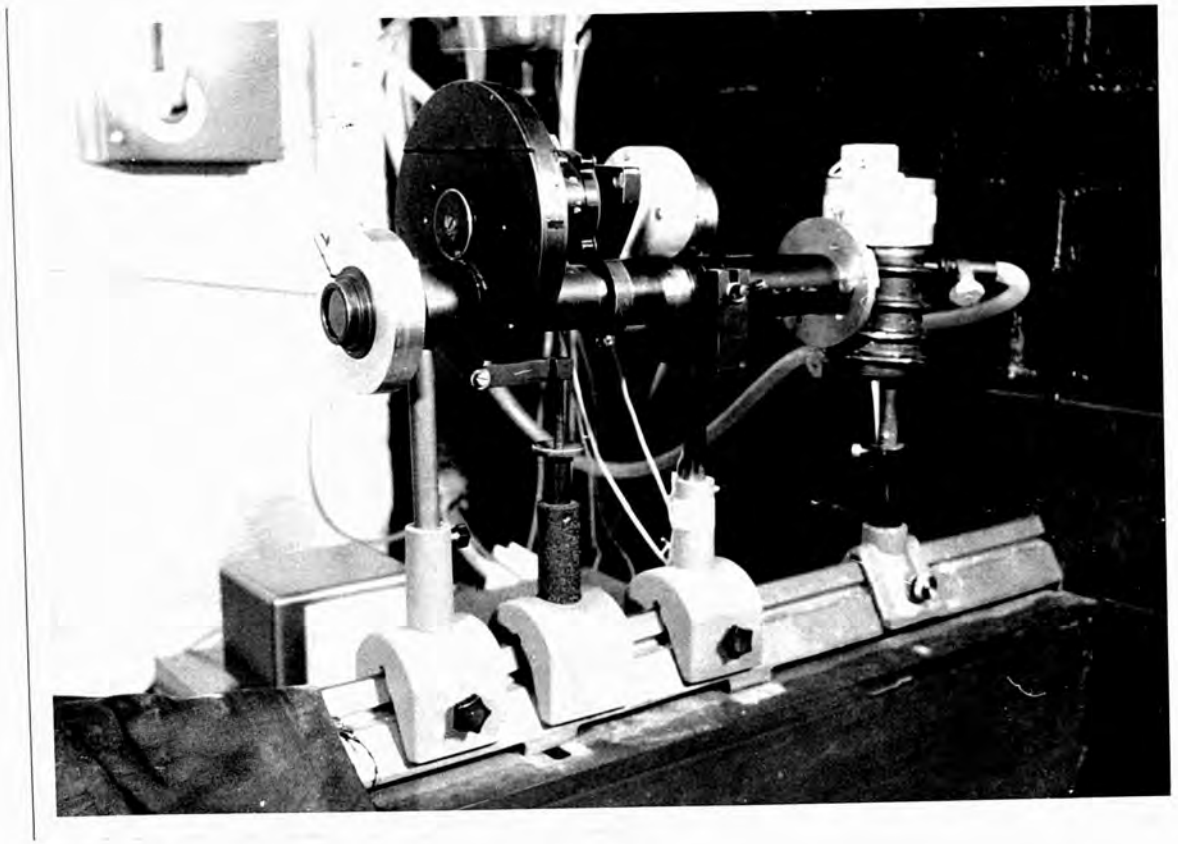

Figure 23.

recommendations given in the EMI photomultiplier handbook, and it was possible to obtain a signal to noise ratio of better than 3000. The tube was shielded with mu-metal, this being essential because of the close proximity of the ion pump magnet. The signal from the photomultiplier was fed to a chart recorder or a digital voltmeter as discussed below. A ground glass screen was fixed in front of the photomultiplier window to reduce polarisation effects and errors due to non-uniformity of the photo-cathode.

4.7. Window Calibration

The windows, of spectrosil B, were selected for their optical homogeneity. If the reflection coefficients are to be obtained from the ratio of the intensities for the "sample in" and "sample out" configurations, clearly the absorption coefficients of the two windows are ideally required to be the same. This condition may be checked as follows: the uncorrected reflection coefficient of a standard reflector was measured, the windows interchanged and the reflection coefficient again measured. The standard reflector used was a nickel film which had been allowed to oxidise by exposure to atmosphere for several days. It was assumed that the reflection coefficient of the film did not vary over the time of the measurements. The ratio of the two measurements provides a measure of the difference in absorption coefficients as follows:-

If I_o = incident intensity, the itensity of the light

emerging from W_2(Figure 20) will be given by:-

$$I_1 = \alpha_2 R_o I_o \qquad (2)$$

Where R_o = reflectivity of standard reflector

α_2 = absorption coefficient of W_2

The intensity of light emerging from W_3 is given by:-

$$I_2 = \alpha_3 I_o \qquad (3)$$

Therefore the unoorrected reflectivity will be given by:-

$$R_1 = \frac{\alpha_2}{\alpha_3} R_o \qquad (4)$$

If the windows are now interchanged the uncorrected reflectivity will be given by:-

$$R_2 = \frac{\alpha_3}{\alpha_2} R_o \qquad (5)$$

Putting $\alpha_2/\alpha_3 = x$ (the appropriate calibration factor) then (4)÷(3) gives

$$x^2 = R_1/R_2$$

$$x = \sqrt{R_1/R_2} \qquad (6)$$

Thus the reflectivity of the "standard" reflector need not be known, the only requirement being that its reflectivity remains constant with time. The quantity x was measured for light polarised at 45° to the plane of incidence throughout the range 4000Å → 7000Å. For all points sampled, x differed from unity by less than 0·2% and showed no systematic variation with wavelength. The calibration was checked periodically to ensure that thin film deposits had not occured and that the windows had not become strained to differing degrees.

4.8. Choice of Mirrors

Clearly, a major source of error in the system is differences in optical path for the "sample in" and "sample out" configurations. These will occur if the angles of incidence on m_1 and m_2 for the two configurations differ. The two most commonly used mirror materials are silver and aluminium. The optical constants of these materials (Heavons 1955) were used to calculate the change in reflectivity resulting from a 0.5° change in angle of incidence for an angle of incidence of 45°. The results of this calculation are shown in figure (24). From the curves we see that silver gives a uniformly small error over the whole spectrum range and for this reason silvered mirrors were used. Aluminium would, of necessity, be used for work below 4000Å because of the decrease in the reflectance of silver which occurs below this wavelength, and we note that the errors in reflectance coefficients are decreasing in this range. The mirrors were prepared by thermal evaporation of silver at a pressure $< 10^{-5}$ T.

4.9. Reflectometer Operation

Figure (21) shows an arm attached to the mirror m_1. This arm is rotated by a micrometer screw, thus enabling the mirror to be rotated slowly. This was necessary because of the optical leverage exerted by the two mirrors. When taking measurements, m_2 was fixed in the appropriate position using

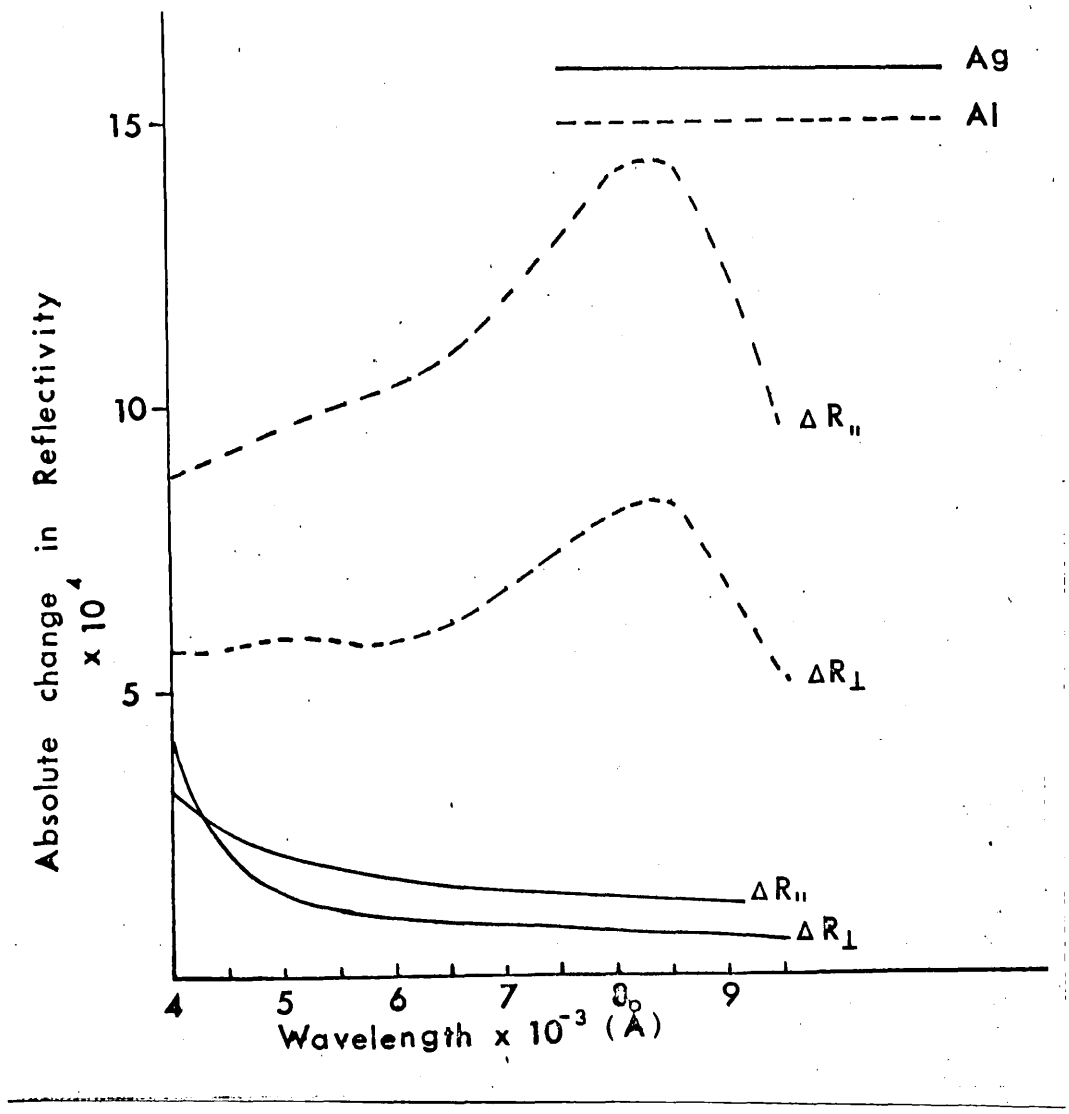
Ag
Al
15
10
5
Absolute change in Reflectivity
x 10⁴
ΔR∥
ΔR⊥
ΔR∥
ΔR⊥
4
5
6
7
8
9
Wavelength x 10⁻³ (Å)

Figure 24.

the tapered pin, and m_1 was then rotated slowly about the correct position and the output from the photomultiplier fed to a chart recorder. (Panax Servoscribe SREC-2p) In this way peaks were obtained on the chart, the maximum height of which represented the intensity to be measured. This procedure was adopted in order to reduce errors due to the variation in sensitivity of the photo-cathode across its area. Typical output peaks are shown in figure (25). From this figure we see that the best accuracy obtainable with this system is 0.2%. This is clearly the major source of error in the system. However, such an accuracy is sufficient for the accurate determination of optical constants. At a later stage the chart recorder was replaced by a digital voltmeter (Solartron LM1480.3). This voltmeter is capable of detecting the maximum or minimum values of time-varying signals. The micrometer and [illegible] were replaced with a bi-directional electric motor having a speed of 0.1 revs./minute.

With these modifications, reflectivities could be obtained to better than 0.1%.

4.10 Sample Replacement

Good reproducibility of sample position was needed, and this was achieved using the system illustrated in figure (26). The sample is fixed at the end of a rod which can be raised and lowered by means of a stainless steel bellows. The rod can be rotated about an axis in the plane of the sample and perpendicular

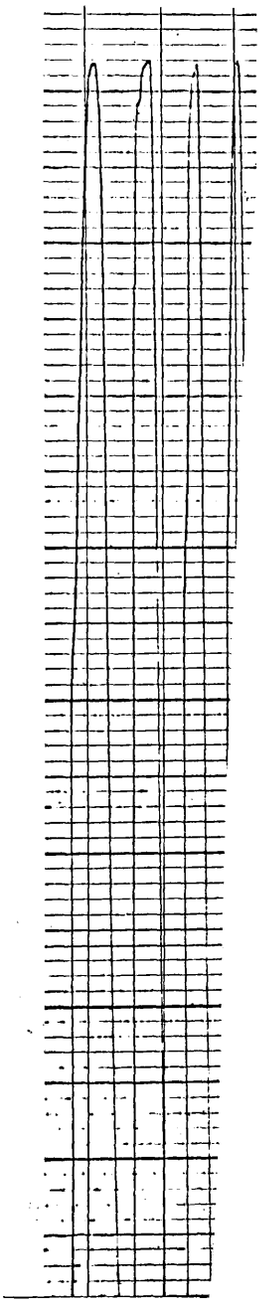

Figure 25.

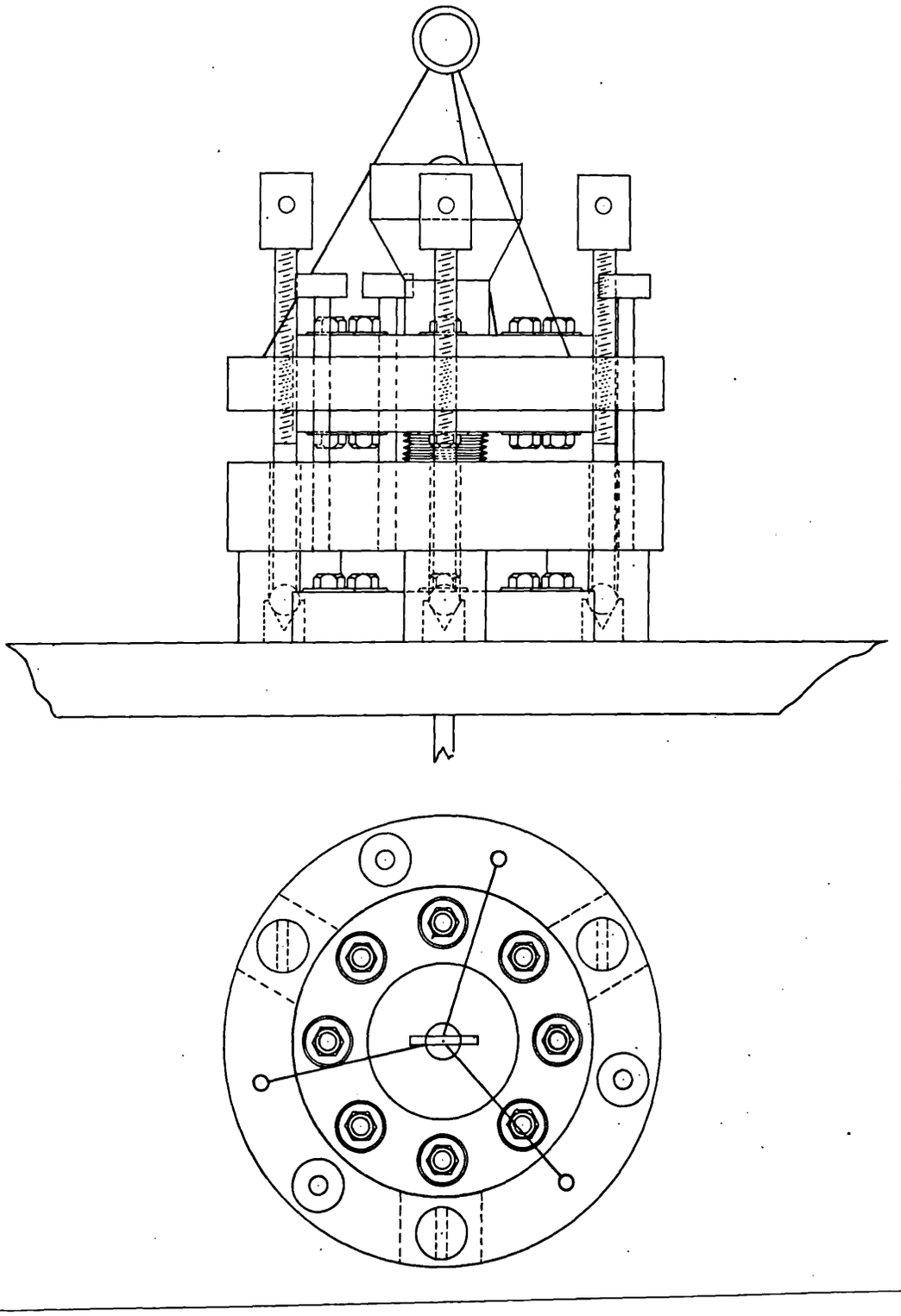

Figure 26.

to the plane of incidence. Outside the vacuum system the bellows are supported by three steel legs at the vertices of an equilateral triangle. Spheres are fixed at the bottom of each leg; these in turn rest in conical holes. Tilt adjustment can be achieved with the three legs. The legs are a loose fit in three guiding tubes, which allow the smooth raising and lowering of the sample for various tilt adjustments. A pulley system is used to raise and lower the sample.

4.11 Reflectance Ratio Measurements

As mentioned in (3.3.) reflectance ratio measurements are easier to make than measurement of reflection coefficients. The photomultiplier is fixed in a position to receive light at the appropriate angle of incidence and the intensities are measured for the parallel and perpendicular polariser settings. However, in general, the intensities of the incident components are not equal. This can be overcome by plane polarising the light at 45° before polarising in the parallel or perpendicular directions. Alternatively a calibration experiment may be performed whereby the actual intensity ratio is measured. Depolarisation is another possibility and some success was achieved in this direction by using a perspex light pipe, but, some polarisation of the incident beam always remained. It was decided that the direct incident beam calibration was most convenient since the use of the polariser tended to yield

non-reproducible results. This was because the incident intensities varied rapidly with the setting of the first polariser, and this in turn was wavelength dependant. The windows were checked for dichroism by measuring the incident ratio of the light before it entered W_1 and after it emerged from W_3, the ratios measured were the same to better than 0.1%. For the ratio method it is important that there is no beam movement when the polariser is rotated. The Glan Thompson prism was therefore replaced with a sheet of polaroid for reflection ratio measurements.

CHAPTER V

THE PREPARATION OF THE SPECIMENS BY THERMAL EVAPORATION

5.1. Introduction

Any determination of the optical constants of a material requires the preparation of a surface free from contamination and the maintenance of that surface for a period of time sufficient to complete the measurements. The methods available for surface preparation have been reviewed by Roberts (1963). In the present work, surfaces have been prepared by thermal evaporation in ultra-high vacuum. The high reactivity of some of the materials studied made this method the most suitable.

5.2. The Thermal Evaporation Process

The conditions that must be realized for the generation of clean surfaces by thermal evaporation have been discussed by Heavens (1955) and his results are summarized here. The variables most likely to affect the optical properties on an evaporated film are:-

(i) Nature and pressure of residual gas in chamber.

(ii) Intensity of beam of atoms condensing on surface.

(iii) Nature and condition of target surface.

(iv) Temperature of evaporation source.

(v) Contamination of evaporated material by supporting material of source.

In the present work, these variables were controlled as far as possible in the following ways:

(a) Evaporation was carried out in ultra high vacuum $\sim 10^{-10}$ τ and the residual gas monitored with a mass spectrometer.

(b) A uniform high evaporation rate was used for all evaporations ~700Å/minute.

(c) The substrate was subjected to rigorous cleansing procedures.

(d) The temperature was made to be consistent with (b)

(e) Lengthy outgassing procedures were employed and careful shuttering used during evaporation.

5.3. Evaporation Chamber.

The attainment of ultra-high vacuum $\sim 10^{-10}$ τ was achieved as follows. A 12" diameter stainless steel chamber was rough pumped with an Edwards alumina-trapped rotary pump. At a pressure of approximately 10^{-3} τ a Varian Triode ion pump was started. This pump had a pumping speed of 140 litres/s at high pressure, and a pressure of 10^{-6} τ was quickly attained with the system isolated from the rotary pump with a bakeable valve. At this stage the Bayard-Alpert gauge, used for total pressure measurement, was outgassed by electron bombardment. Titanium sublimation pump filaments were also outgassed at this stage. The system was then baked at 250°C until a pressure ~5 x 10^{-8} τ, (indicated by the ion pump current) was attained. The length of time needed

to achieve this depended critically on the cleanliness of the system. The system was allowed to cool and the gauge again outgassed. The pressure after cooling was $\sim 10^{-9}$ T. The titanium sublimation pump (T.S.P.) was then used for ~12 hrs. with the ion pump to reduce the pressure to $\sim 10^{-10}$ T. At this stage liquid nitrogen was fed to a stainless steel baffle inside the chamber. This baffle was situated directly above the T.S.P. filament. The condensation of gas onto this baffle further reduced the pressure to $\sim 4 \times 10^{-11}$ T. Low pressure measurements were made with a modulated Bayard-Alpert ionization gauge. Either copper con-flat gaskets or gold wire seals were used on all the ports. In order to reduce the time taken to achieve minimum pressure the following practices were adopted.

(i) The materials used for structures in the UHV chamber were carefully chosen for their low outgassing properties and low vapour pressure. Wherever possible, stainless steel was used for major structures and oxygen-free high conductivity copper for electrical connections. Stainless steel components were first degreased by ultrasonic agitation in a degreasing agent (DECON 90) and then a smooth surface produced by electropolishing in ortho-phosphoric acid. The components were finally washed in distilled water.

(ii) The system was normally let up to atmospheric pressure with dry nitrogen, and was sealed as quickly as possible.

Pumping was typically restarted within 90 minutes of first letting the system up to atmospheric pressure. Although perfect clean room conditions were not obtained, care was taken to keep the room as dust free as possible, the ports and the main chamber being covered with polythene whilst experiments were assembled. All flanges in contact with gold wire seals were cleaned with fine grade emery cloth wetted with iso-propyl alcohol. All tools used in the assembly of experiments to go into the chamber were ultrasonically cleaned in a degreasing agent. Rubber gloves and face masks were worn during assembly.

These procedures allowed the system to be pumped to its base pressure within about 36 hours, this time including a 12 hr. bake. However, when the system was left at atmosphere for times in excess of 2 hrs. it was found necessary to bake for approximately 36 hrs.

An A.E.I. "MINIMASS" mass spectrometer was used to obtain a residual gas analysis of the chamber. Figure (27) shows a typical mass spectrum for the system at its base pressure. The peak at mass number 18 is identified unambiguously as water vapour. That at 28 may consist of N_2^+/CO^+ or $C_2H_4^+$. However, the ions N_2^+ and N^+ (mass number 14) should occur in the ratio 10:1 so the absence of a significant peak at mass number 14 indicates that $C_2H_4^+$ and CO^+ were present to a greater extent than nitrogen.

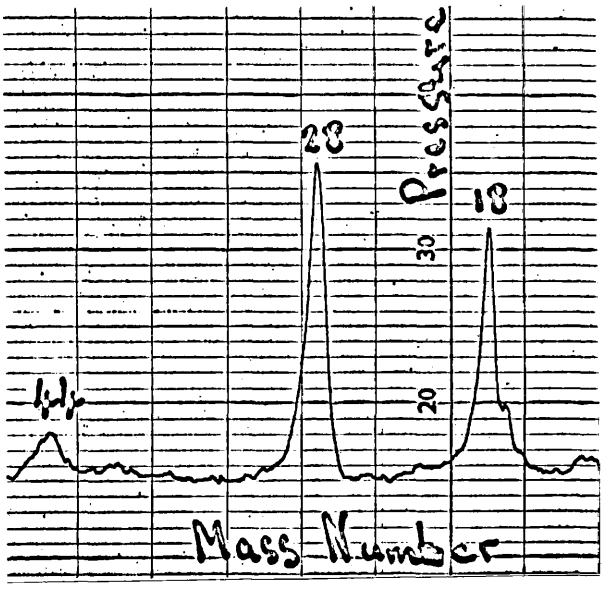

Figure 27.

The peak at mass number 44 is largely due to CO_2 but the hydrocarbons $C_3H_7^+$ and $C_3H_5^+$ may be contributing to this peak. The hydrogen peak is obtained separately from the rest of the mass spectrum. Hydrogen did not greatly contribute to the residual pressure except during the operation of freshly installed T.S.P. filaments. We note the possible pressure of a small quantity of oxygen. Several methods were tried to reduce the water vapour peak. Baking through the backing line, repeated flushing with dry nitrogen and extended baking failed to improve the situation. Estimates given below show, however, that the partial pressure of water vapour should not greatly affect the film composition. The relative sizes of the peaks at 28 and 18 varied from cycle to cycle but these two peaks always dominated the mass spectrum.

5.4. Filament Preparation

Evaporation took place from a tungsten helical coil heated to high temperatures by Joule heating. The coils had an internal diameter ~2mm and a length of ~$2\frac{3}{4}$cms. The filaments were first outgassed in an ordinary high vacuum system at a pressure of better than 10^{-5} τ. The coils were held at red heat for approximately 15 minutes. A rod of the material to be evaporated was then inserted in the helix and the temperature increased until the rod melted, thus wetting the tungsten with evaporant. This procedure was repeated with further rods until globules of evaporant prevented further packing. The globules were then

held in a liquid state for approximately 30 seconds to complete the outgassing. Throughout the outgassing a microscope slide was fixed above the filament so that observation confirmed that excessive quantities of evaporant were not lost during outgassing. The highest melting point metal studied in this work was terbium, which melts at 1450°C. Tungsten melts at 3380°C, so that, at first sight, it would appear that contamination of the film by the tungsten filament is unlikely. However, it is known that in the evaporation of aluminium (melting point 660°C) from tungsten filaments, some tungsten dissolves in the aluminium. Heavens (1952) has shown, using radioactive tracer techniques, that the solid solution loses the charge material preferentially during evaporation and the extent of contamination of silver and germanium films by tungsten source materials was less than a few parts per million. Film contaminations of this order are considered to have negligible effects on the optical properties of evaporated films. The most likely contaminant, particularly for the rare earth metals terbium and gadolinium, is the oxide of the evaporant. This is expected to be minimised by the outgassing procedure. Filaments prepared in this way were stored in high vacuum until immediately prior to installation in the ultra-high vacuum chamber. The evaporation system is shown in figure (28). Figure (29a) shows a filament ready for installation in the U.H.V. system.

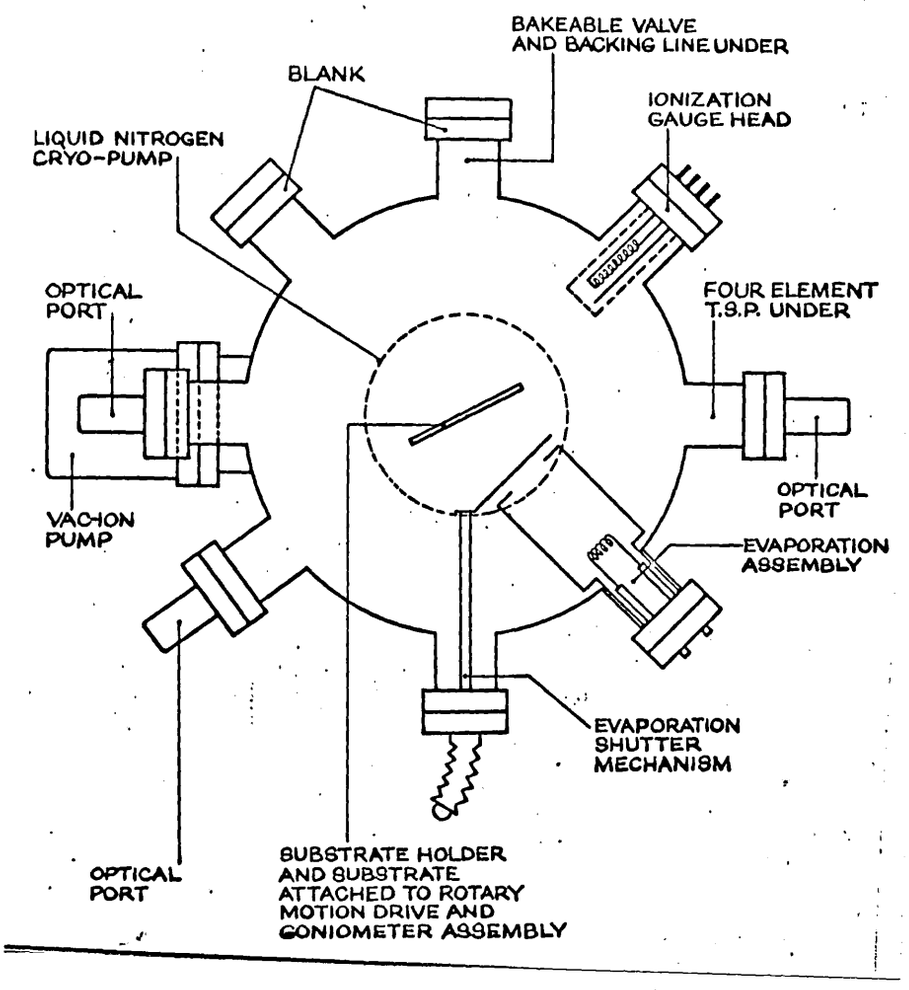
BAKEABLE VALVE
AND BACKING LINE UNDER
BLANK
IONIZATION
GAUGE HEAD
LIQUID NITROGEN
CRYO-PUMP
OPTICAL
PORT
FOUR ELEMENT
T.S.P. UNDER
OPTICAL
PORT
VACION
PUMP
EVAPORATION
ASSEMBLY
EVAPORATION
SHUTTER
MECHANISM
OPTICAL
PORT
SUBSTRATE HOLDER
AND SUBSTRATE
ATTACHED TO ROTARY
MOTION DRIVE AND
GONIOMETER ASSEMBLY

Figure 28.

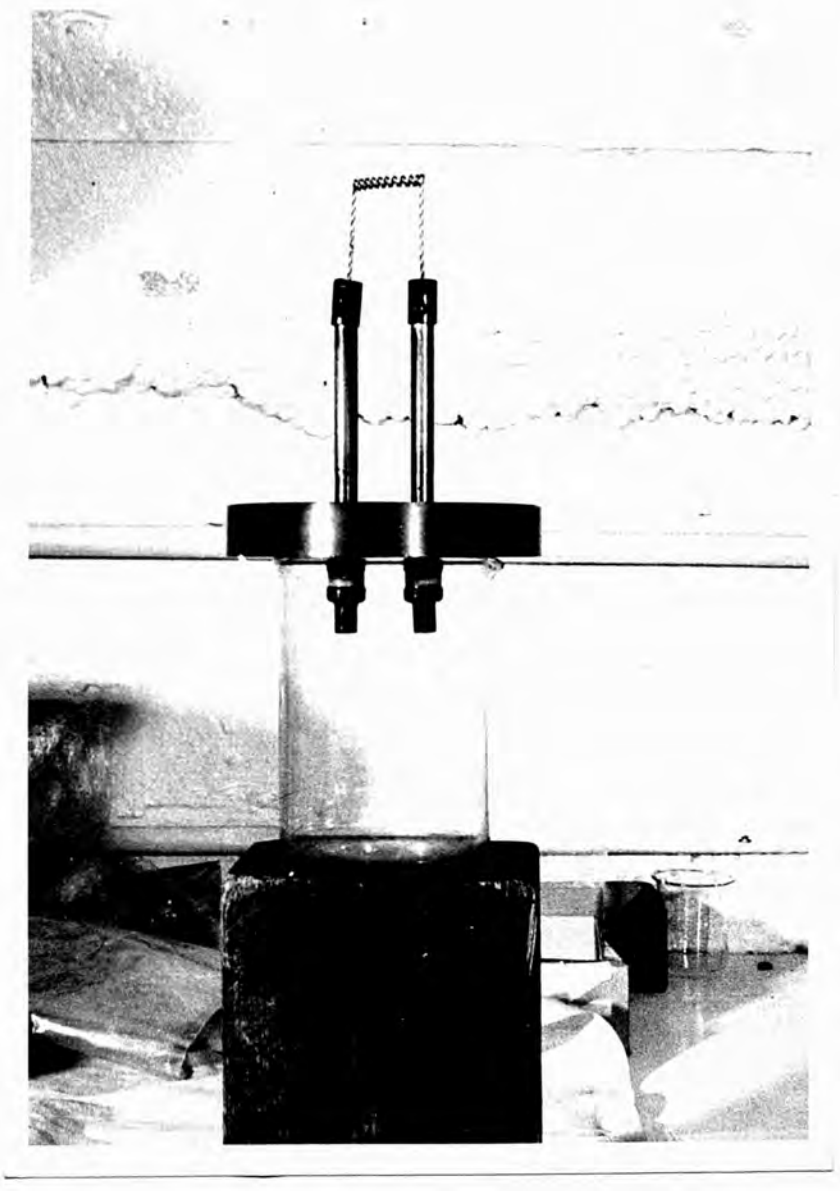

Figure 29.

5.5. Substrate Preparation

Float glass microscope slides were used as substrates throughout this work. They were prepared as follows. Two slides were selected for their cleanliness and freedom from scratches. These were then clamped vertically in a beaker of degreasing agent (DECON 90) and ultrasonically cleaned for about an hour. The degreasing agent was then displaced with distilled water and the substrates rinsed for ten minutes. They were then again cleaned ultrasonically, this time in distilled water. The substrates were then stored under distilled water until approximately fifteen minutes before installation in the ultra-high vacuum chamber. The slides were then removed from the distilled water and it was checked that the water flowed uniformly from the slide surface. They were then allowed to dry in air, covered loosely with lens tissue. Prior to installation, dry nitrogen was blown across the slide surface to complete the drying. One slide was then taken and examined under a bright light source for scratches and water marks. The slide was then checked for the uniform condensation of water vapour (the breath test). The remaining slide was then checked for scratches and water marks and fitted to the substrate holder described below.

5.6. Substrate Holder

Figure 30 shows a substrate mounted in its holder.

Figure 30.

The holder is of stainless steel and comprises a block with a channel cut deep enough to take four microscope slides. These are fixed with two steel bars screwed to the block. The substrates were lightly clamped to reduce strain effects. The holder is fixed to the rotatory drive as indicated in figure 30 and the mounting was constructed so that the front face of the substrate passed through the axis of rotation of the drive. Substrate heating always proves difficult in ultra-high vacuum bedause of outgassing problems. For this reason a new type of heater was developed. A microscope slide was coated with nichrome to approximately 2000Å by evaporation in ordinary high vacuum. To produce a mechanically hard film the slide was heated to 250°C during evaporation. The resulting slide was then used as a substrate heater by passing current through it. It was found that substrate temperatures of approximately 300°C could be readily achieved using this system. Contact on the nichrome was achieved by clamping copper bars to the film. Annealed gold wires were used for electrical contacts to the low tension currents feed-throughs. The source-substrate distance was fixed at $5\frac{1}{2}$".

5.7. Film Purity

A necessary condition for an evaporated film to be free from contamination by the residual gas in the chamber is that the atoms of the evaporant have a long mean free path compared with the source substrate distance. An estima-

shows that this condition is satisfied even at 10^{-4} τ so the contamination produced by collisions with the residual gas molecules during evaporation may be ignored. However, if we consider the rate at which gas molecules strike a surface then the pressure limitations become stricter. From kinetic theory we see that the number of molecules striking unit area in unit time, N, is given by:-

$$N = \frac{\rho}{(2\pi mkT)^{\frac{1}{2}}} \qquad (1)$$

Where T is the absolute temperature of the gas and ρ its pressure, m the mass of a molecule and k Boltzmann's constant. From (1) we see that low mass numbers are the most important. Typically the partial pressure of water vapour was 5×10^{-11} τ. Using this figure in (1) we get:-

$$N = 2.4 \times 10^{10} \text{ molecules/sec.}$$

If we take the area covered by a water vapour molecule to be 1.5 sq. Å, the time for formation of a monolayer of water vapour is 78 hrs, assuming unit sticking probability. The appropriate figure for nitrogen at the same partial pressure is about 98 hrs, thus we see that, at the pressures attained in the chamber, the films will be free from contamination by the residual gases if experiments are completed in less than about 60 hrs.

5.8. Film Thickness

The analyses given in Chapters II and III apply to

reflection from films in which multiple reflection can be ignored. The thicknesses for which such conditions hold have been discussed by Taylor(1971). Generally the following relationship should hold:-

$$\frac{d}{\lambda} > .2 \qquad (2)$$

d = film thickness

λ = wave-length of incident light.

The shortest wave-length used in this work was 4000Å. Thus the minimum thickness required is 800Å. Physically, as well as optically, these films are thick and effects due to the finite mean free path of the electrons may be ignored. In general completely opaque films were grown in order to ensure that the condition (2) held. In addition, film thickness measurements were made using multiple beam Fizeau fringes (Tolansky 1963). This method also allowed the smoothness of the surface to be assessed. The step in the film necessary for such determinations was introduced by placing a microscope cover slip under one of the steel bars shown in figure (30). Figure (31) shows a typical multiple beam interferogram of a terbium film grown in the U.H.V. chamber.

5.9. Film Growth

The conditions necessary for the production of an opaque, continuous, thick film were determined by performing several trial runs in ordinary high vacuum. The filament, prepared as described above, was inserted into the vacuum system and the

Figure 31.

system pumped to its base pressure. Further outgassing of the filament was then found to be necessary. Typically the conditions required for evaporation of the rare earth metals were achieved by passing~55 Amps for 2 mins. through the filament. On passing ~30 Amps through the filament with the shutter in position the pressure rose to approximately 10^{-6} τ. On reaching this pressure the current was switched off and the system allowed to return its base pressure. This procedure was repeated until no pressure burst was observed. The current was then increased and the same process repeated until 50 Amps could be passed without a significant pressure burst. The outgassing was limited to 50 Amps because evaporation occured at greater currents. The filament was then left to outgas at 50 Amps, for about 5 mins. From mass spectrum observations it was noted that H_2O, N_2 and H_2 were evolved during outgassing. The substrate was then rotated into position and the shutter opened and the current increased to 55 Amps. A pressure rise was usually observed as the evaporation proceeded, possibly caused by further outgassing from the filament or by outgassing from the container due to heating from the filament. If the pressure approached 10^{-8} τ the current was switched off and the system returned to its base pressure. The process was repeated until the substrate had been exposed to the filament for two minutes at 55 Amps.

Usually the evaporation could be allowed to proceed so that the film was deposited in one evaporation.

CHAPTER VI

THE OPTICAL PROPERTIES OF TERBIUM AND GADOLINIUM IN THE VISIBLE PART OF THE SPECTRUM

6.1. Introduction

Terbium and Gadolinium are classified as heavy, rare earth metals. The rare earth elements, sometimes called the lanthanides, are those elements having atomic numbers in the range 57 to 71. The electronic structure of the rare earths may be written:

$$Xe\ (1s\text{-}4d)\ 4f^{n}5s^{2}5p^{6}5d^{(1)}6s^{2}\ ,\quad n = 0 \rightarrow 14$$

The Xenon terms may be written:-

$1s^2\ 2s^2\ 2p^6\ 3s^2\ 3p^6\ 3d^{10}\ 4s^2\ 4p^6\ 4d^{10}$ (all filled) plus $5s^2\ 5p^6$.

We note the zero population of the 4f level. At lanthanum the 4f state has a higher energy than the 5d level, so that the 4f state remains empty. The addition of another electron and proton to the system makes it energetically favourable for the electron to enter the 4f state. There is also a tendency for the electron in the 5d level to be transferred to the 4f level; hence the configuration of Cerium, ($Z = 58$) is

$$Xe\ (1s\text{-}4d)\ 4f^{2}\ 5s^{2}\ 5p^{6}\ 5d^{(0)}\ 6s^{2}$$

Thus the rare earths are typified by the progressive filling of the 4f level.

There is also a tendency to retain the stable half-filled or full configurations and hence to repopulate the 5d level, so that, for gadolinium, we have the configuration

$$Xe\ (1s\text{-}4d)\ 4f^{7}\ 5s^{2}\ 5p^{6}\ 5d^{1}\ 6s^{2}$$

For terbium the 5d electron is again transferred to the 4f level, giving:-

$$Xe\ (1s\text{-}4d)\ 4f^{9}\ 5s^{2}\ 5p^{6}\ 5d^{(0)}6s^{2}$$

Gadolinium ($z = 64$) is the first of the heavy rare earths in the periodic table, and those that follow it have hexagonal close-packed (h.c.p.) crystal structures, with the exception of Ytterbium. (This element is divalent and, together with europium, is exceptional since the remaining rare earths are trivalent.)

At lanthanum the empty 4f shell is situated outside the Xenon $5s^{2}\ 5p^{6}$ shell, but for the remainder of the series the 4f electrons lie within the Xenon core. This is because an electron added to the 4f shell cannot screen the remaining 4f electrons from the added positive nuclear charge. This phenomenon, known as the lanthanide contraction, causes the metallic radius to decrease with increasing atomic number. This contraction is interesting theoretically since gadolinium exhibits ferromagnetism and terbium exhibits ferromagnetism and antiferromagnetism, and it is the 4f electron which gives rise to their magnetic properties. However, the 4f levels are buried deep in the atom and the coupling mechanism between atoms, which is necessary for magnetic order to exist, cannot occur by direct overlap of the electrons in the incomplete shell (as it does for Ni, Co and Fe) and some other exchange mechanism is essential. This then forms the broad theoretical interest in the heavy rare earths. In addition, the scarcity of optical data, the increasing availability

of the pure metals and the recent energy band structure calculations provide the motivation behind this experimental study of terbium and gadolinium.

6.2. The Growth of Gadolinium Films

The preparation of the Gadolinium films was described in Chapter V. A typical set of results is given here and the reproducibility between different sets of data is discussed below.

The growth conditions for the film discussed here, were as follows:-

i) The residual gases were H_2O, N_2, CO and CO_2: and the partial pressures as follows:-

$$H_2O < 1.2 \times 10^{-10}\ \gamma$$

$$N_2 \text{ and CO (mass 28)} < 8 \times 10^{-11}\ \gamma$$

$$CO_2 \text{ (mass 44)} < 2 \times 10^{-11}\ \gamma$$

The total integrated pressure measured on the Bayard-Alpert ionization gauge was $< 3 \times 10^{-10}\ \gamma$ (modulated reading).

ii) The film was grown from a 99.9% pure sample, obtained from the Koch-Light laboratories.

iii) An evaporation current of 55 Amps was passed for 120 secs, during which time the pressure, measured on the linear scale of the Bayard-Alpert gauge, remained at $8 \times 10^{-9}\ \gamma$. The film was deposited in one evaporation.

iv) The measured film thickness was 1400Å (an evaporation rate > 10Å/sec.)

v) Visual inspection showed that the film was free from pin-holes on removal from the ultra-high vacuum chamber, but pin-holes were formed quite rapidly on exposure to air.

vi) The film was grown on a cold substrate.

vii) The system returned to its base pressure within 20 secs of completion of evaporation.

viii) Room temperature was observed to be 27°C throughout measurements, and thus the gadolinium remained in the paramagnetic state.

6.3. Method of Measurement

The reflection ratio method of measurement was used for determinations on this film. The voltage from the photo-multiplier was measured with a digital voltmeter. Measurements were made for angles of incidence of 76° and 68°, measured to $\pm$ 0.25° using the calibrated head on the rotary drive. The incident beam was calibrated to give the incident intensity ratio at energy steps of o.1 eV. The calibration factor varied by 1.6% throughout the spectral range, this being a much smaller variation than that in the reflection ratio. Measurements were completed at one angle, the angle changed, and measurements made at the other angle. This procedure was thought preferable to obtaining both measurements at the same time for each wavelength, because movement of the sample could cause spurious effects through small differences in the angle of incidence and beam movements

with respect to the sample surface. The measurements on this film were completed within 4 hours of growth so that it can be stated with some certainty that the film was not affected by the residual gas in the system.

6.4. Reflectance Ratio Measurements

Figure 32 shows the "raw data", which was used as input for the programme described in Chapter III, which returned values for n and k from values of reflectance ratio at given angles of incidence. We note the large variation in reflection ratio for an angle of incidence of 76° compared with that at 68°. We also notice the structure occuring in both curves. The point at 2.6 eV was remeasured and found to be correct to within the experimental uncertainty of the measurements. The error bars shown were estimated by measuring the same ratio several times and the resulting uncertainty was found to be $\sim 0.3\%$. The values of n and k shown in figures 33 and 34 were derived from the observed reflectance ratios. The calculated optical conductivity curve is shown in figure 35a and is discussed below.

6.5. Specimen Reproducibility

At this stage it is appropriate to discuss the extent to which results given here are typical of all the samples measured. In all, 20 films of gadolinium were grown and their optical properties measured. About half were measured using the ratio method and the remainder using the reflection coefficient

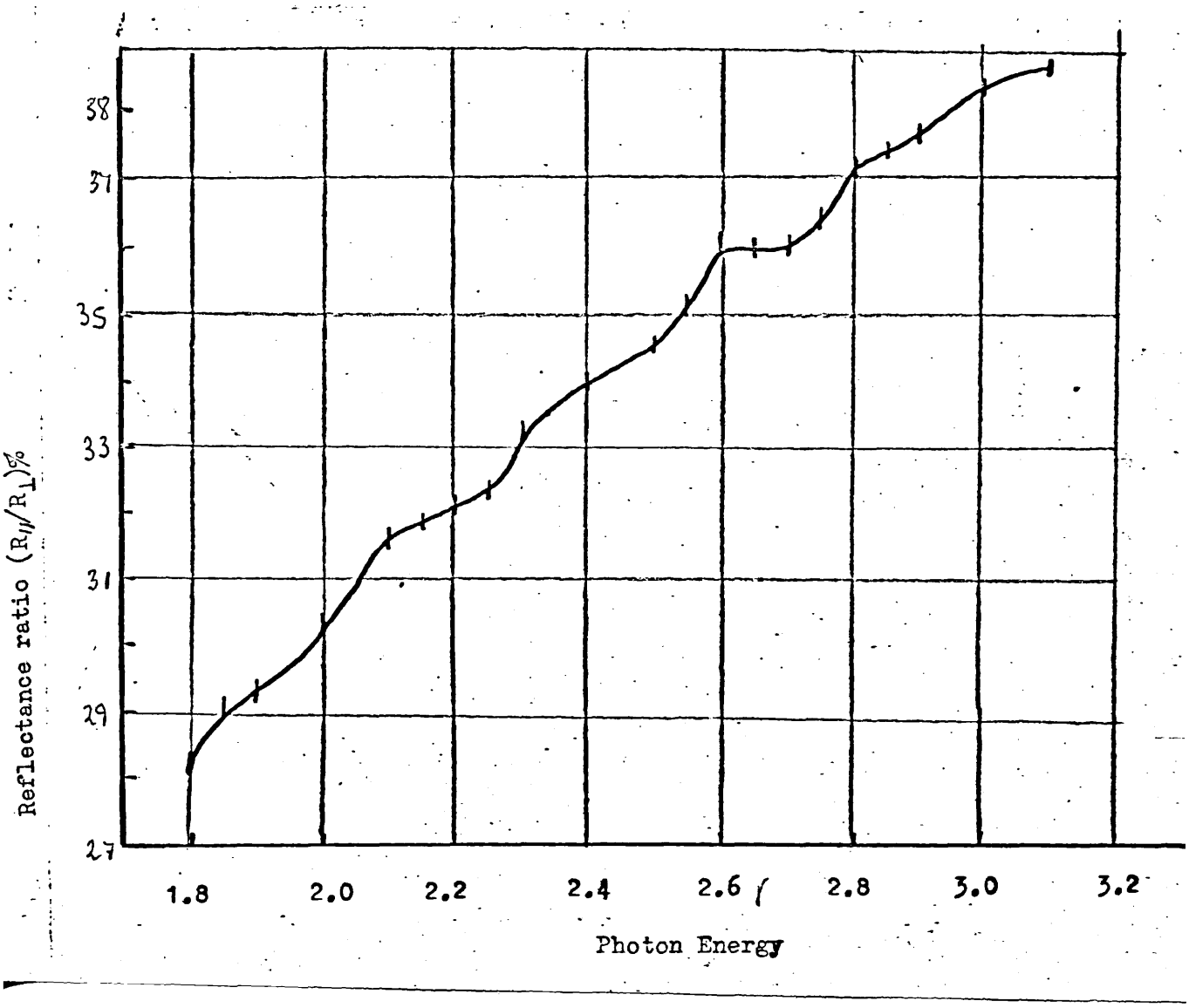

Figure 32(a). Reflectance ratios at 76° measured for gadolinium.

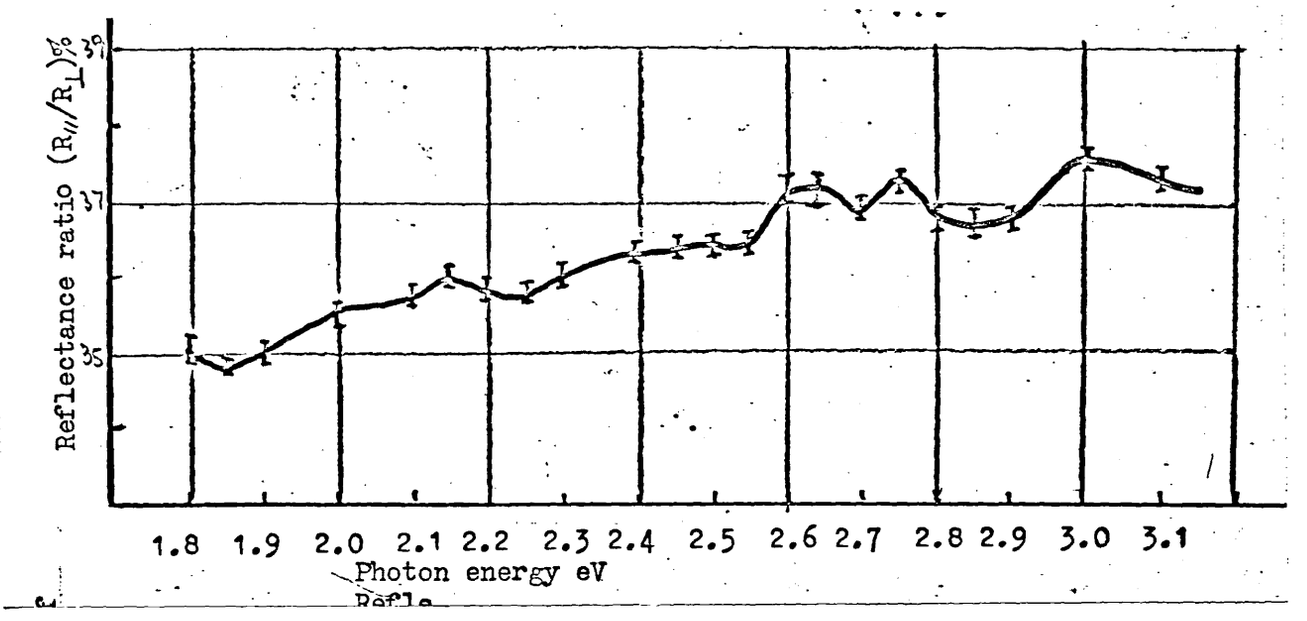

Figure 32(b). Reflectance ratios at 68° measured for gadolinium.

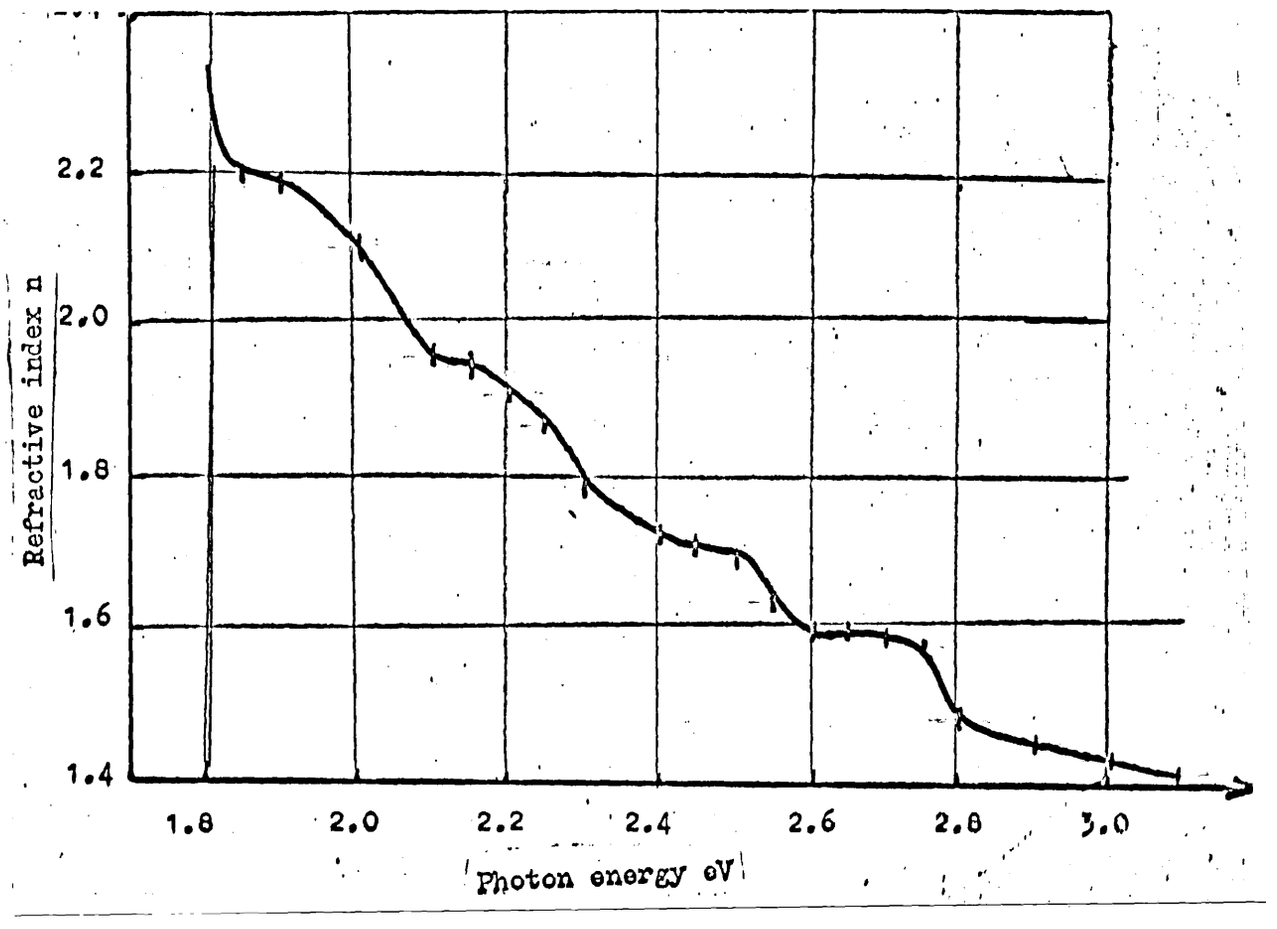

Figure 33. Variation of n with photon energy for gadolinium.

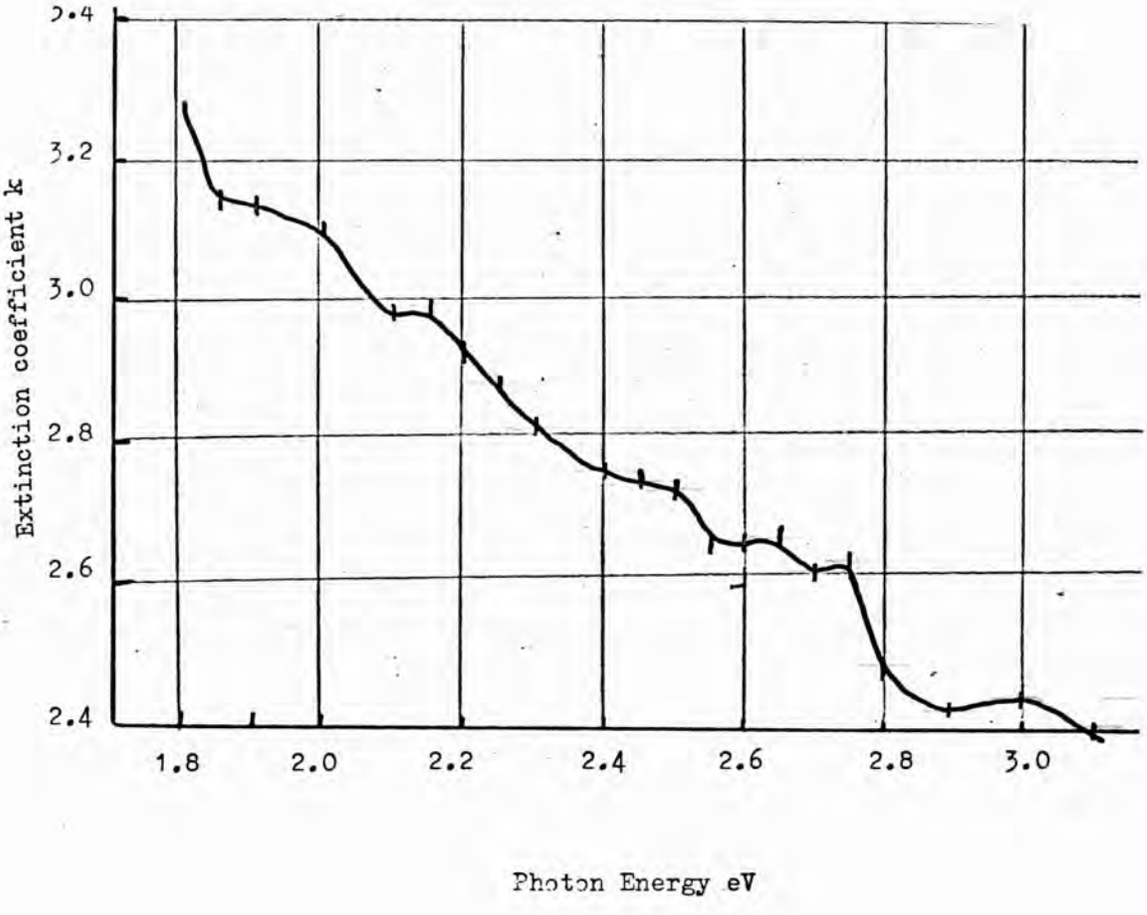

Figure 34. Variation of k with photon energy for gadolinium.

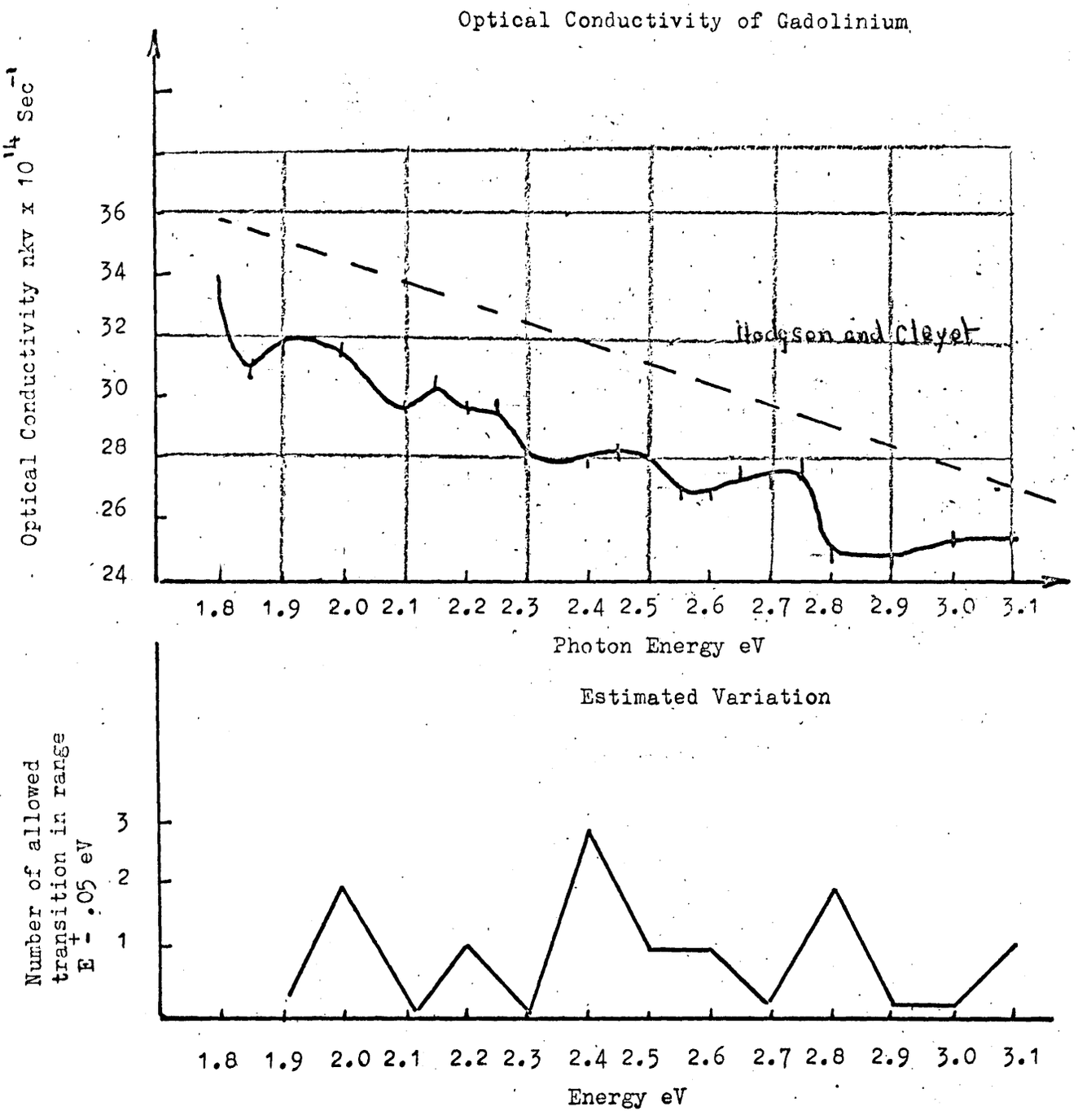

Figure 35. Variation of optical conductivity with photon energy
a) observed ,b) estimated , peak positions.

method.

Some results had to be discarded because they were made on samples grown over platinum contacts used for resistivity measurements. In order to keep the contacts on the glass substrates intact, cleaning could not be carried out after evaporation in ordinary high vacuum. The effects of the platinum contacts could be seen as a transparent region round the contacts. In addition, subsequent analysis showed that the optical constants of films grown over the contacts were not reproducible. Most of the results derived from the reflection coefficient method were obtained before the installation of the circular filter described in Chapter IV, so that only a few points throughout the spectral range could be measured using narrow band filters. These results agree numerically to within 10% with the data given here, but no conclusions can be drawn, for these samples, about the fine structure in the optical conductivity curves. There remained seven sets of data, five of which were in good numerical agreement and showing similar structure in the optical conductivity curves. The remaining two films appeared contaminated, probably because of inadequate substrate cleaning and the conductivity curve rose sharply at the ultra-violet end of the spectrum. The remaining five sets of data were all obtained at good base pressures and the films appeared smooth and continuous. The values of n and k derived from these films agree to within 10%. The general shapes of the optical conductivity curves remained the same, with shifts in the peak positions of $\pm$ 0.05 eV.

Thus, after initial problems with film preparation five consistent sets of data have been produced, of which the results given here are typical.

6.6. Effects of Ageing

Figure 36 shows the reflectance ratio curves of a gadolinium film obtained within 2 hours and then within 24 hours of growth, the film being left in the vacuum system at $< 3 \times 10^{-10}$ Torr. There is good numerical agreement between the two sets of data and it was concluded that ageing effects were not likely to be important. For this reason films were grown on cold substrates which had been previously outgassed. Substrate heating during evaporation caused a variable increase in the partial pressure of water vapour, and it was therefore decided that in order to produce standard conditions, films would be grown on cold substrates.

6.7. Film Surface and Structure

Scanning electron microscopy and X-ray reflection diffraction studies we made at the Fulmer Institute. This necessitated transporting the film in an evacuated desiccator to the Institutes laboratories, so that we cannot state with any certainty that the properties revealed by the study correlated to those properties which existed during measurements in ultra-high vacuum. The film studied had been stored for 48 hours in ultra-high vacuum and the growth conditions

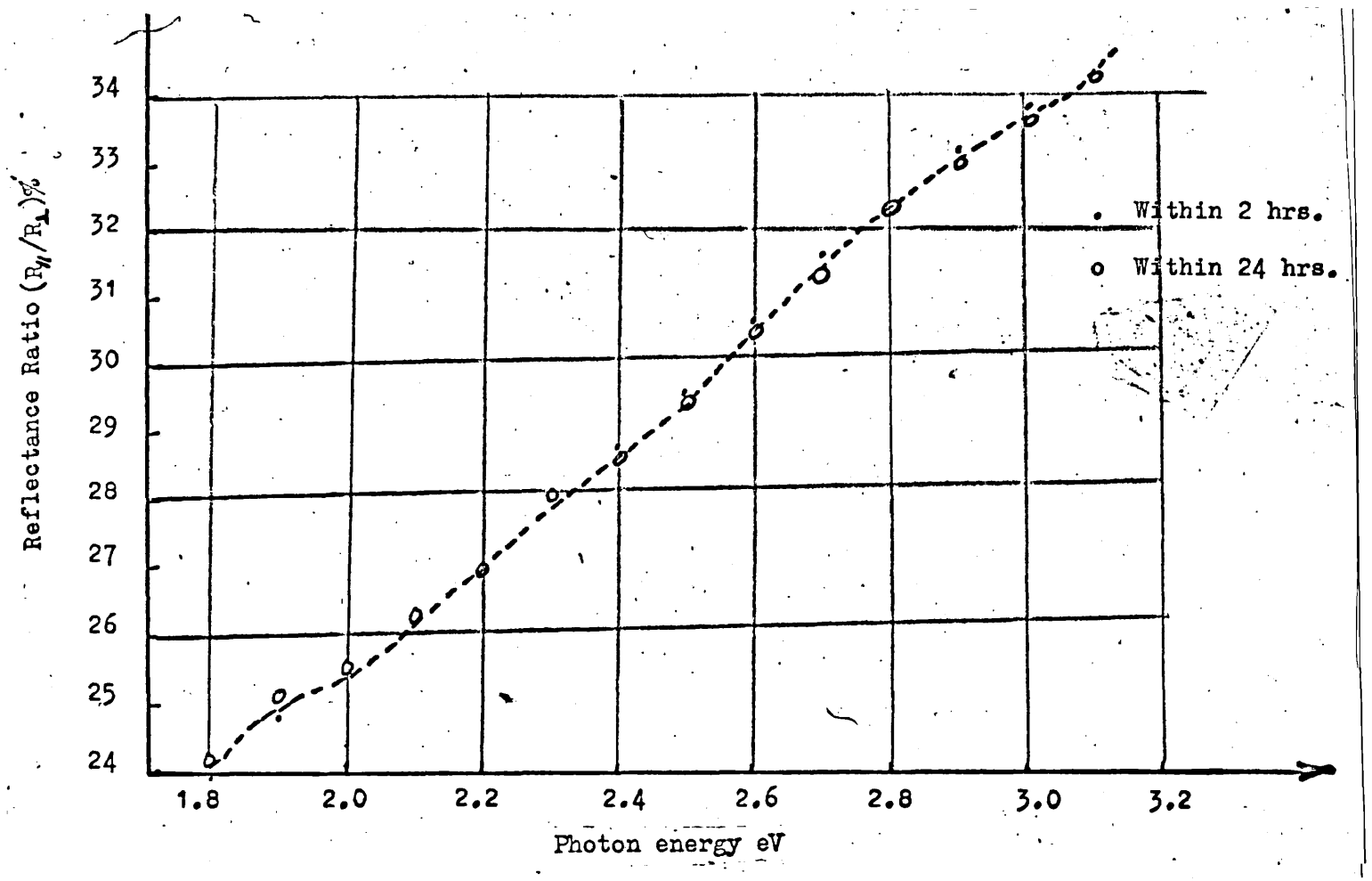

Figure 36. Effect of aging on gadolinium film.

were not significantly different from those described in 6.2. The main results of the scanning electron microscope studies may be summarized as follows:-

i) There is no significant detail on the surface of the film.

ii) One or two minor tears were apparent in the film and these were probably produced by the subsequent handling of the films. Figure 37 shows such a tear.

iii) By focussing on the tears it was possible to detect some topographical features. Figure 38 shows a blister in the film surface. These blisters were spread uniformly over the surface and have been discussed by Taylor (1972) who concludes that their effect on the optical properties will be negligible.

The results of the X-ray study were poor because of the relatively small thickness available. The film produced a weak diffraction pattern showing arced diffractions from a textured deposit. All the diffraction arcs were consistant with the h.c.p. structure of gadolinium with a c/a ratio of 1.590. Because of the poor quality of the results it was not possible to make estimates of grain size or strain. However, the observed patterns were neither unduly broadend (a characteristic of small crystallites) nor spotty (a characteristic of large crystallites). From these observations it was estimated that the film grain size was greater than 250Å in a direction perpendicular to the plane of the film and less than 150Å in the plane of the film. From

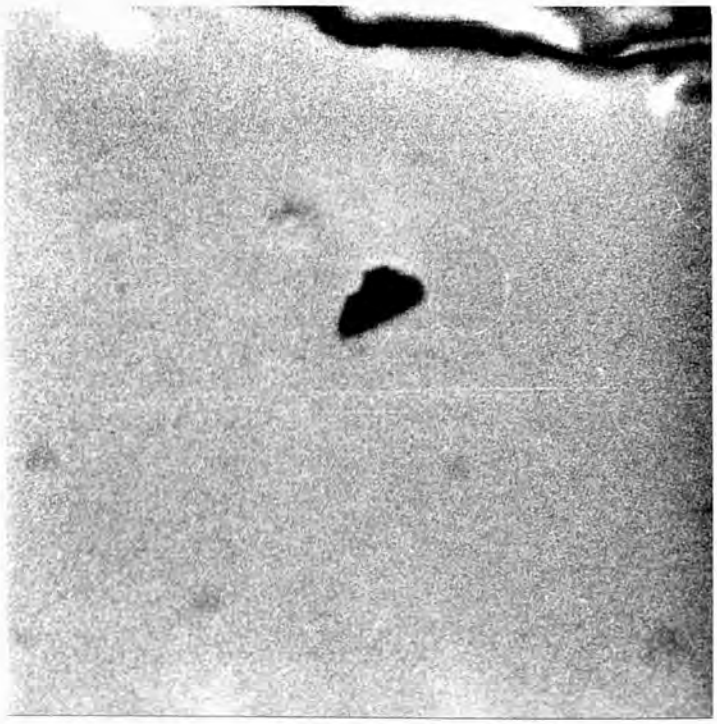

Figure 37.

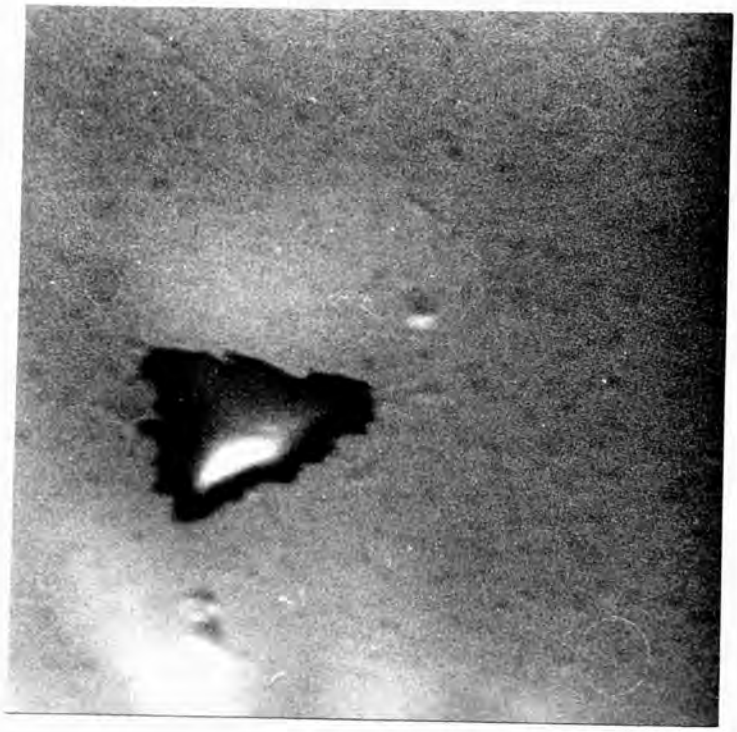

Figure 38.

Height of blisters
≈ 30 Å

the relative intensities of the diffraction arcs it was possible to infer that there was some fibre orientation with a (0001) plane parallel to the surface i.e. with the c-axis of the h.c.p. lattice perpendicular to the plane of the film. The main conclusion of this study is then, that the film was essentially polycrystalline with some degree of preferred orientation.

6.8. The Optical Conductivity Curve of Gadolinium

Figure 35a shows the optical conductivity ($n k \nu$) of gadolinium plotted as a function of photon energy. Several other workers have measured this curve and their results are discussed below. Figure 35a also shows the results of Hodgson and Cleyet (1969). We note the good numerical agreement with Hodgson's work $\sim 10\%$ and the agreement between the slope of Hodgson's curve and the average slope of the curve in the present work. Schuler (1966) obtains values which are about twice those shown here. However, Hodgson claims that Schuler's values of conductivity need some revision and this point has been conceded by Schuler. To complicate the situation we note that recent results obtained by Petrakian (1972) appear to be in good agreement with the untreated results of Schuler! It is interesting to note at this stage that the normal-incidence data used by Hodgson to compare his results with Schuler's may be insensitive to the differences in film conditions which produce changes in optical constants. The quantities $(n^2 - k^2)$ in this work also agree well numerically with those obtained

by Hodgson. Apart from the good general agreement between the results of Hodgson and the present work, we notice that the curves obtained here contain a considerable amount of structure not previously observed. Other experimenters have generally carried out their experiments over a wider energy range than here, and they have detected broad gross features in the optical conductivity curves. Schuler obtains an essentially flat curve between 2 and 3 eV, whilst Petrakian's curve has a positive slope from 2 to about 2.6 eV. This is obviously in disagreement with the present work and Hodgson's work. All the relevant sets of data are shown in Figure 39. For this figure the general levels of the curves have been adjusted so that they can be shown on the same diagram. The agreement obtained here with Hodgson's work is most welcome when we consider the disagreement between previous sets of data in the range 2 - 3 eV. In figure 35a it will be noticed that there is the possibility of structure at 2.15 eV. The assignment of a peak at this energy would be somewhat tentative since structure was not always observed at this energy. Peaks at 1.95, 2.50 and 2.75 eV were found in a majority of films measured, with only slight variations in position ($\pm$ 0.05 eV). The fact that structure occurs for all the films measured allows one to say with confidence that sensitive determinations of the optical constants of gadolinium on clean samples yields information not yet obtained by other methods. It is difficult at this stage to distinguish between the differences in the observed optical constants due to

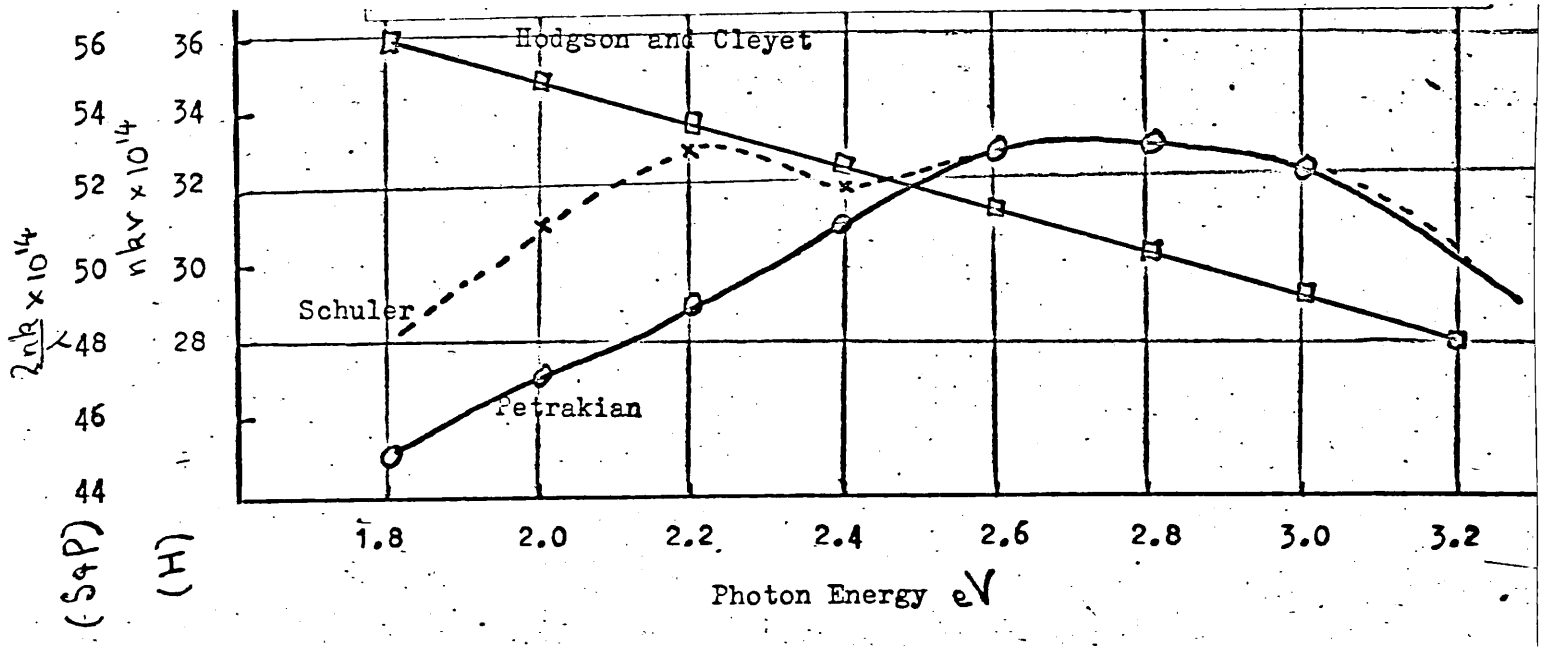

Figure 39. Previous data obtained for gadolinium.

differing methods of measurement, and differences due to dissimilar specimen surfaces. Certainly we would expect variations in the films prepared by different observers because of the different methods of preparation. Schuler states that his films were prepared in ultra-high vacuum and his determination of k requires a determination of the variation in transmission with film thickness at each wavelength. This seems an extremely tedious method of determining k, and the whole procedure whereby a layer is deposited, the optical properties measured and then another layer grown seems to warrant careful study. Petrakian makes much of the fact that his films were grown in static ultra-high vacuum $\sim 5 \times 10^{-10}$ Torr. However, it is to be inferred from his paper that the pressure rise during evaporation was $\sim 10^{-6}$ Torr. Also it must be noted that Petrakian used relatively insensitive normal incidence methods for the determination of optical constants. Hodgson used the glass-film interface of a specimen prepared on a glass prism for polarimetric determinations of optical constants. It is felt that this technique also needs careful examination to determine whether the glass-film interface yields properties typical of the bulk metal. Furthermore, the effects of the subsequent heating used by Hodgson for reducing residual resistivity are unknown, and might be important since the surface actually used for measurements will be subject to strain due to the differential expansion between the glass and the film. It is further to be noted that contamination of the measured surface may occur from the evolution

of gas molecules from the glass during heating. It is felt that because of the improved preparation and measurement techniques that the results obtained in this work are probably the best obtained to date and should be interpretable in terms of the theoretical results which have been calculated for gadolinium.

6.9. Theoretical Interpretation of the Optical Conductivity Curve of Gadolinium

As stated in Chapter I, the optical conductivity dispersion curve for visible wavelengths should be interpretable in terms of the energy band structure diagram. Band structure calculations have been performed by Dimmock and Freeman (1964). Several different starting potentials have been subsequently tried (Dimmock et al (1966)) and the results found to be generally similar. Typical of the starting potentials used is one calculated for the free atom configuration $4f^{7}\ 6s^{2}\ 5d^{(1)}$. The calculations have so far been non-relativistic and have used an augmented plane wave method, first described by Slater (1937). The results of Dimmock and Freeman are shown in Figure 40a and Figure 40b shows the appropriately labelled 1st Brillouin zone of the hexagonal close-packed crystal lattice. Each band is labelled according to the irreducible representation according to which the eigenfunctions, which generate the eigen-values, transform.

Stated differently, the crystal symmetry limits the type of wave function which satisfies the Schroedinger equation for an electron moving in a potential having the symmetry of the crystal

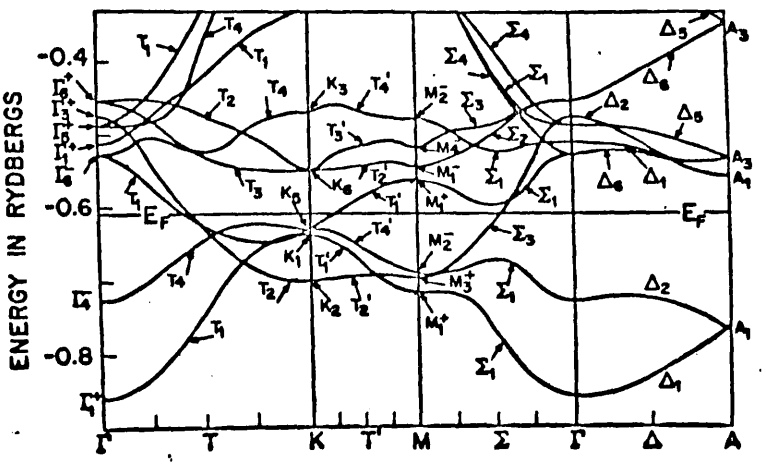

Figure 40(a).

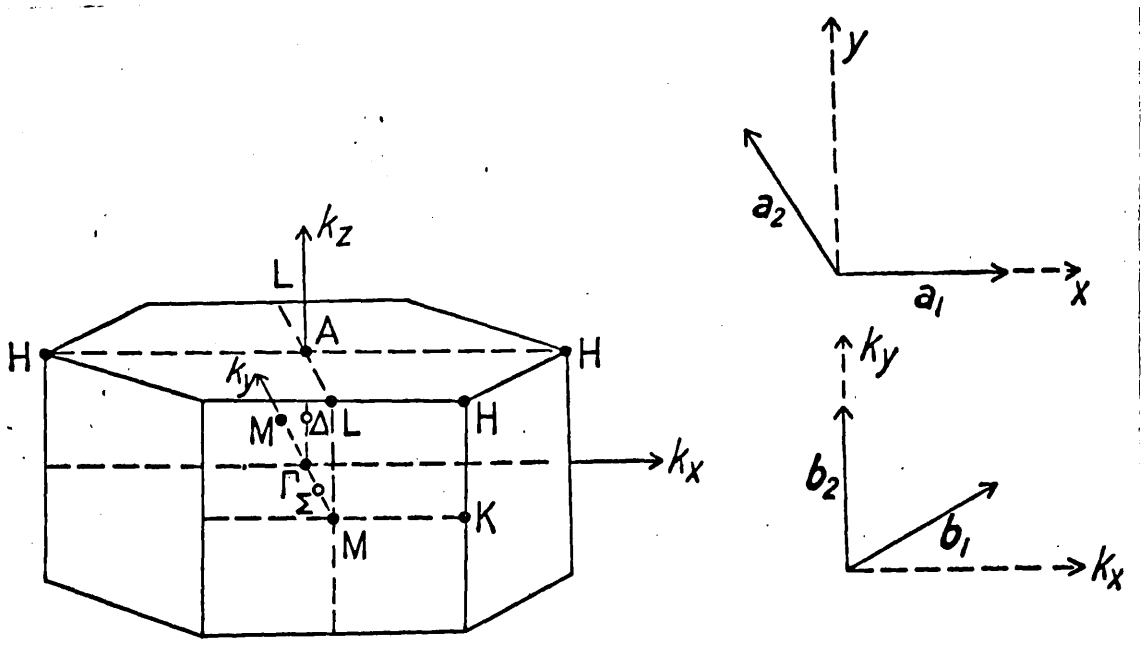

Figure 40(b).

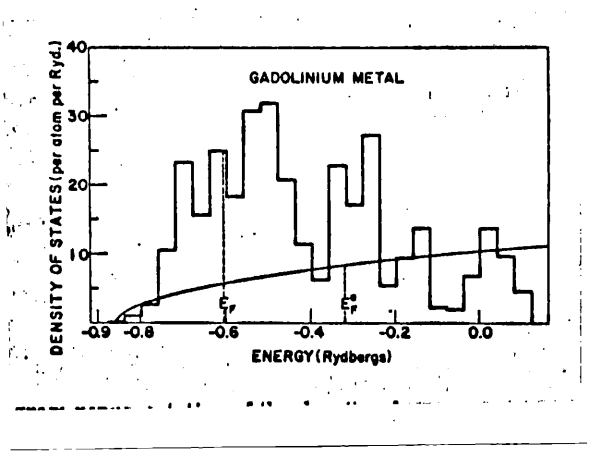

Figure 41. Density of states for gadolinium.

Symmetry Point	Radiation Direction	Allowed Transition	Associated Energy eV
	x, y	$K_2 \rightarrow K_6$	2.045
K	z	$K_2 \rightarrow K_3$	3.17
	x, y	$K_5 \rightarrow K_3$	2.24
M	z	$M_1^+ \rightarrow M_4^-$	2.79
	y	$M_2^- \rightarrow M_1^-$	1.755
	x	$M_3^+ \rightarrow M_4^+$	2.045
	y	$M_3^+ \rightarrow M_4^-$	2.385
	z	$M_3^+ - M_2^-$	2.93
L	x	$L_1 \rightarrow L_2$	2.48
	y, z	$L_1 \rightarrow L_1$	2.44
A	x, y	$A_1 \rightarrow A_3$	3.185
	z	$A_1 \rightarrow A_1$	2.84
H	x, y	$H_1 \rightarrow H_1$	2.58
	x, y	$H_2 \rightarrow H_1$	2.44

TABLE 7

lattice. The labels in Figure 40a identify the different types of wave function. From 40a we see that the bands are flat, (i.e. of zero slope) and therefore parallel at symmetry interband points such as Γ, K, M and A. Thus, we might expect structure to occur in the conductivity curve at energies corresponding to the energy difference between bands situated above and below the Fermi-level. However, there are additional selection rules which have to be considered. These depend on the symmetries of the initial and final states together with the orientation of the electric vector of the incident light wave with respect to the reciprocal lattice. The calculation of these selection rules is a somewhat lengthy theoretical exercise and has been carried out for the h.c.p. lattice by Petrakian (1972). These rules are given in Table 7 and we note that they may be changed by the presence of spin-orbit coupling. We also note that the rules given by Schuler are thought to be incorrect as are the energies read from the band structure diagram by Schuler. In view of the conflicting views on the best theoretical approach for the interpretation of optical data in terms of the band structure calculations, it was decided to adopt the following simplified procedure:-

It was assumed that all allowed transitions were equally probable and the interband optical absorption at a photon energy E was proportional to the number of allowed transitions in the range $E \pm \delta E$. Using this assumption with E set in steps of 0.1 eV

and $\delta E = 0.05$ eV Figure 35b was obtained. Clearly the peak positions deduced this way have, associated with them an uncertainty of $\pm$ 0.05 eV. The first thing we notice is the surprisingly good matching between the peak positions and those in the experimental curve. The peak at 2.0 eV can be associated with the observed structure near 1.95 eV and this can be assigned as:-

$$K_2 \longrightarrow K_6$$

and $$M_3^+ \longrightarrow M_4^+$$

The peak at 2.2 eV corresponds to the structure frequently observed at 2.15 eV and this may be written as:-

$$K_5 \longrightarrow K_3$$

Theoretically estimated structure between 2.4 and 2.6 eV is clearly seen in the experimental curve and may be assigned to the following group of transitions:-

$$M_3^+ \longrightarrow M_4^-$$

$L_1 \longrightarrow L_1$ (not shown on diagram)

$H_2 \longrightarrow H_1$ (not shown on diagram)

$L_1 \longrightarrow L_2$ (not shown on diagram)

$H_1 \longrightarrow H_1$ (not shown on diagram)

(a more complete diagram is given by Dimmock et al (1966)).

The observed peak at 2.75 eV corresponds fairly well with the estimated curve at 2.80 eV and may be assigned to:-

$$M_1^+ \longrightarrow M_4^-$$

$$A_1 \longrightarrow A_1$$

The experimental curve also shows a peak near 3.1 eV, which also

agrees well with the theoretically predicted peak near 3.1 eV which is assigned to:-

$$K_2 \longrightarrow K_3$$

Thus we see that the structure in the optical conductivity curve can be explained entirely in terms of direct k-conserving transitions at symmetry interband points in the first Brillouin zone. At this stage we can offer a tentative explanation for the slight energy variation in the peaks observed in different samples. As stated above, the optical selection rules depend on the orientation of the electric vector of the incident light wave with respect to the crystal lattice, we also note that the analysis of (6.7) showed a preferred orientation of the crystallites in the film. Thus the strength of observed transitions will depend on the type and degree of orientation in the film. If we regard the interband optical conductivity at any energy point as the sum of interband contributions centred ih the neighbourhood of that point, then the resultant peak positions will vary with the type and degree of orientation of the crystallites in the film. If then, the preferred orientations in the otherwise polycrystalline randomly orientated film vary from sample to sample the small shifts observed in the peaks are to be expected. This interpretation differs from that given by Petrakian and Schuler who both interpret their curves by assuming that the large peak in the visible is due to an average effect due to all interband transitions. Thus Petrakian averages the energies at

which allowed transitions occur and arrives at a maximum in the optical conductivity curve at 3.1 eV which is some 0.3 eV higher than his observed maximum.

The above model, based on interband transitions, would appear to generally account for the positions of the peaks in the optical conductivity curve. It is necessary, in addition, to account for the general trend of the curve i.e. its overall negative slope. There are several possible interpretations. As stated in Chapter I the overall background, upon which the above interband transitions are superimposed, may be due to non-k-conserving transitions. Alternatively, the general slope of the curve could be simply due to a systematic variation in the relative strengths of the observed interband transitions (allowing for finite line widths). A further possibility is that free carrier absorption dominates, however, an Argand plot of $(n^{\sim} - k^{\sim})$ agains $nk\nu$ does not yield a straight line and this process does not seem likely. In addition, all other workers have found an absorption edge near 0.8 eV, and free-carrier absorption must contribute less in the visible than it does at the base of this edge.

A particularly attractive interpretation of the results given here would be in terms of transitions from the 4f level to states just above the Fermi-level. Such transitions would appear as sharp absorption edges, just as observed e.g. at 2.75 eV in Figure 35a. However the photo-emission studies of

Blodgett et al (1966) indicate that transition from the 4f levels should not occur in the energy range of the present experiments. Also Blodgett et al base much of their interpretation on the assumption that non-k-conserving transitions are important. For these reasons we are drawn to our assumption made in Chapter I that the main transitions contributing to the conductivity curve are non-direct and additional structure is due to allowed transitions at symmetry interband points. Consideration of the density of states histogram obtained by Dimmock and Freeman by sampling the equivalent of 192 points throughout the Brillouin zone adds weight to this interpretation. The density of states histogram is shown in Figure 41. If the energy from the Fermi-level to the first maximum in the density of states is measured we obtain a predicted maximum at 1.5 eV. There is a maximum in the curve obtained by Hodgson at 1.55 eV. This agreement is excellent and since the results obtained here agree as to general shape above 2 eV, it is likely that this agreement would persist and that the same maximum would be obtained. This clearly implies that the background may be described in terms of non-k-conserving transitions.

6.10 Further Data on Gadolinium

At this stage, because of the importance of the observed structure, it is desirable to present some further optical conductivity curves. These are shown in Figure 42. These results were taken using a lower energy resolution and chronologically these were the first curves measured for gadolinium. The structure

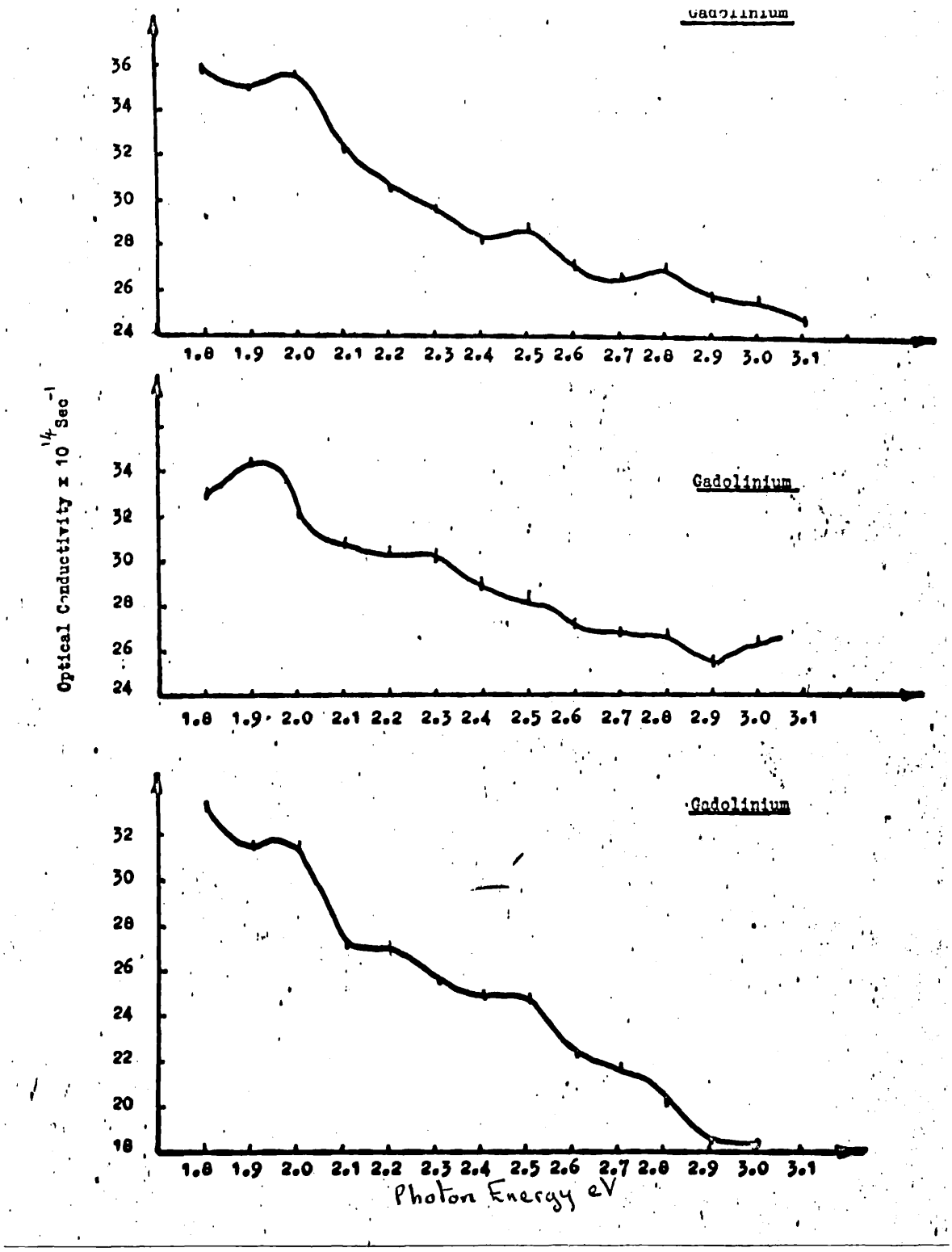

Figure 42 Further data on gadolinium.

near 1.9 eV is clearly evident, as is the 2.45 eV. There is also structure near 2.8 eV. The structure between 2.1 and 2.3 eV is not present in all the curves. Clearly from this data we have evidence for structure in the optical conductivity curve of gadolinium. These sets of data provided the motive for the higher energy resolution study described previously and we see that such resolution is needed to locate the structures precisely. The measurements by other workers on gadolinium were with larger energy steps $\sim$ 0.2 eV. From the data presented we can be fairly sure that measured on the apparatus described, gadolinium films show structure in their optical conductivity curves. In order to reduce the likelihood of systematic errors passing unnoticed, the films were removed from the UHV system and placed in an evacuated glass cell. These films were then measured by either Taylor (1972) or Hasan (Unpublished). These workers used the reflection coefficieht method described in Chapter II. A different wave length filter and polarizer was used by them and in addition some samples were measured in air, thus removing the possibility of spurious structure due to absorptions by the glass cell. Figure 43 shows the results of Taylor on a film which was measured within 6 hours of removal from the vacuum system. Clearly, there is evidence of structure in the curve and the positions correspond fairly well with those observed in this work. Thus as far as the measurements are concerned, it can be stated that the peaks observed in the optical

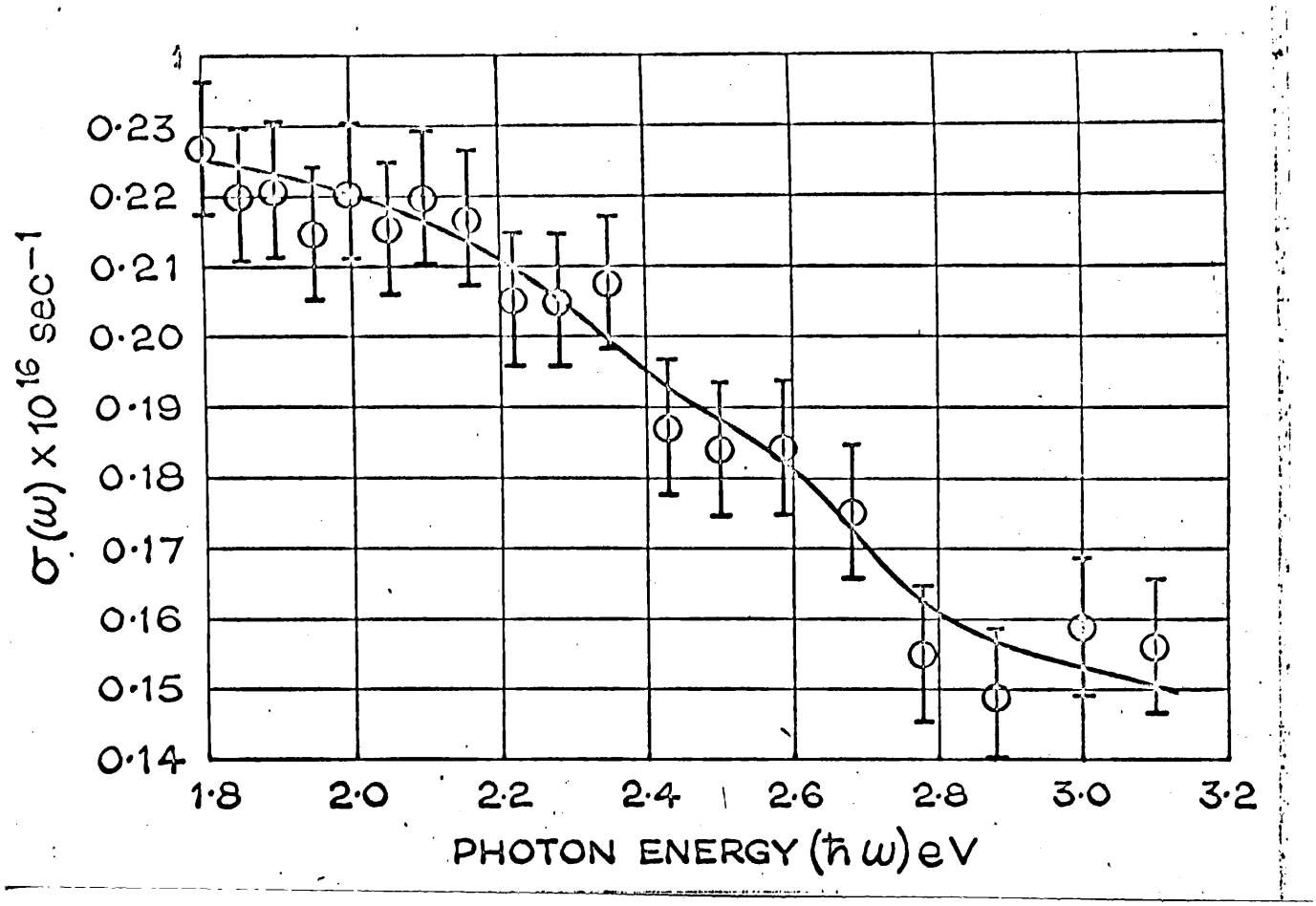

Figure 45. Optical conductivity of gadolinium measured in air, by Taylor.

conductivity curve are not likely to be caused by systematic errors in the measuring apparatus, (this is further confirmed by the work of Chapter VIII). Thus the only likely errors will be due to poor growth conditions and, as described above, great care has been taken to produce pure gadolinium films.

6.11 The Optical Properties of Terbium

Following the studies on gadolinium it was decided to investigate terbium, this being the next element in the rare earth series. There were several reasons for this. As stated in 6.1., the outer electron configuration for terbium and gadolinium may be written:-

$4f^7\ 5s^2\ 5p^6\ 5d^{(1)}\ 6s^2$ Gadolinium

$4f^9\ 5s^2\ 5p^6\ 5d^{(0)}\ 6s^2$ Terbium

However, these assignments are by no means certain and several other configurations are possible. Gadolinium for example may have an outer electron configuration as follows:-

$4f^8\ 5s^2\ 5p^6\ 5d^{(0)}\ 6s^2$.

If this is the case and the terbium configuration is as written then the only difference between the electronic configurations of the two elements is in the 4f level. Since the 4f level is deeply buried within the rare gas core we would not expect any large differences between the optical properties of the two metals if, however, the additional electron for terbium goes into the 5d shell, the energies of which are near the Fermi-level, then we might expect considerable

differences between the two elements. Thus it is of theoretical interest to compare the optical properties of the two metals. In addition, since the elements are next to each other in the periodic table, we might expect the theory which worked well for the prediction of peak positions for gadolinium would work for terbium. Band structure calculations for terbium have recently become available (Jackson 1969) and we should therefore, be in a position to apply an analysis to any terbium results. Experimental data on terbium are almost non-existent. Schuler and Petrakian in their work on gadolinium claim to have obtained data on terbium but this has not been published. Taylor (1972) obtained some preliminary results for terbium, however, the growth conditions used by him were poor and it is thought that his films may have had a considerable oxide content.

6.12 Preparation of Terbium Films

The terbium films were grown under conditions similar to those described in (6.2.). The results for a fairly typical film are given here and the specimen reproducibility is discussed below.

The base pressure of the system was measured as $< 6 \times 10^{-11}$ Torr. The mass spectrum again showed two main peaks one at mass number 18 (H_2O) and one at 28 (CO). The film was prepared from a 99.9% pure sample of terbium supplied by Rare Earth Products Ltd. A thickness $\sim$1400Å was obtained by passing a current of 50 Amps for 2 minuts, during which time the pressure in the system remained

at 3×10^{-9} Torr. The film was produced in one evaporation and the system returned to its base pressure in <30 seconds.

6.13 Specimen Reproducibility for Terbium Films

In all ten films of terbium were grown. Again five sets of results were discarded because these had been grown over platinum contacts. Of the remaining five sets of data four sets showed structural similarities. The remaining film was exceptional and when visually examined it had a contaminated appearance.

6.14 Results on Terbium

The reflection ratio method was again used for angles of incidence of 75° and 69°. The observed reflectance ratios are shown in Figures 44 and 45. The values of n and k derived from these ratios are shown in figures 46 and 47.

6.15 The Optical Conductivity Curve for Terbium

The optical conductivity dispersion curve for terbium is shown in Figure 48a. A peak near 1.9 eV is evident and this was found to vary in position from sample to sample by $\pm$ 0.05 eV. Another peak is evident at 2.2 eV and the energy variation of this peak is again found to be $\pm$ 0.05 eV. The peak near 2.45 eV did not vary in position and was clearly evident in all samples measured. Structure can only be assigned

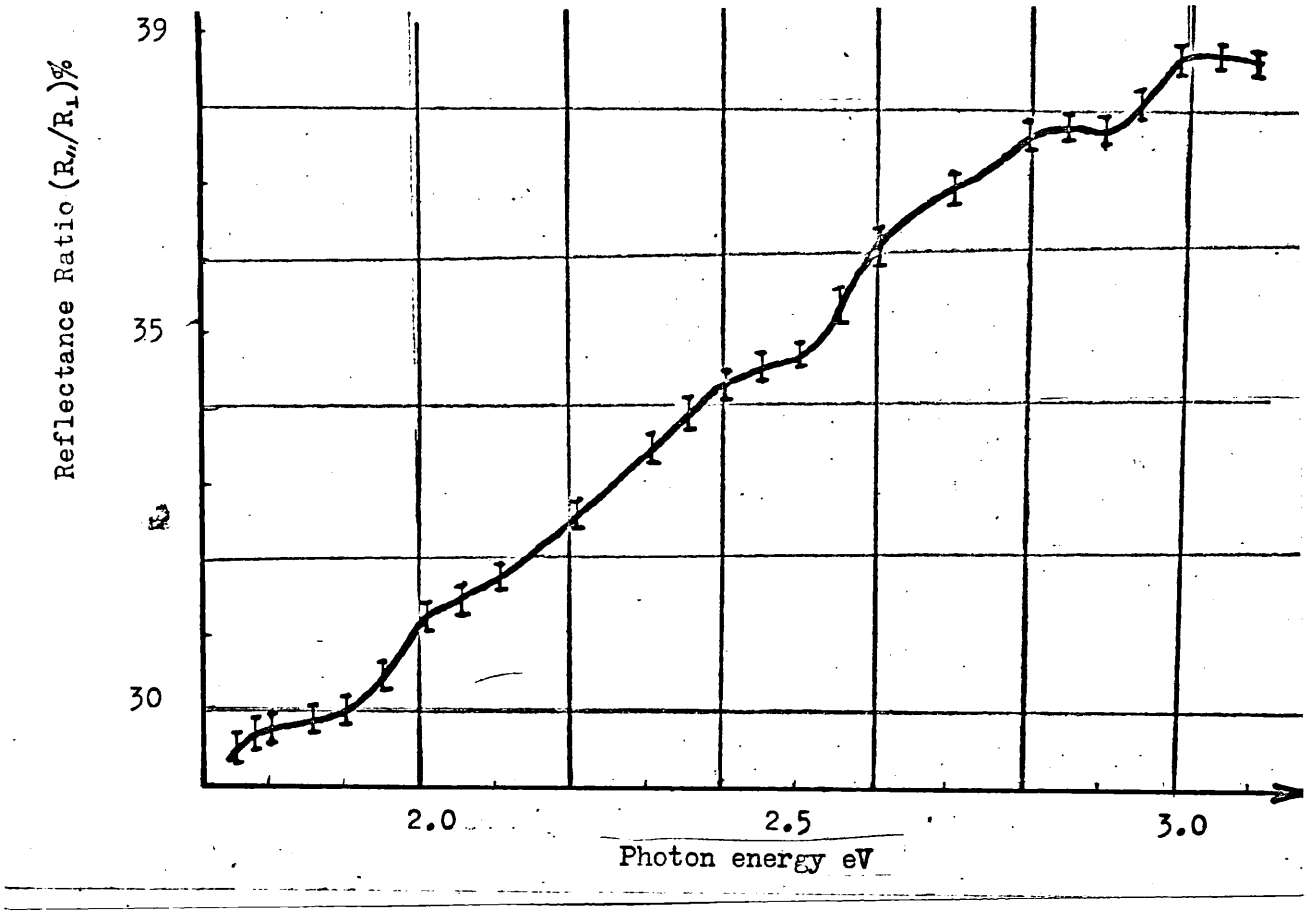

Figure 44. Reflectance ratio of terbium measured at an angle of incidence of 75.^{0}

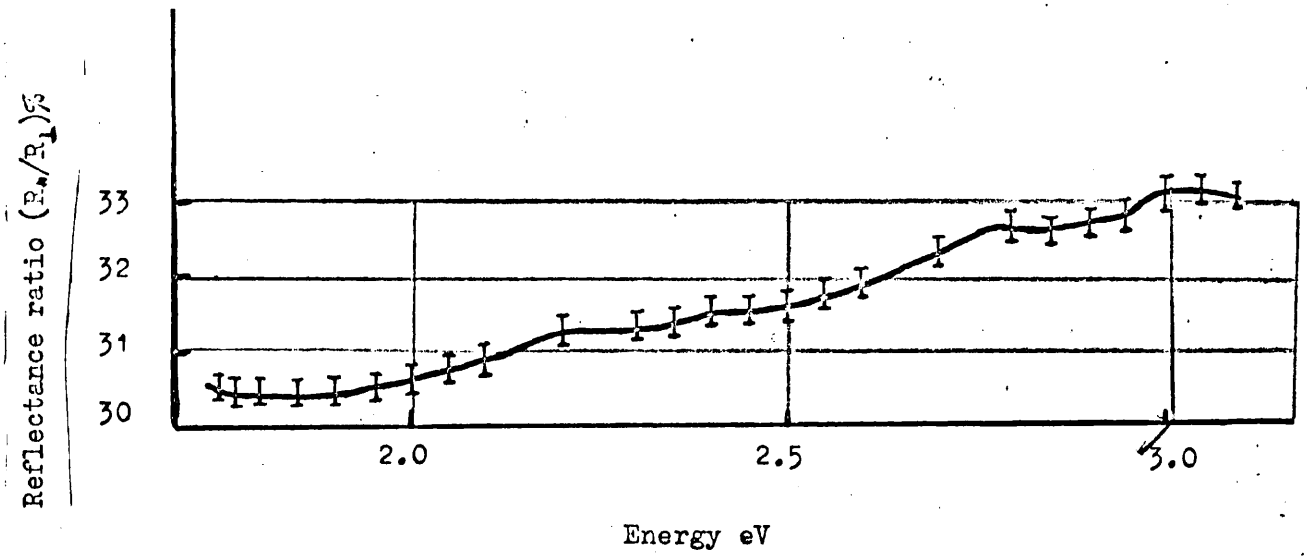

Figure 45. Reflectance ratio of terbium measured at an angle of incidence of 69°.

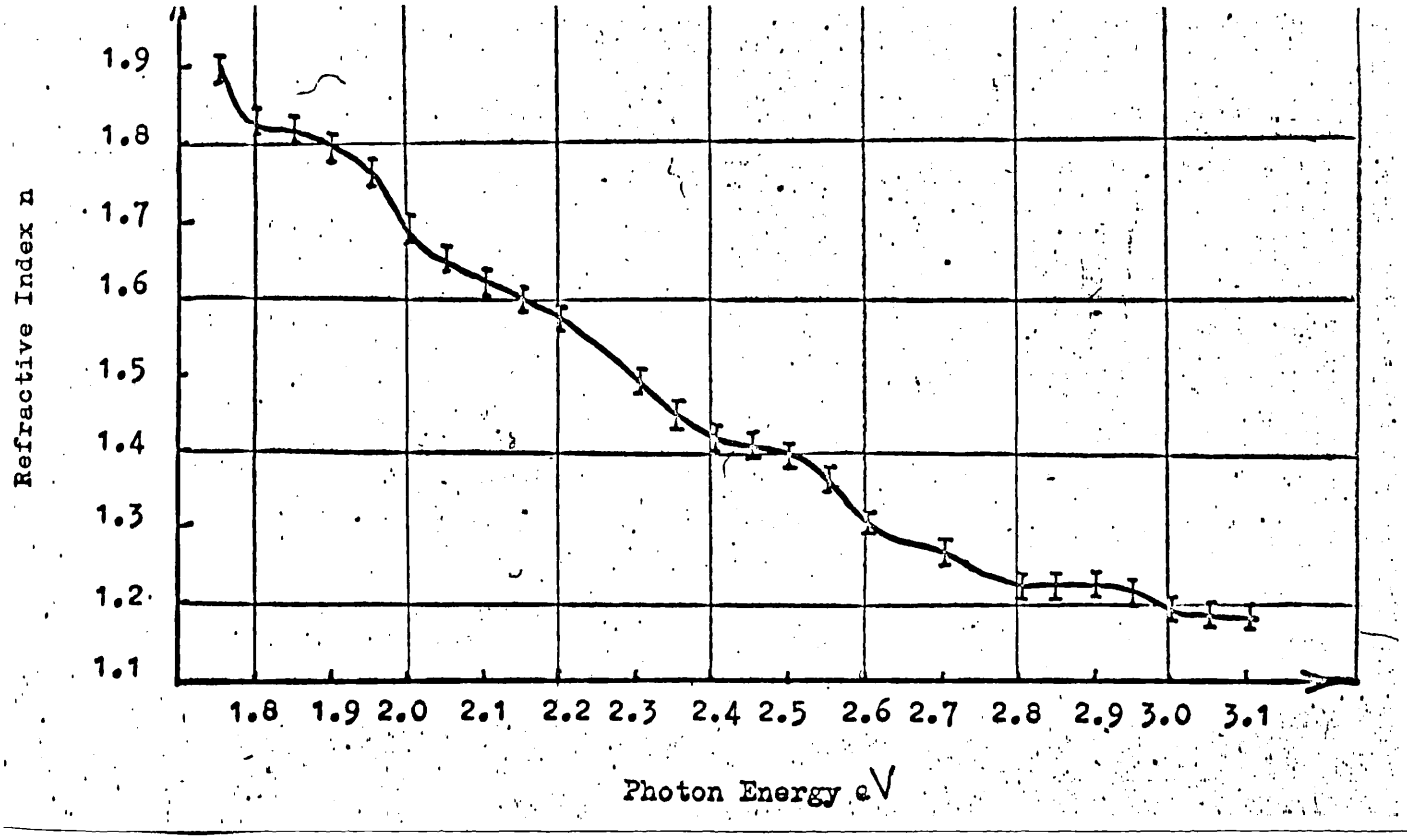

Figure 46. Refractive index of terbium.

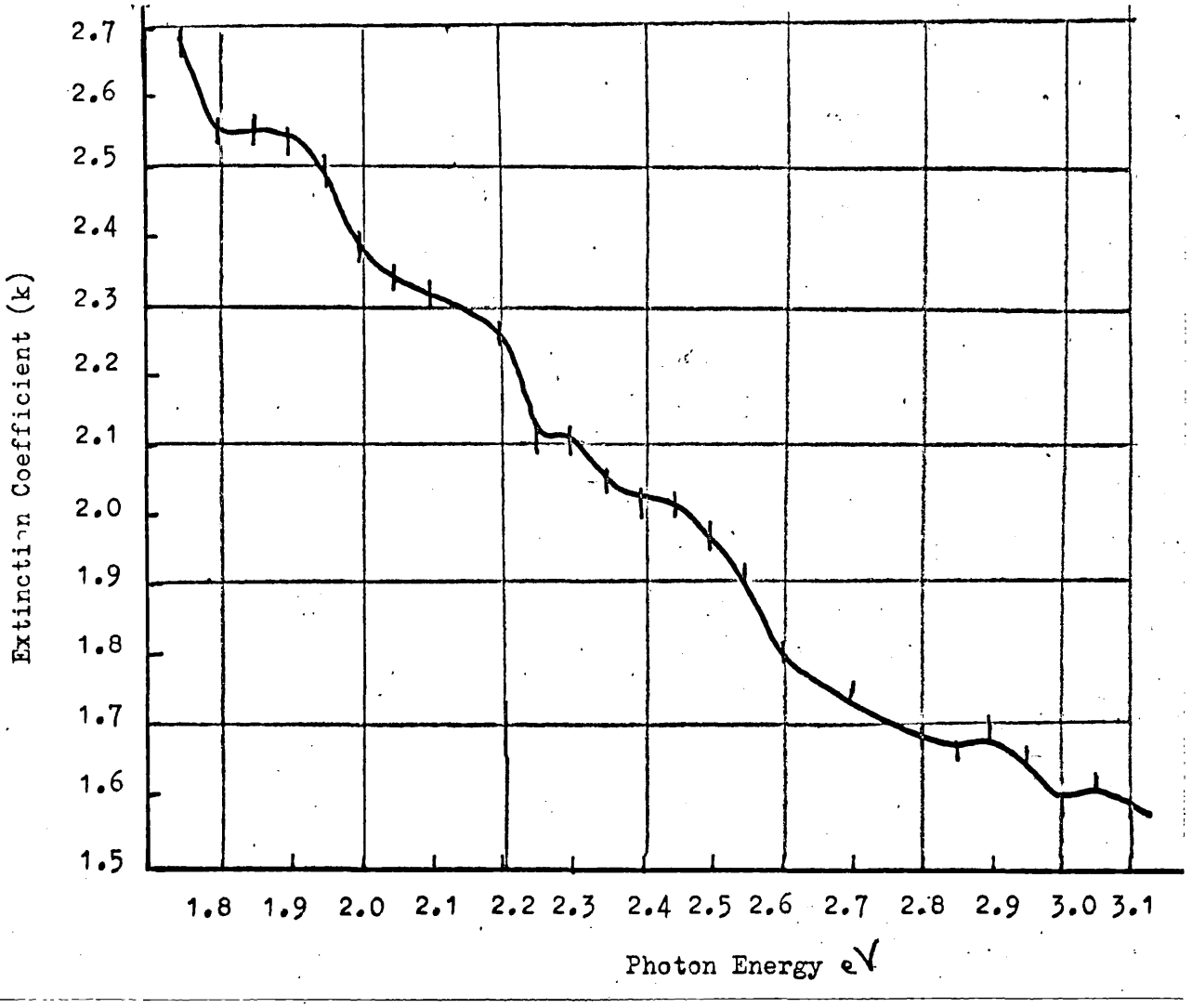

Figure 47. Extinction coefficient of terbium.

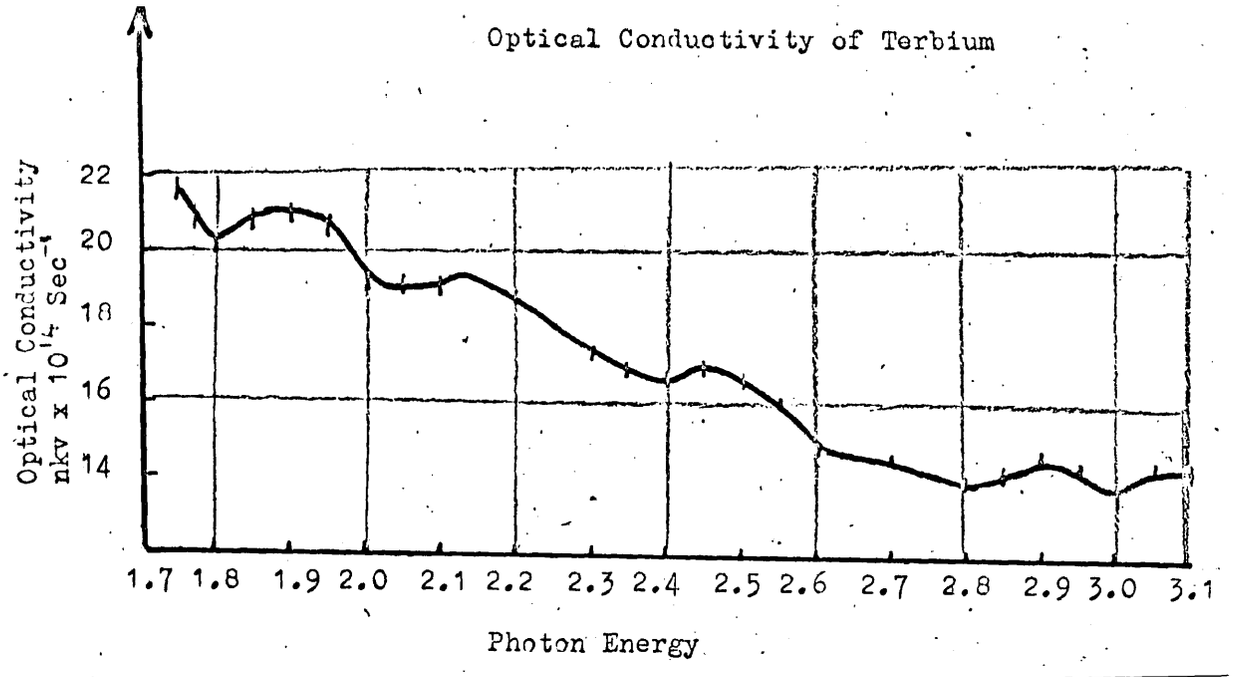

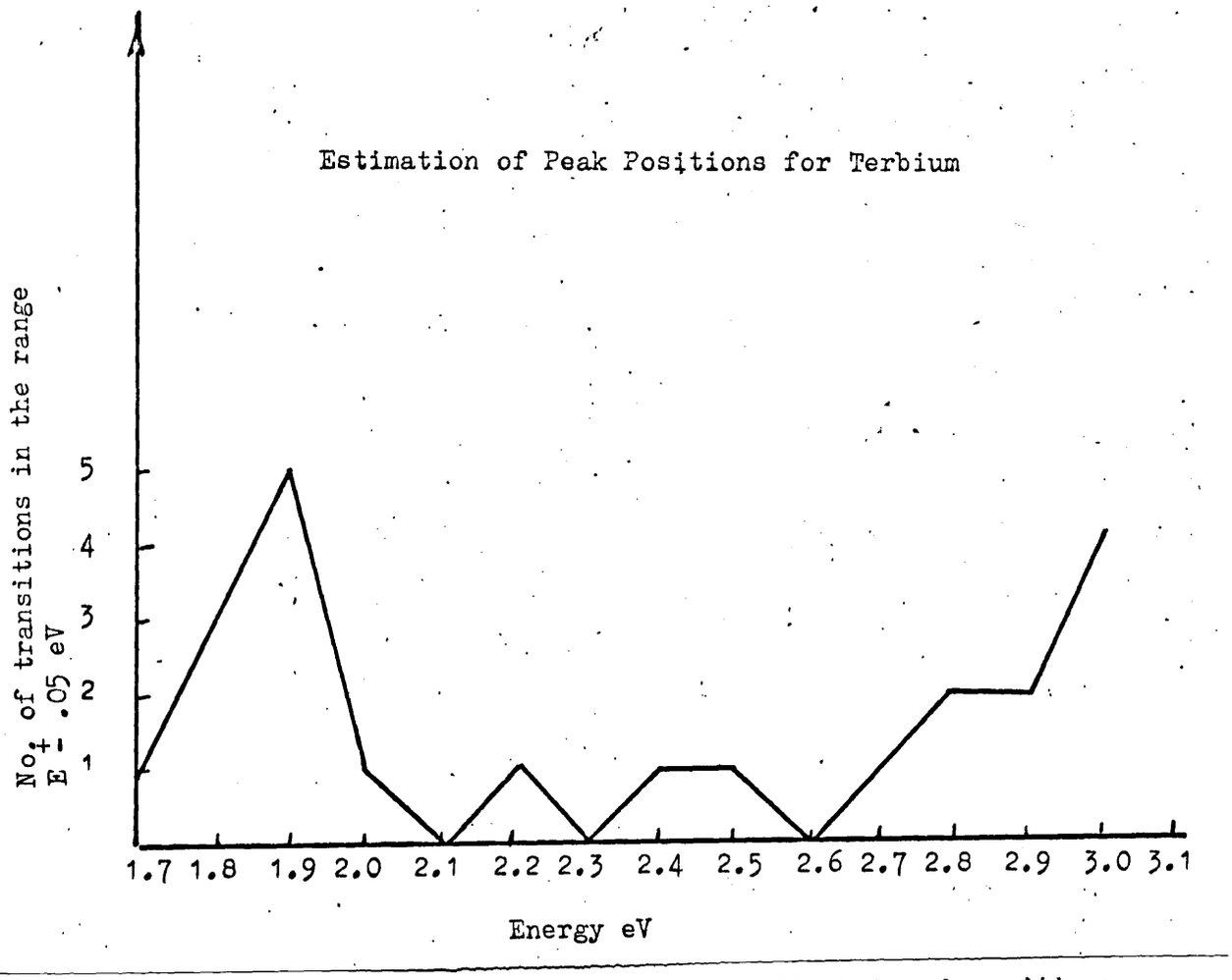

Figure 48. Optical conductivity of terbium and estimated peak positions.

tentatively at the energy 2.9 eV. There was, in most films measured, some evidence for structure in the range 2.7 - 2.9 eV. An X-ray analysis of the film was difficult owing to the small thickness of the specimen, but it could be reasonably concluded from the poor diffraction data that the structure was h.c.p. with the correct c/a ratio and poly- crystalline with some degree of fibre orientation.

6.16 Theoretical Interpretation of the Optical Conductivity Curve of Terbium.

Figure 49a shows the energy-bands of terbium calculated by Jackson (1969) who used a relativistic augmented-plane wave approach. The atomic configuration used to generate the starting potential was:-

Xe (1s-4d) $4f^{9}$ $5s^{2}$ $5p^{6}$ $5d^{(0)}$ $6s^{2}$

It has again been found that the calculated energy bands do not vary too much with starting potential (Keeton and Louks 1968). It will be noticed that the bands are not labelled as they are in Figure 40a. The reasons for this are associated with modern methods of band structure calculations. The symmetry properties of the eigenfunctions are usually determined by observation of the computer out-put, or alternatively labelling can be achieved from group theoretical considerations using observed degeneracies at symmetry inter-band points.

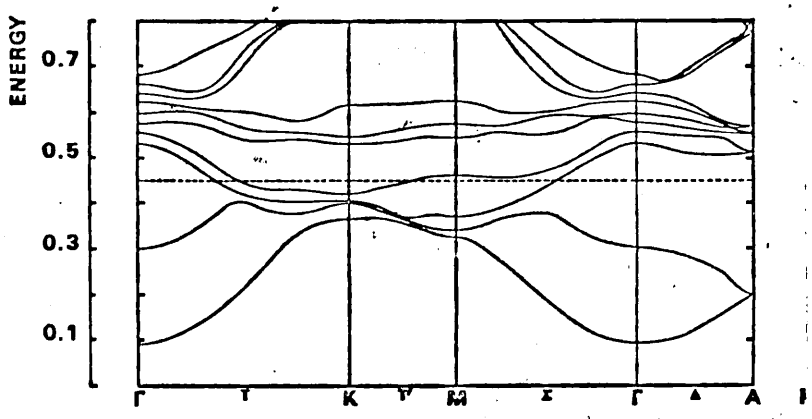

Figure 49(a)

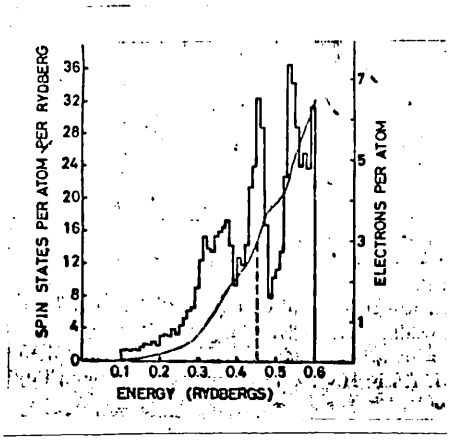

Figure 49(b)

In a relativistic calculation such as the one discussed here the degeneracies are removed by the presence of spin-orbit coupling, therefore this approach is untenable. In order to label the diagram it would therefore be necessary to use the original programme to determine the appropriate symmetries and this would be an extremely long procedure requiring considerable expertise in group theory. Obviously a few points could be labelled by direct comparison with the diagrams for gadolinium. However, we note that not many transitions in the range $1.8 \rightarrow 3.1$ eV are excluded for gadolinium by the selection rules given in Table (7). In the absence of labelling, we will disregard the selection rules and deduce figure 48b, corresponding to figure 40b for gadolinium. The energy differences between bands above and below the Fermi-level at symmetry interband points are listed below. These were taken from the out-put of Jackson's programme rather than a direct measurement from the diagram.

Symmetry Point	Energy Gap Δ E
M	1.836
	2.992
	2.788
	2.380
	2.788
K	2.230
	2.462
	1.754
	1.986
	2.924
	1.822
	1.918
	2.856
	1.714
	2.652

Symmetry Point	Energy Gap δE
A	No transitions within range of measurements.
L	1.938 (This level is assigned a strength 4 because both the upper and lower levels are doubly degenerate)
H	3.046 3.005 2.965
Γ	No transitions in this range.

The estimated peaks are shown in figure 48b. We see immediately that the estimated peak positions are similar to the estimated positions for gadolinium. Again the agreement between experiment and theory is good. In the theoretical diagrams the low energy peak for terbium is shifted to lower energies by 0.1 eV and this agrees well with the observed shifts in the experimental curves. The peak at 2.2 eV is due to a transition at the K symmetry point, as it was for gadolinium. The peak at 2.45 eV is due to a transition at the M symmetry point. From the theoretical diagram, we would expect the high energy peak to move to higher energies for terbium. This is indeed observed for the film measured here but in general, as stated, the structure near this energy is uncertain. Thus we have very good agreement between experiment and theory both for the individual curves and for the predicted shift in peak positions at the low energy end of the spectrum. Figure 50 shows an Argand plot of $n_k\gamma$ against

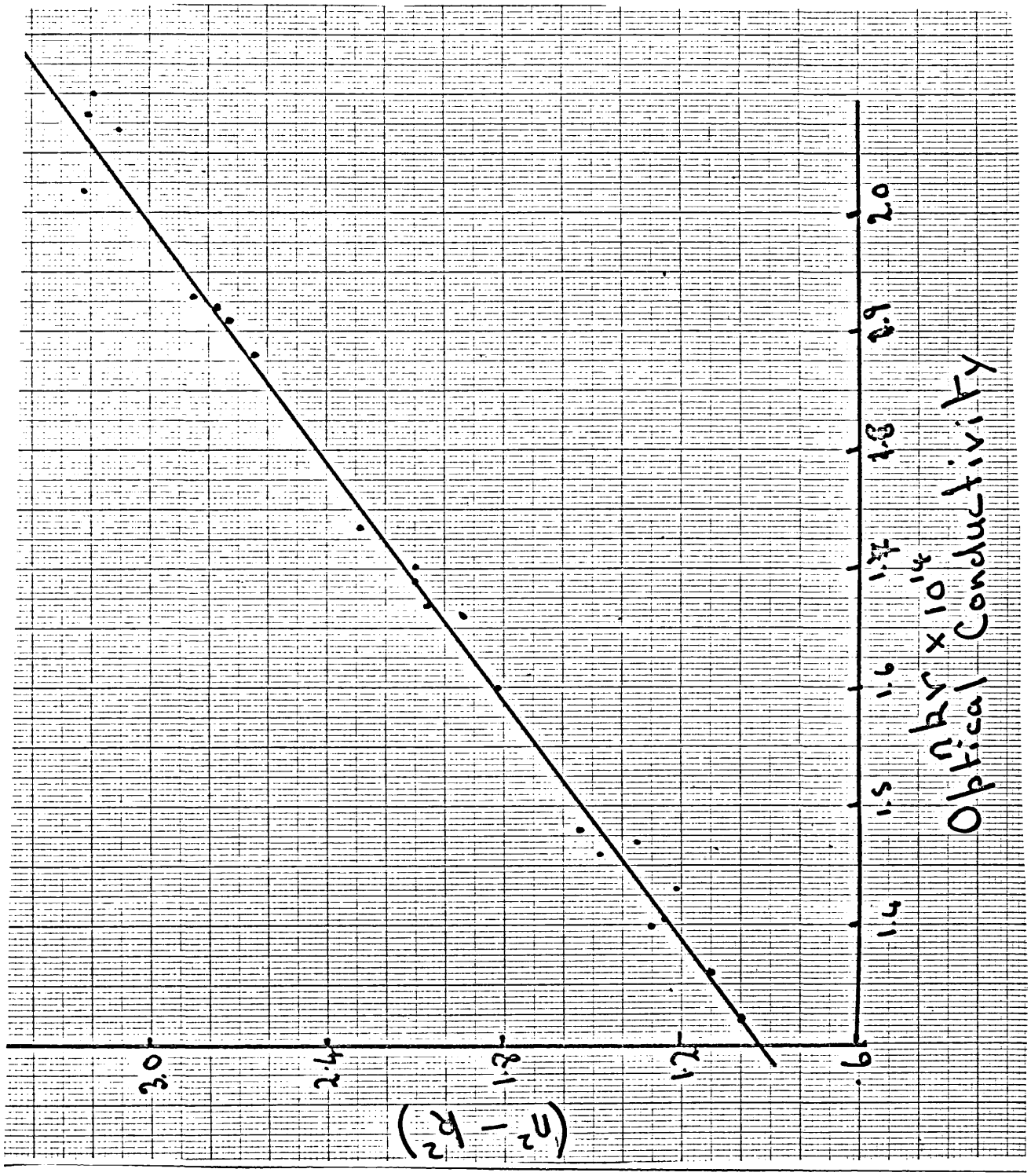
Optical Conductivity, σ_{xy}
$\times 10^{14}$ sec^{-1}
20
18
16
14
12
10
8
6
$(n^2 - k^2)$
3.0
2.4
1.8
1.2
0

Figure 50.

$(n^2 - k^2)$ and this is clearly a good straight line and the results might be interpretable in terms of an overall back-ground of free carrier absorption. However, one is reluctant to interpret the optical properties of the two metals differently. Figure 49b shows the density of states histogram for terbium. If the main peak position is estimated for terbium as it was for gadolinium we obtain 1.4 eV which is consistant with the slight decrease in slope on going from gadolinium to terbium. Because of the similarity between the two optical conductivity curves it is possible that the difference in the electronic configurations of the two elements is in the 4f level. This could be achieved in several ways, for example:-

$4f^8\ 5s^2\ 5p^6\ 5d^0\ 6s^2$ (Gadolinium)

$4f^9\ 5s^2\ 5p^6\ 5d^0\ 6s^2$ (Terbium)

or

$4f^7\ 5s^2\ 5p^6\ 5d^1\ 6s^2$ (Gadolinium)

$4f^8\ 5s^2\ 5p^6\ 5d^1\ 6s^2$ (Terbium)

6.17 Further Data on Terbium

It was again thought necessary to present further data on terbium to add credibility to the observed structure in the optical conductivity curves. Figure 51 shows additional optical conductivity curves. The general level of agreement between the curves is not as good as it was for gadolinium, however, this might be expected since terbium is known to be more chemically

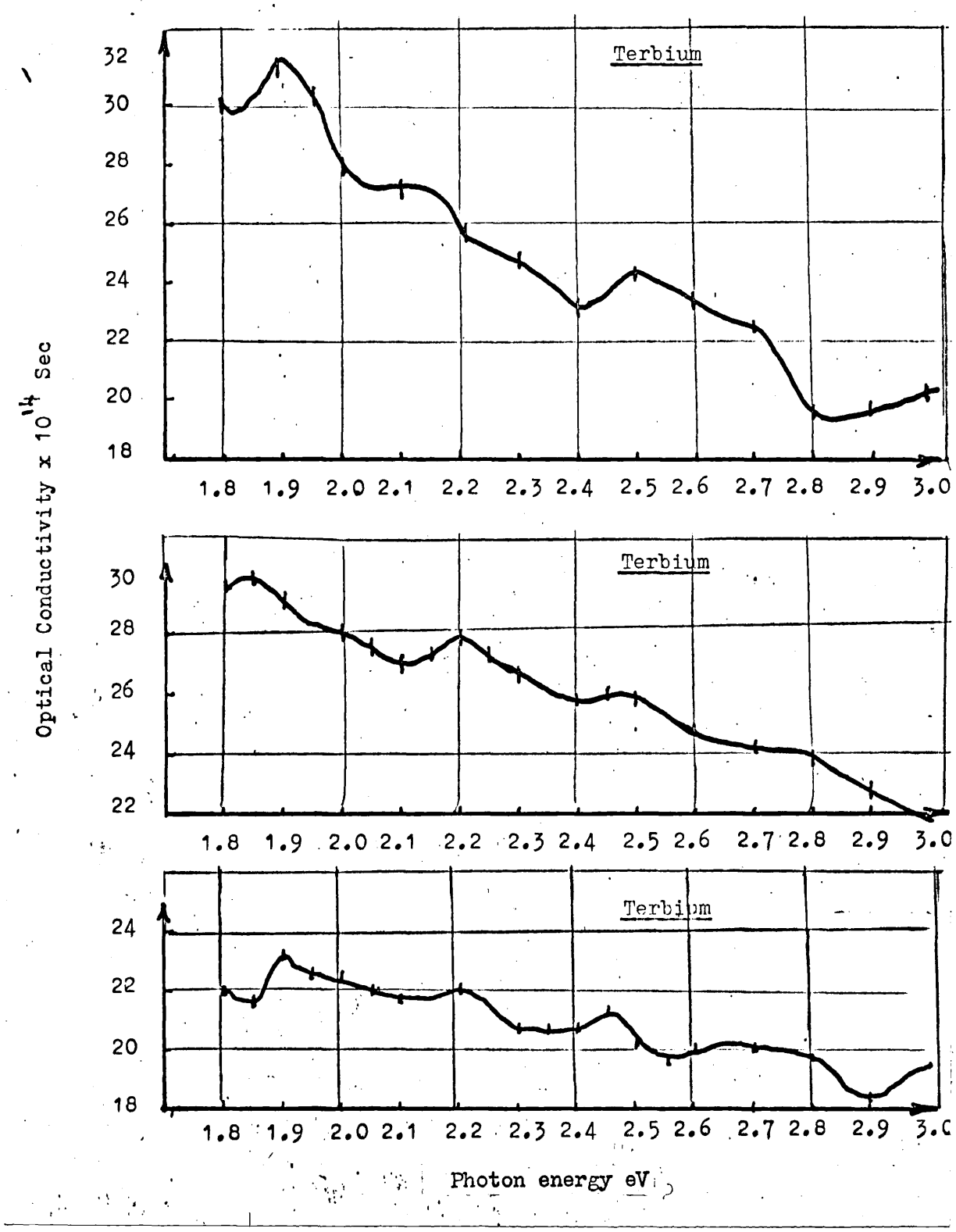

Figure 51. Additional data on terbium.

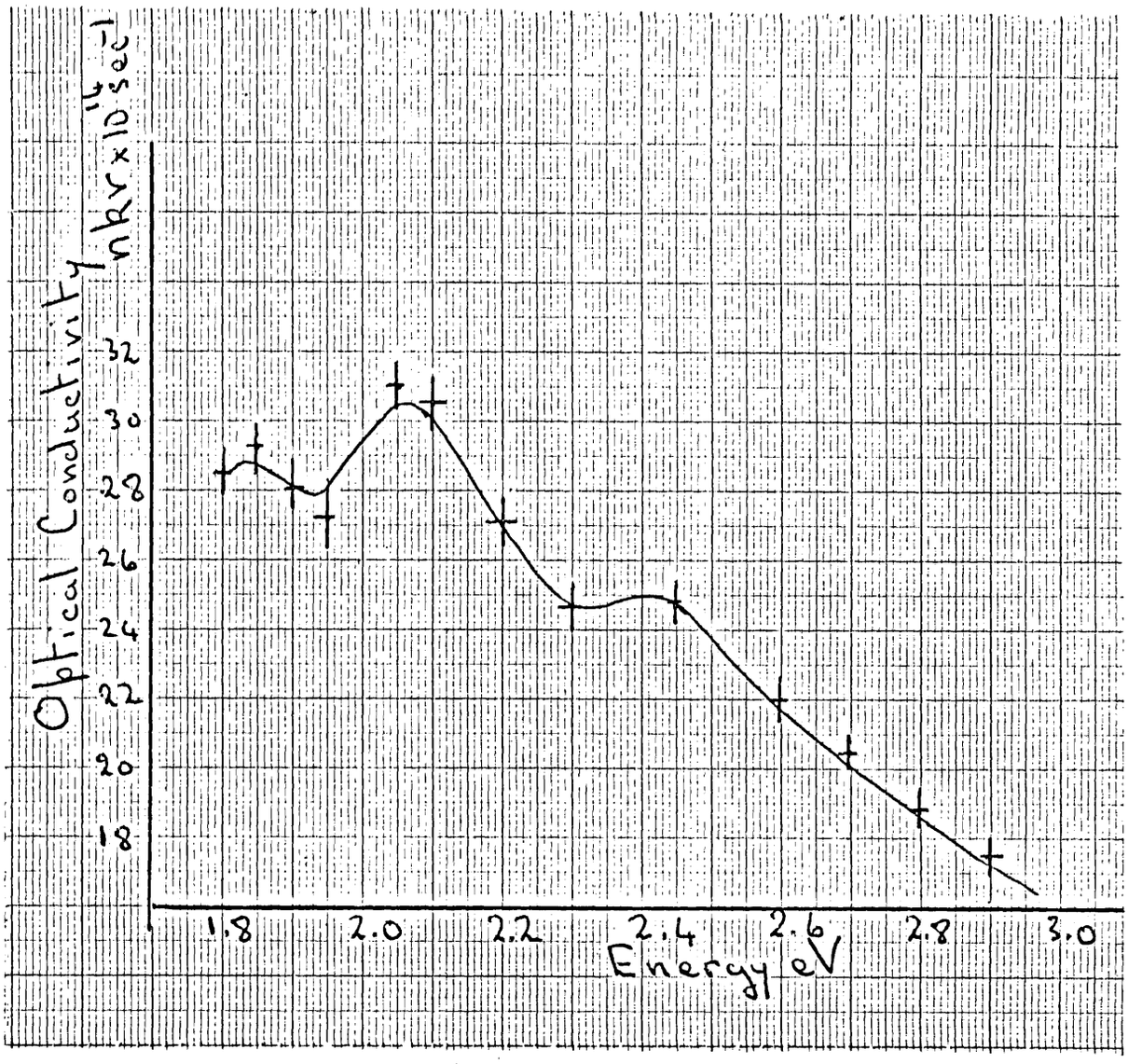

Fig 52

Optical conductivity of terbium measured in air by Hasan.

reactive than gadolinium. The curves shown here are consistant with the conductivity curve discussed in (6.15) with the exception of the behaviour above 2.8 eV. Clearly the assignment of a peak at high energies is tentative. The poor reproducibility at the blue end of the spectrum is not well understood. Tentatively, it can be suggested that there is a strong peak just above 3.0 eV and that this peak is structure dependant, this would account for differences in observed slope between different films. Petrakian and Schuler both claim to have observed strong structure just above 3.0 eV. Figure 52 shows the optical conductivity of terbium films measured by Hasan (Unpublished) in air and these results confirm the existance of structure in the optical conductivity curve.

6.18 Summary on the Rare Earth Data

The optical properties of terbium and gadolinium have been measured on carefully prepared surfaces. The conductivity curves show structure not previously observed and this structure can be interpreted quite well in terms of interband transitions at symmetry inter-band points. The overall background to the curve may be interpreted in terms of non-k-conserving transition from the Fermi-level.

CHAPTER VII

7.1 Introduction

In this chapter an optical study of copper and gold is described. In view of the importance of the results of the previous chapter it was felt that a general check of the apparatus should be made using specimens for which well established data was available for comparison purposes. Recent work by Pells and Shiga (1969) was carried out on samples prepared by heat treatment in U.H.V. and it was of interest to compare results on surfaces prepared by different methods. Copper is, perhaps, the best understood of all the metals. Mueller and Phillips (1967) have carried out a calculation of the imaginary part of the dielectric constant (2nk) based on band structure calculations carried out by Burdick (1963). This is, to date, one of the few calculations of its kind and therefore provides a rare opportunity for comparisons to be made between experiment and a comprehensive theoretical calculation. However, the prime objective of the study was to provide a control for the studies made on the rare earths. This study was, therefore, less comprehensive, only two films of each metal being measured.

7.2 The Preparation of Copper Films

Copper was evaporated from oxygen free material estimated to be 99.99% pure (supplied by the Johnson-Matthey Company).

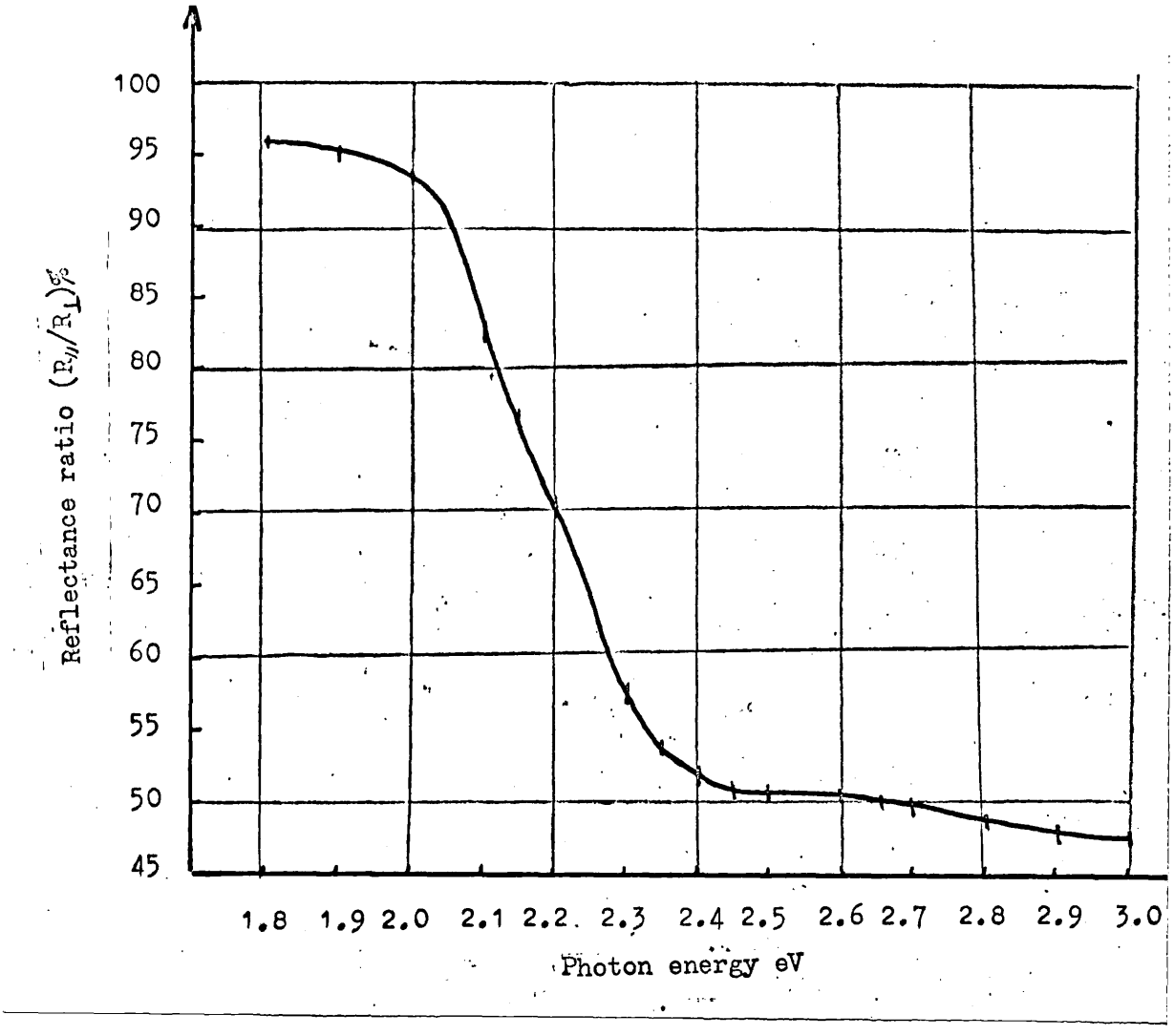

Figure 53. Reflectance ratio of copper measured at an angle of incidence of 75°.

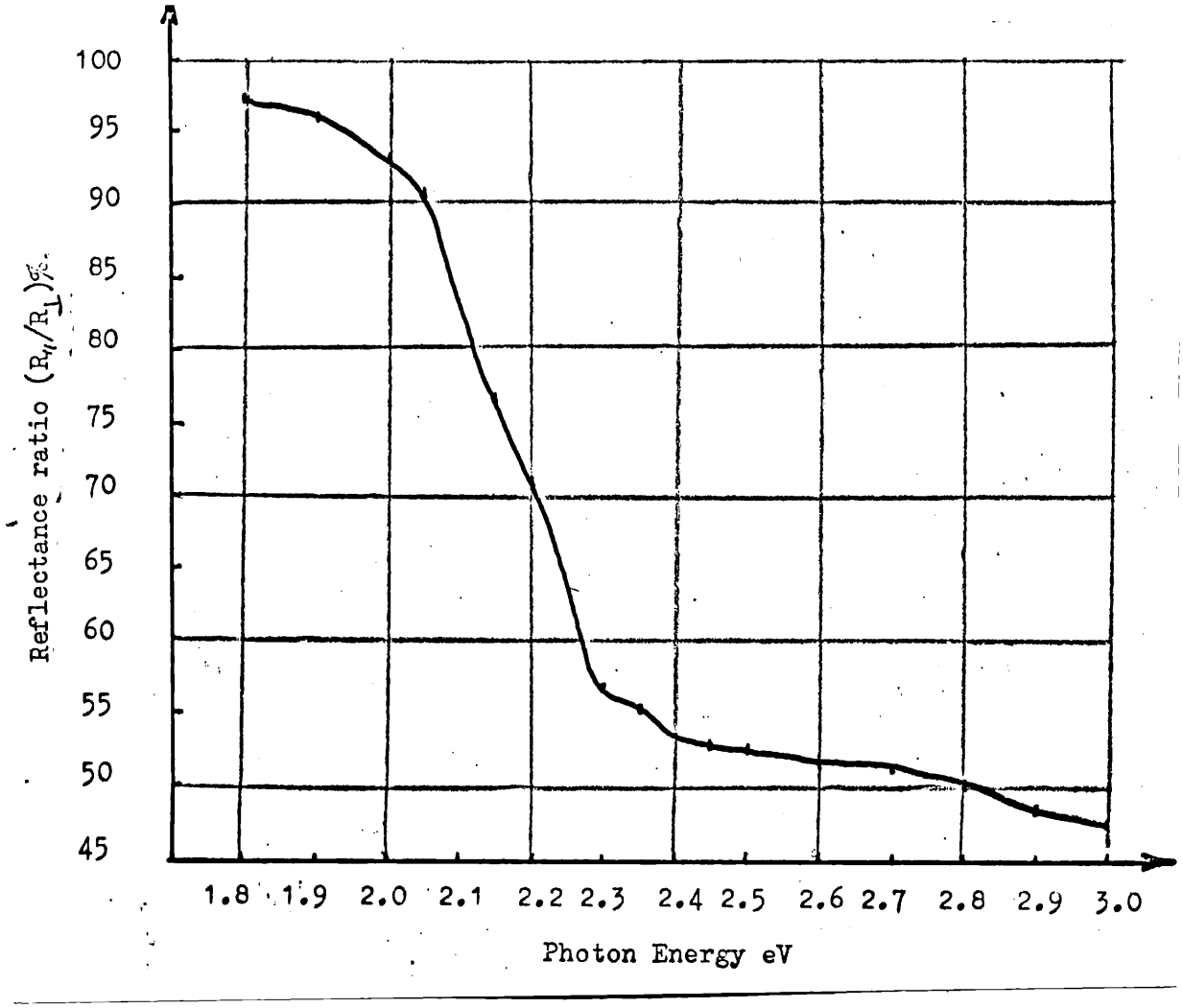

Figure 54. Reflectance ratio of copper measured at an angle of incidence of 68°.

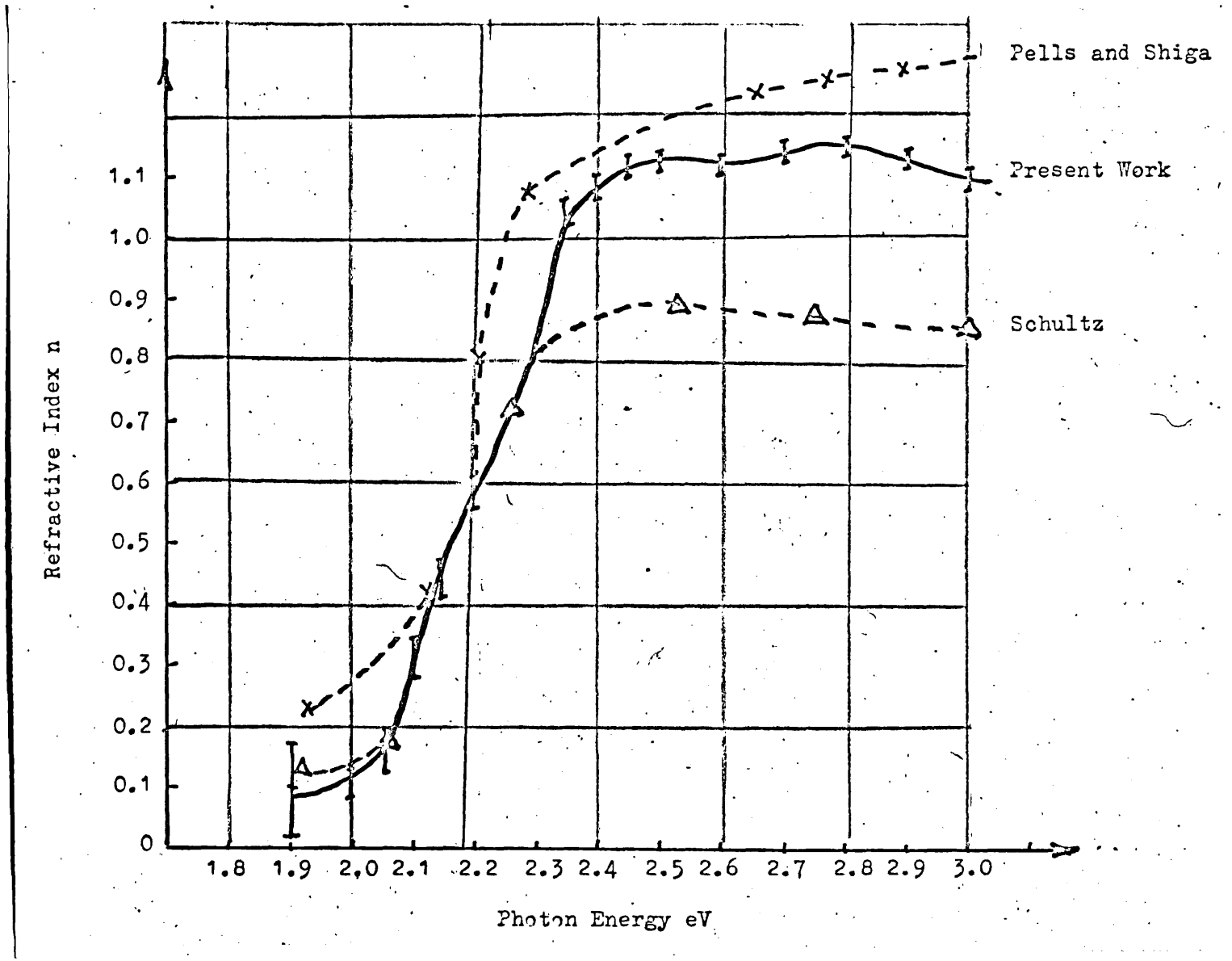

Figure 55. Refractive index of copper.

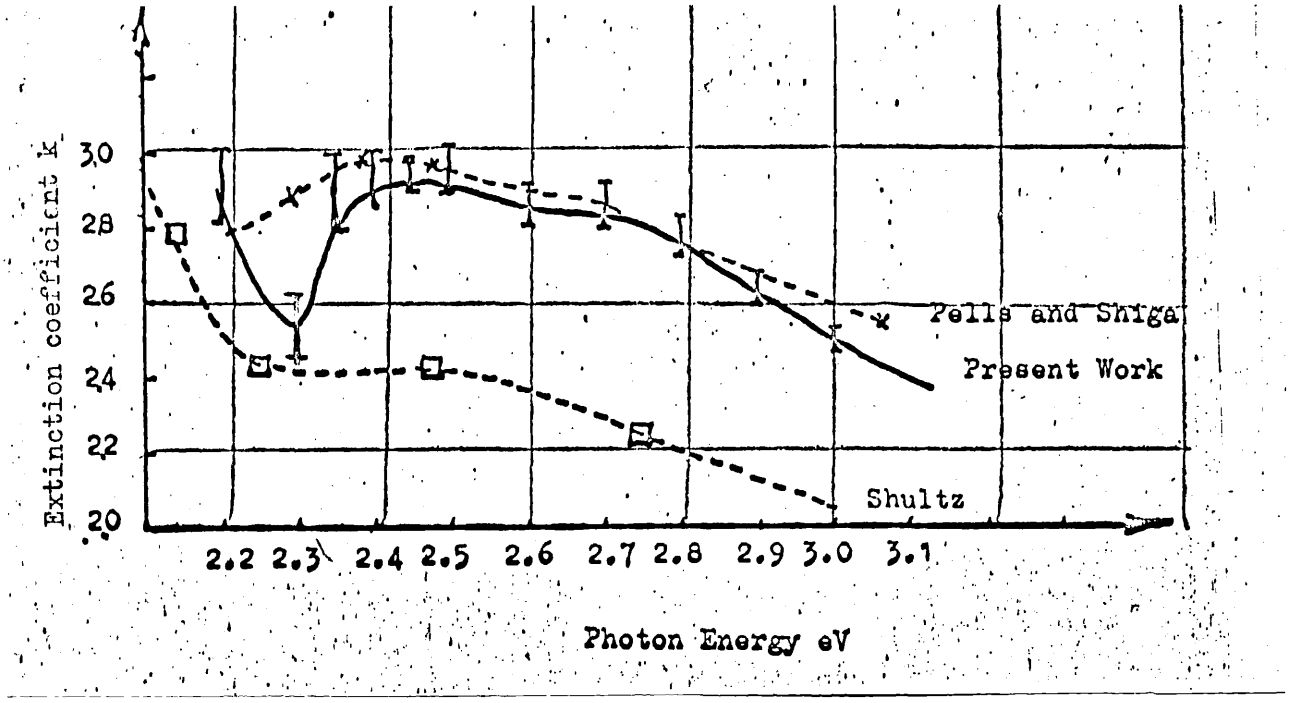

Figure 56. Extinction coefficient of copper.

The metal was again evaporated from a tungsten helix. The base pressure used for both films was $\sim 10^{-10}$ Torr. The predominant peak in the mass spectrum was at mass number 28 (CO) with additional peaks at mass number 18 (H_2O) and 44 (CO_2). For the film discussed here a current of 50 Amps was passed for one minute giving a thick copper film $\sim$1400Å. During the evaporation the pressure of the system remained at $< 5 \times 10^{-9}$ Torr. Measurements were completed within four hours of growth.

7.3 Reflectance Ratio Measurements of Copper

Reflectance ratios of the sample were measured at angles of incidence of 76° and 68° using the system described previously. Again the accuracy of the measurement was assessed at $\sim 0.3\%$. The measured reflectance ratios are shown in figures 53 and 54. Clearly there is an absorption edge at about 2.15 eV as might be expected from the red colour of copper.

7.4. The Optical Constants of Copper

The values of n and k derived from the reflectance ratios are shown in figures 55 and 56. The results for n are shown from 1.9 eV and those for k above 2.1 eV. This is because it was found that below the absorption edge n was very small and k relatively large leading to excessively high errors in the determined optical constants. For example at 1.8 eV the programme returned:

$n = 0.09 \pm 0.963$

$k = 4.58 \pm 14.00$

Thus we have encountered a region of very poor sensitivity and for this reason some results have been discarded. Those results presented here do, however, have acceptable accuracy. In addition, the results of Pells and Shiga are shown together with those of Schultz (1954). The determinations made by Pells and Shiga were ellipsometrical using apparatus described by Pells (1967). Schultz's determinations were based on interferometrical techniques and were made on samples prepared by thermal evaporation and measured in air.. The agreement between the present work and that of Pells and Shiga is encouraging, particularly when we consider the poor agreement often obtained by other workers. When considering the data available on germanium Heavens (1959) was moved to state, "On the whole there is depressingly little correspondence between different observers results". If we consider the values of extinction coefficients k we note one marked discrepancy between the present work and that of Pells and Shiga. Within the limits of the experimental uncertainty of this work there is a minimum present at 2.30 eV. It is not possible to assess the behaviour of Schultz's curve in this region, however, his limited data does not exclude the possibility of a minimum. This minimum in the extinction coefficient has important consequences when the optical conductivity curve is discussed. At this stage we note that the main objective of this

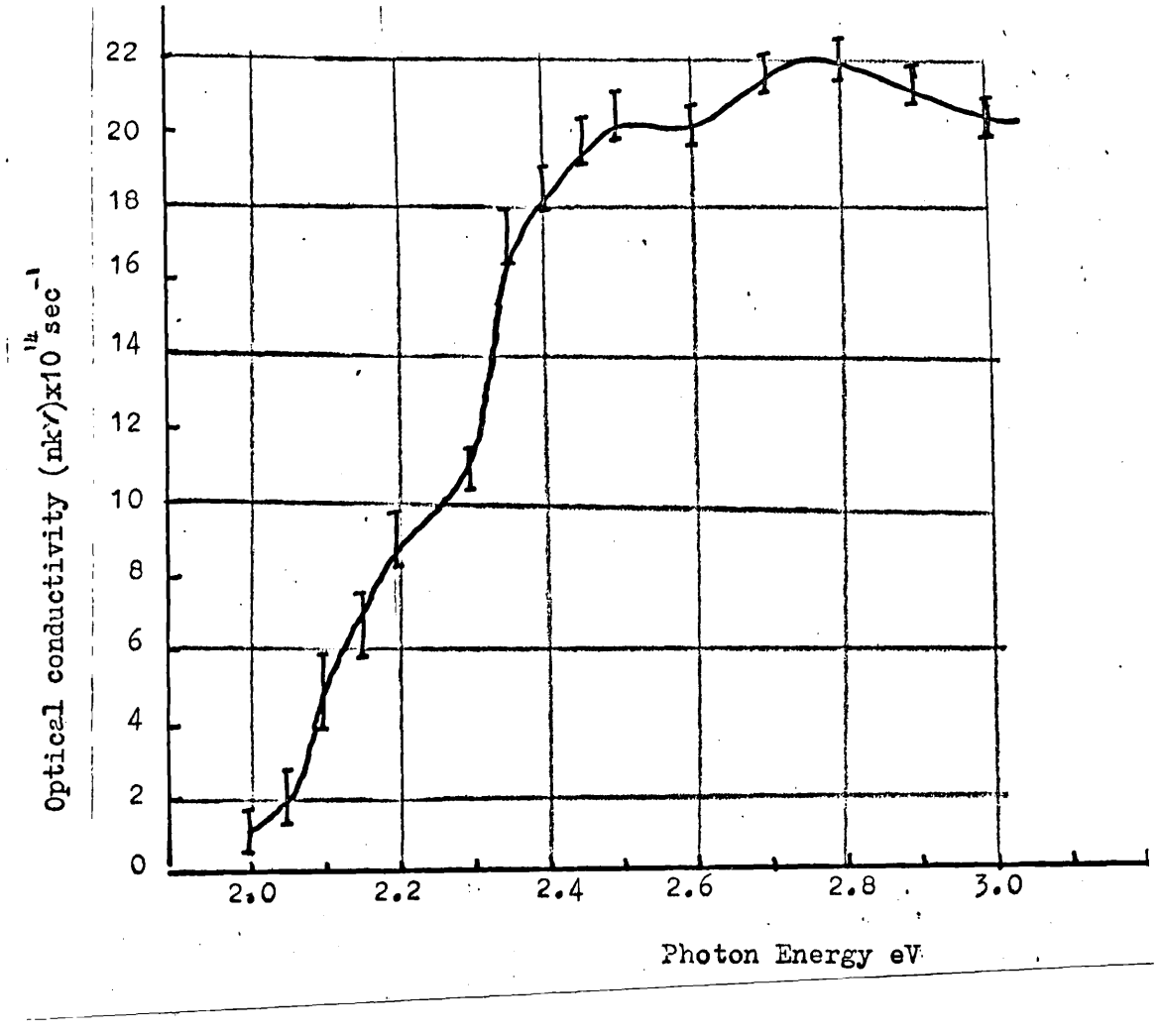

Figure 57. Optical conductivity of copper grown at high evaporation rate.

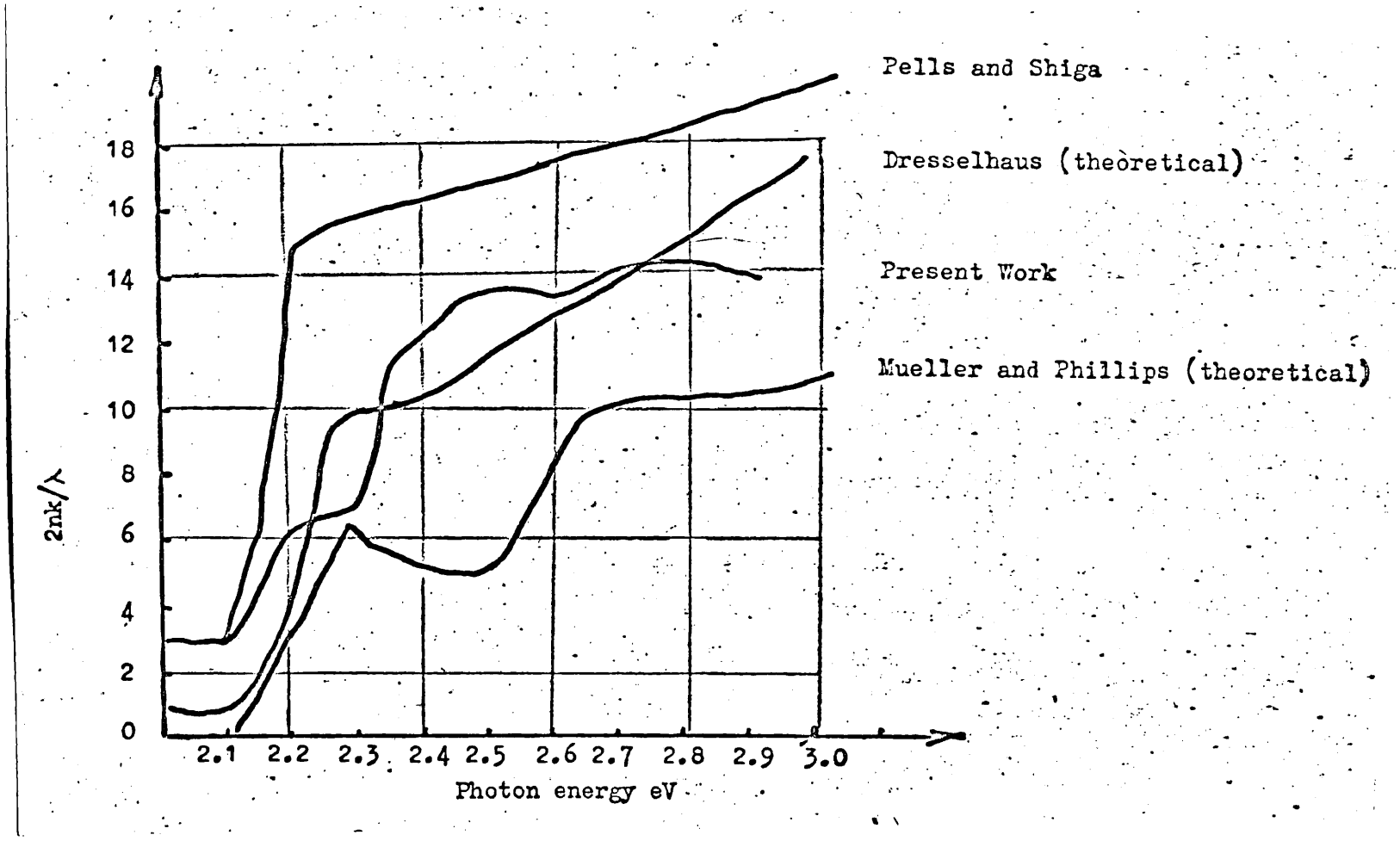

Figure 58. Absorption coefficient of copper.

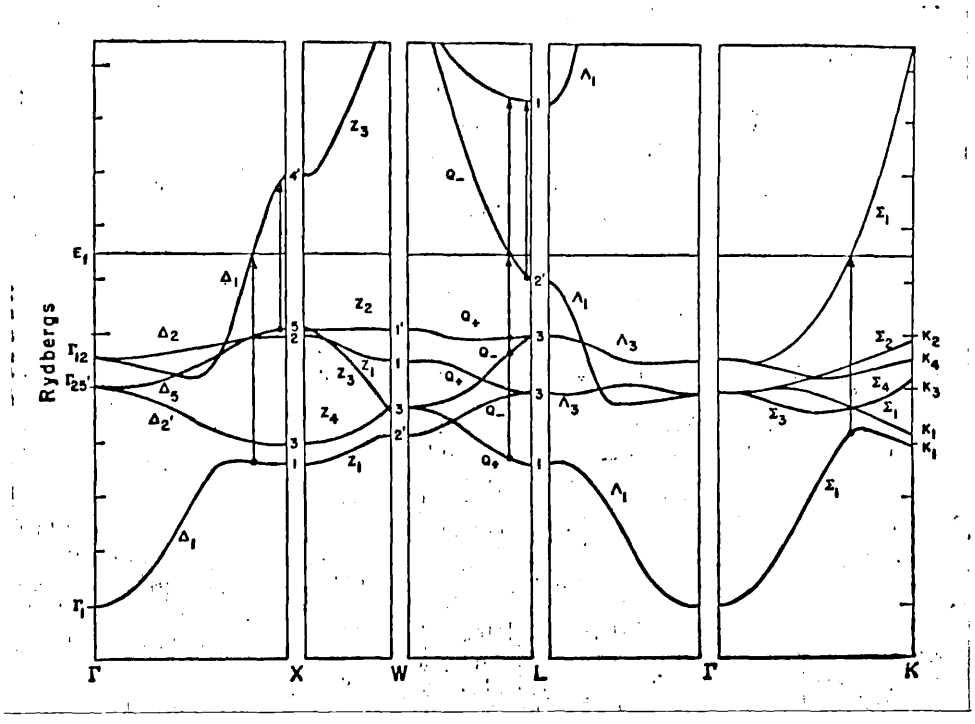

Figure 59. Energy bands of copper.

study has been achieved. A tolerable agreement has been obtained between results taken with the apparatus used for the rare earth measurements and the results of a different observer, using different surface preparations and a different measuring technique.

7.5 The Optical Conductivity Curve of Copper

The optical conductivity of copper is shown in figure (57). The absorption edge is seen to start near 2.05 eV and is centred at 2.2 eV. Between 2.3 and 2.4 eV there is a sharp increase in slope indicating possible structure near 2.25 eV. There is also possible structure near 2.40 eV and 2.80 eV. Figure (58) shows the quantity $2nk/\lambda$ (absorption coefficient) plotted as a function of photon energy together with the results of Pells and Shiga. The positions of the absorption edges are in good agreement, as are the general magnitudes of the results. The detailed behaviour above the edge and the behaviour near 2.3 eV is different.

7.6. Theoretical Interpretation of the Results for Copper

Figure (59) shows the appropriately labelled energy band structure diagram for copper obtained by Burdick (1963) Mueller and Phillips have used the results of the calculation to obtain the quantity 2nk by evaluating the following summation.

$$\epsilon_2(\omega) = \frac{4\pi e^2 \hbar^2}{3 m^2 \omega^2} \sum_{m,n} \int_{B.Z} \frac{2}{(2\pi)^3} d\vec{k} |P_{mn}|^2 \delta(E_n - E_m + \hbar\omega) \quad (1)$$

where K represents a vector in the reciprocal lattice and

$$P_{mn} = \frac{\hbar}{\Omega i} \int \psi^*_{km} \nabla \psi_{kn} \cdot d\gamma$$

Ω = is the volume of the unit cell.

The form of (1) is plausible since it represents a double sum over all reciprocal space of all wave functions giving eigenvalues ~~being~~ having equal energy differences $\hbar\omega$. The actual computation of this integral is non-trivial and the results are shown in figure 58. We note in passing that this is the type of calculation which could be performed for the rare earth metals, being more comprehensive than that given in the previous chapter. The results of a similar calculation by Dresselhaus (1969) are also shown in figure 58. A feature of both of these theoretical curves is the structure near 2.2 eV and, in the case of Mueller's curve, below the top of the main absorption edge. This agrees very well with the structure observed experimentally in this work. Thus according to Mueller's work, we can assign the transition to $\Delta_5 \longrightarrow \Delta_1(E_f)$ in Figure 59. Mueller's work also shows a marked levelling off of the curve above 2.6 eV which could well be associated with the experimentally observed peak at 2.8 eV. However, both the experimental and theoretical curves of other workers are rising at 3.0 eV whereas that obtained here is decreasing slowly. In common with those of Pells, the results here indicate that the energy absorption edge starts at a slightly lower energy than is predicted by theory. Thus on the basis of the results obtained for one of

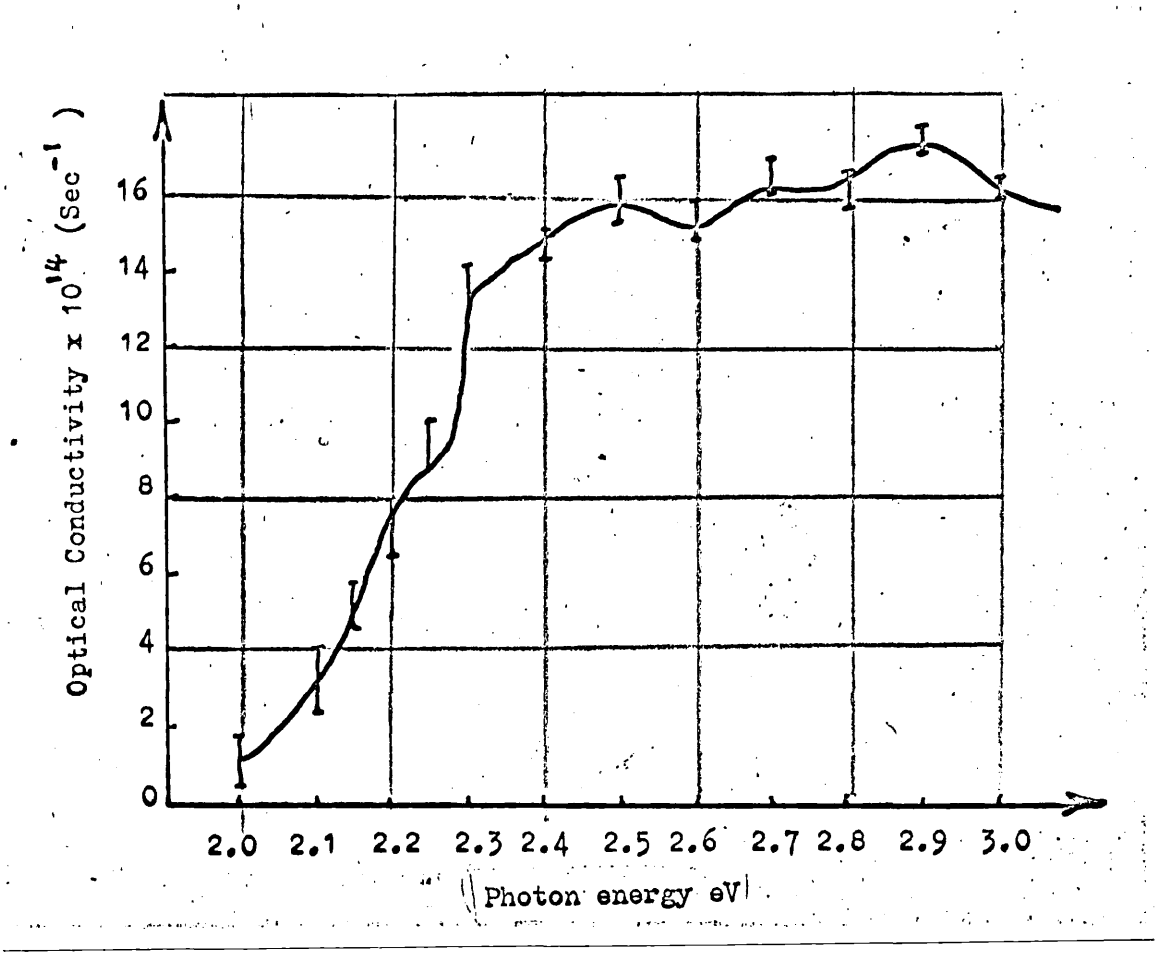

Figure 60. Optical conductivity of copper grown at low evaporation rate.

the copper films we might conclude that we have achieved somewhat better agreement with theory than previous workers.

7.7. Further Results on Copper

Figure 60 shows the optical conductivity of a copper film grown under slightly different conditions. Although the base pressure of the vacuum system and the residual gas analysis were almost identical to those discussed for the previous film, a different evaporation rate was used. A current of 42 Amps was passed for two minutes to give a film $\sim$ 1400Å. The difference in evaporation rates arose because it was not possible to evaporate the copper at the lower current for the first film discussed. Presumably the differences in current required to evaporate the copper in the two cases was caused by different loading conditions for the filament. We note that the level of the top of the absorption edge is reduced. The structure near 2.3 eV is neither confirmed nor excluded by this set of results. In particular the values of the extinction coefficient are considerably reduced and are nearer to those obtained by Schultz. The values of n were also smaller and are shifted towards those obtained by Schultz. Because it is considered that the results of Pells and Shiga in vacuum, are superior to those of Schultz, it is thought that the first set of results presented here are probably nearer ideal than the second set. In the absence of further data it is only possible to draw the following conclusions very tentatively.

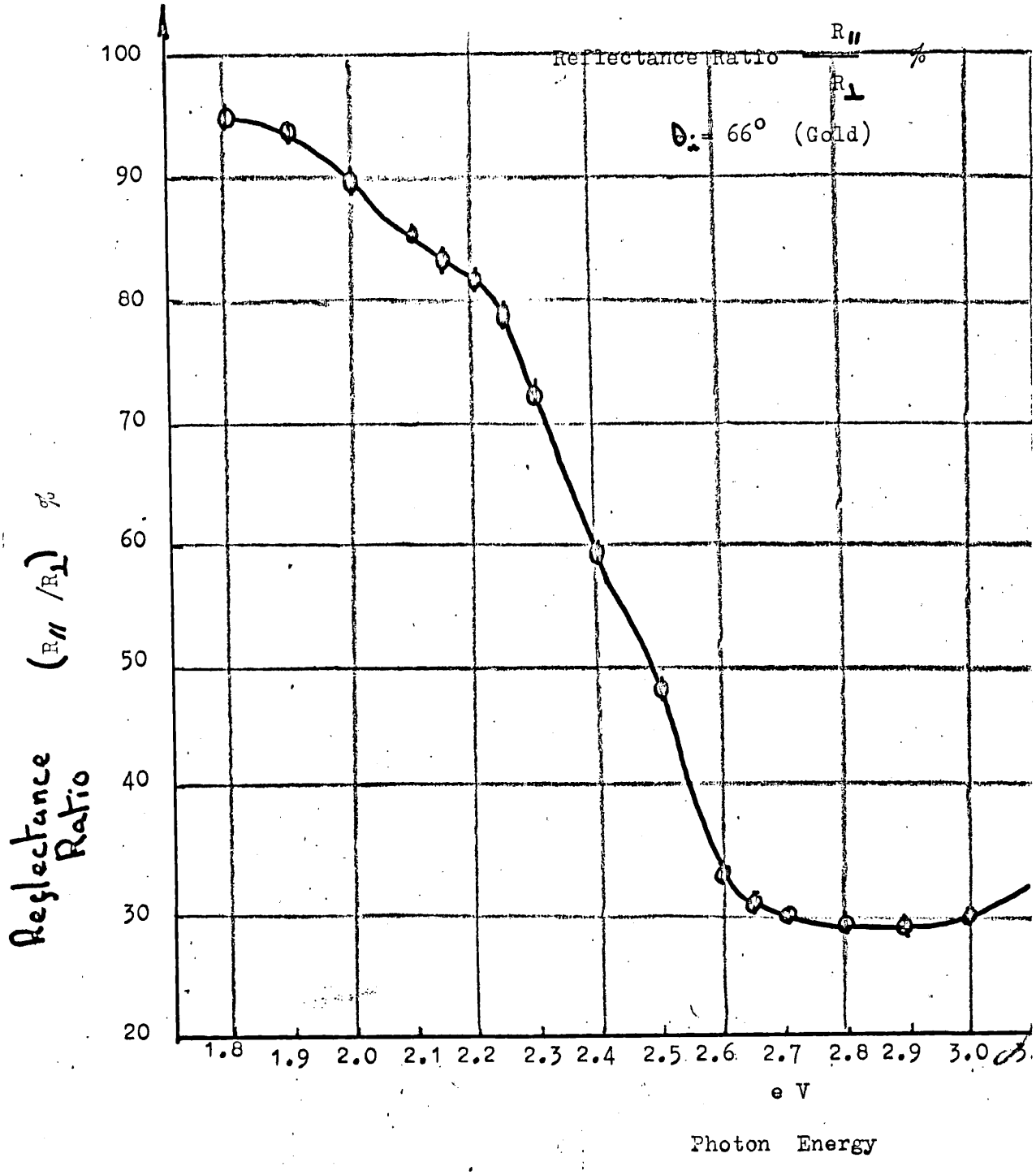

Figure 61. Reflectance ratio of gold.
$\theta_i = 66°$

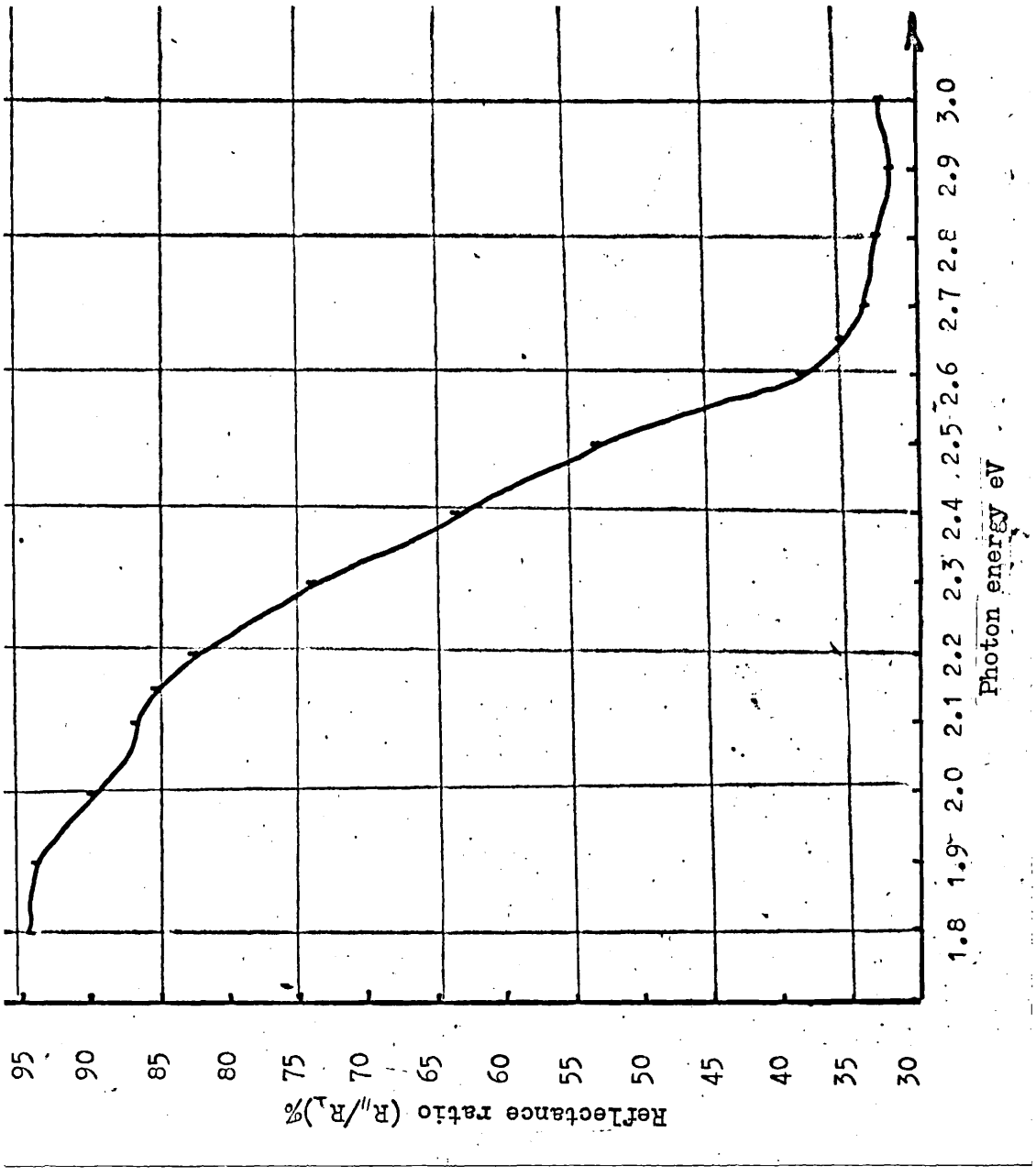

Figure 62. Reflectance ratio of gold.

$\theta_i = 75°$

However, they do represent an encouraging basis for further work.

i) The optical constants of copper measured using the reflection ratio method described previously, and on surfaces prepared by thermal evaporation in ultra-high vacuum, are in reasonable numerical agreement with those measured by different techniques on surfaces prepared by different methods.

ii) There is some possibility that structure has been detected in the optical conductivity curve of copper that has not been previously observed.

iii) From the observations, it would seem that high evaporation rates are necessary in order to produce films having optical constants close to those of films prepared by different techniques.

iv) For copper, it would seem that the differences in the general level of observed optical constants between different workers is probably due to different surface conditions rather than measuring techniques.

7.8. Optical Properties of Gold

Two films of gold were measured using the reflectance ratio method. For both evaporations the base pressure of the system was $< 3 \times 10^{-10}$ Torr and the residual gas composition was similar to that discussed in 7.2. Different evaporation rates were used for each film. Data are presented for one film and comparisons with the second film made at a later stage. Figures 61 and 62 show

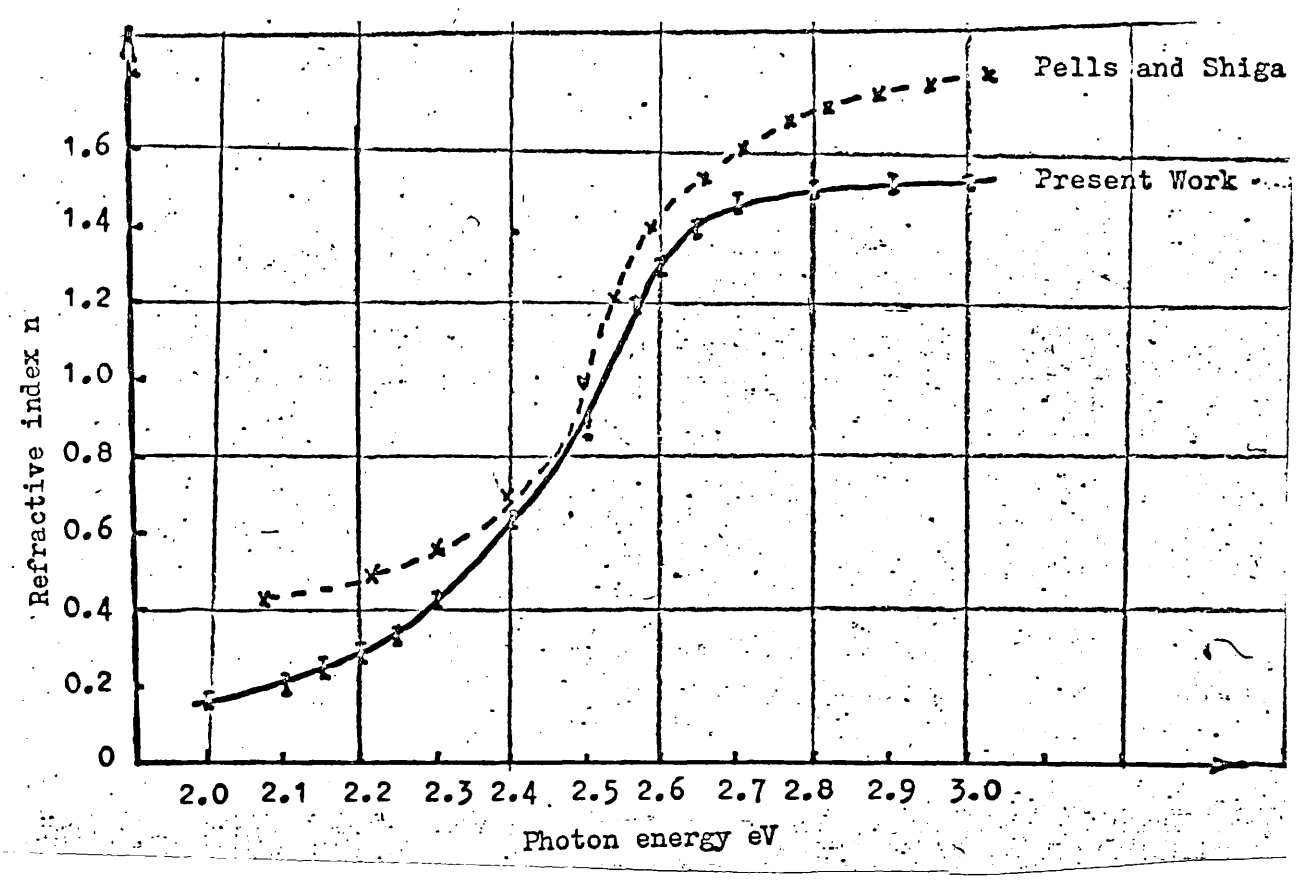

Figure 63. Refractive index of gold.

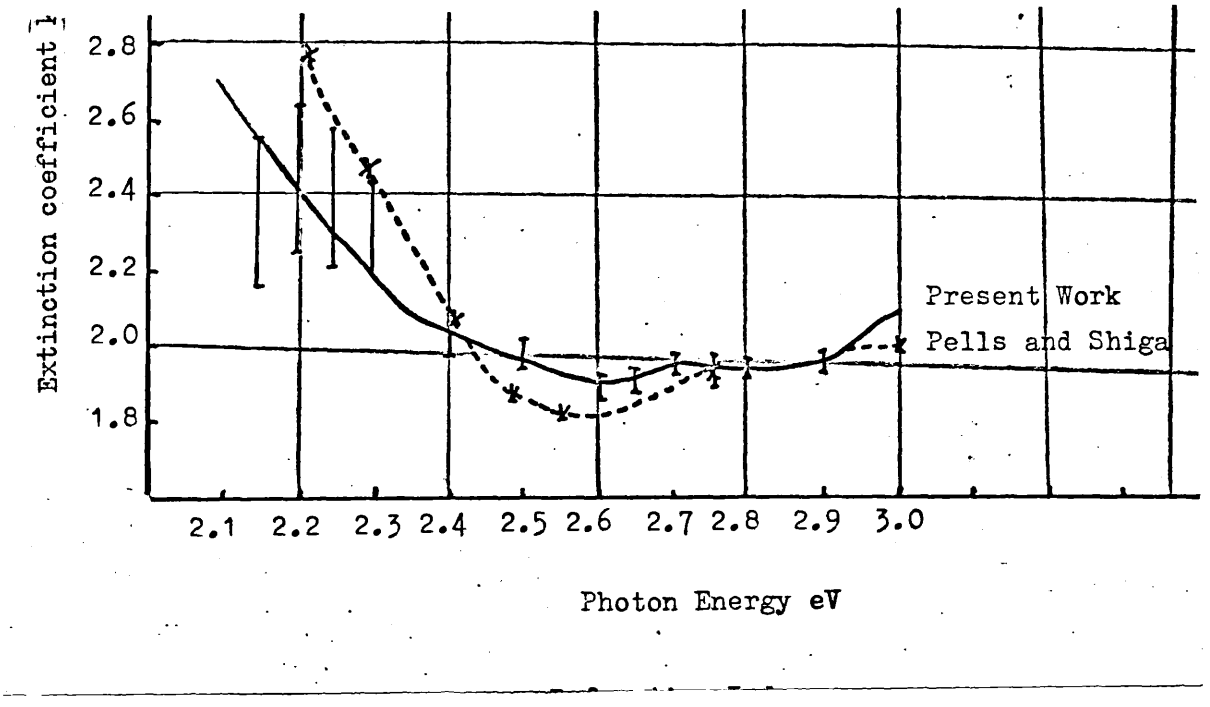

Figure 64. Extinction coefficient of gold.

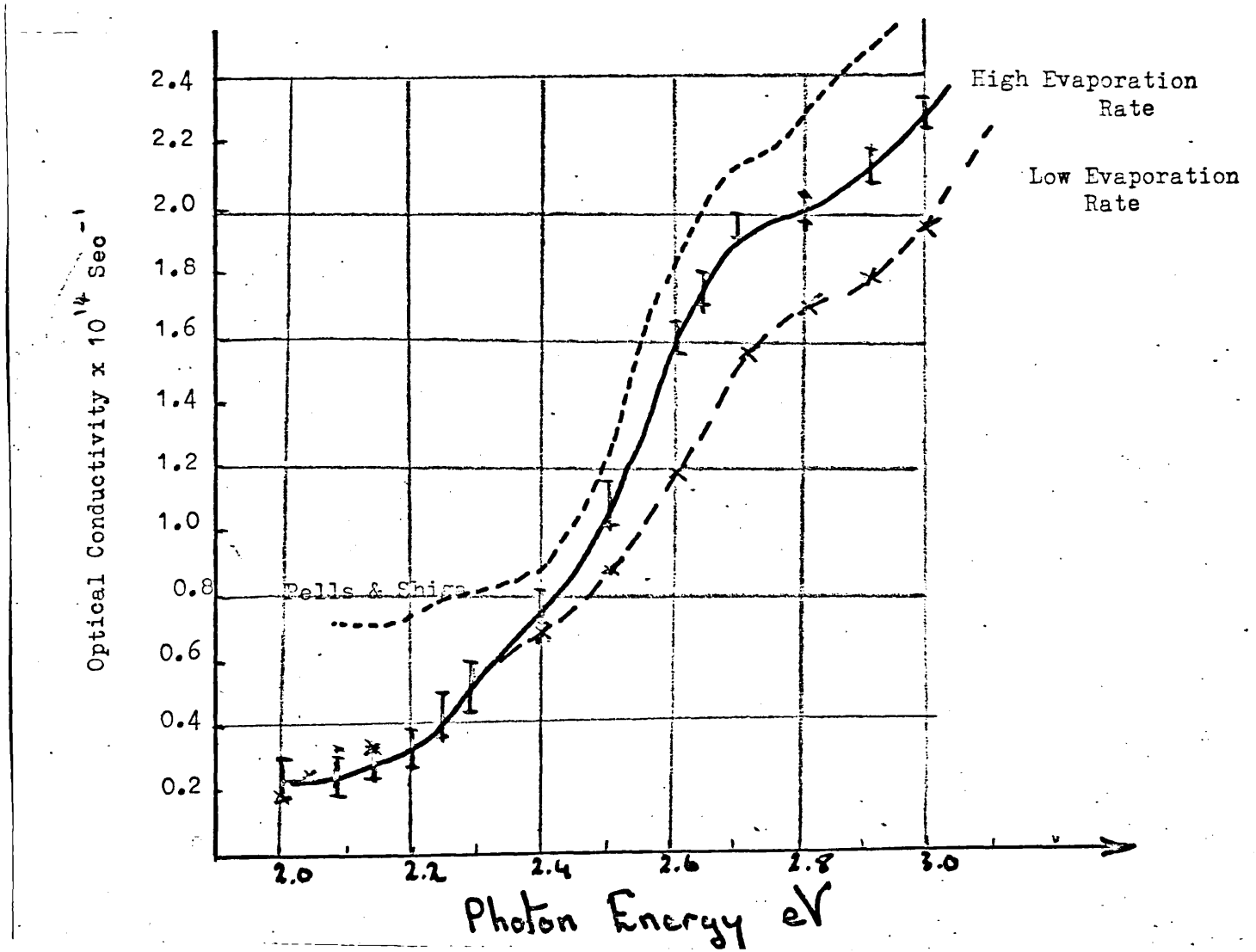

Figure 65. Optical conductivity of gold.

the reflectance ratio of a film having a thickness of $\sim 1400\text{Å}$ prepared by passing a current of 55 Amps for one minute through a tungsten helix loaded with 99.99% pure gold supplied by Johnson-Matthey Ltd. The n and k values obtained from these reflectance ratios are shown in figures 63 and 64, together with those of Pells and Shiga. Again a region of poor sensitivity was encountered and results had to be discarded. There is tolerable numerical agreement between the results obtained in this and those of Pells and Shiga: the n values obtained here are consistantly lower but the k values agree quite closely. Their results, however show a deeper minimum near 2.55 eV than that obtained in the present work.

7.9 The Optical Conductivity of Gold

Figure (65) shows the measured optical conductivity of gold. The results of Pells and Shiga are also shown together with the results obtained on a second gold film measured in the present work. The centre of the absorption edge measured in the present work coincides fairly well with the centre of the edge obtained by Pells, although the effective "widths" of the edges appear different. The general variation of the optical conductivities are in good agreement. A current of 50 Amps was passed for 90 seconds to yield a film of thickness $\sim 1400\text{Å}$. Again it is observed that the results on the film grown at the lower rate are further removed from the results obtained by Pells

than are those obtained on the first film discussed. No new structural detail for gold was observed in the optical conductivity curve. The theoretical interpretation of the optical conductivity curve of gold has been discussed by Pells.

7.10 Variation of Optical Constants of Gold and Copper with Evaporation Rate.

Levinstein (1949) has examined the structure of a large number of metals using both electron microscopy and electron diffraction. It was found that gold showed a marked preferred orientation when condensed on glass so that the type of effect discussed in 6.8 may be present. We note the slight shift in energy of the whole curve for the gold evaporated at the lower rate. Work by Duffendack (1943) showed that copper and gold may form agglomerates on condensation separated by interstices much smaller than the widths of the aggregates. The interstitial separation is likely to vary with evaporation rate, since the formation of aggregates depends on the surface mobility of atoms at the substrate on condensation and this in turn depends on the local temperature. Large interstitial separations will tend to produce films with low optical conductivity. Thus the observed variations in optical constants are not inconsistent with previous electron microscope studies.

CHAPTER VIII

CONCLUSIONS AND SOME SUGGESTED FURTHER WORK

This study of methods for the determination of optical constants has yielded a considerable amount of new information. Querry's solutions to the Fresnel reflectance equations have been critically examined and applied for the first time to measurements on metal surfaces. The existence of optimum angles of incidence for the determination of optical constants from reflectance measurements has been confirmed and their values estimated. New computer-based search techniques were established to accomplish this optimization. During this work, analytic equations to the boundaries in ($R_{\perp}$, $R_{//}$) space, outside which no real solutions to the Fresnel equations exist, have been established. It is noted in passing that Armaly et al (1972) have subsequently reported similar studies. They have used the same conditions as stated here and draw similar conclusions. Their work has not been as detailed as the studies made here. Perhaps the most important aspect of the optimization studies is the discovery of the large magnitude of errors in optical constants, arising from errors in reflectance measurements measured at angles well removed from optimum. In particular, the sensitivity of the normal incidence reflectivity spectrum to small changes in optical constants has been studied and conditions established for this spectrum to be sensitive to small changes in optical

properties. Work is at present being performed to determine whether optical constants of real metals fulfil these conditions.

Following this study new methods for the computation of optical constants from measured values of combinations of the reflection coefficients $R_{\perp}$ and $R_{//}$ at two angles of incidence were evolved and the sensitivity of these combinations to small changes in optical constants studied. Again the importance of working in optimum regions for the angles of incidence was established. In particular, the combination $\left(\frac{R_{\perp}}{R_{//}}\right)$ was studied in detail and the method applied experimentally to various metal surfaces. Further work in this field should enable even more sensitive determinations of optical constants to me made. For example, if the functions of $R_{\perp}$ and $R_{//}$ are measured at more than two angles of incidence then n and k may be determined more accurately because consistancy is required between additional sets of observables. Another possibility is that optical constants may be derived from the slopes of curves obtained by measuring $R_{\perp}$ and $R_{//}$ continuously over a range of angles of incidence. In addition it may also be possible to obtain optical constants from the slopes of dispersion curves of $R_{\perp}$ and $R_{//}$ measured under various conditions. The basic technique required for these calculations has been well established in Chapter III.

A reflectometer operating at near optimum conditions has been constructed and its sensitivity evaluated. In particular the choice of mirror material has been shown to be important.

A procedure has been evolved for the accurate alignment of the reflectometer. The main new features of the reflectometer are that only two non-standard mirrors are required, and the system was constructed for use with samples prepared and maintained in ultra-high vacuum. The preparation of clean surfaces by thermal evaporation in ultra-high vacuum has been discussed.

The optical constants of the rare earth metals terbium and gadolinium have been measured under what is considered to be the best conditions to date. Prior to this work no agreement had been obtained between different observers results in the visible part of the spectrum. In this work tolerable agreement has been obtained with the general trend of one of the three previous observers results. This therefore represents a step forward in the field of the study of the optical properties of rare earth metals. Apart from the general agreement with Hodgson's work, new structure in the optical conductivity curve of gadolinium has been observed. This structure can be accounted for fairly well on the basis of a very simple model developed in this work. Great care was taken to establish the existance of the observed structure and the possibility of systematic error was largely removed by repeated observation and comparisons with work on the same films carried out by different observers using different apparatus. Observations were carried out on terbium films and the measurements represent the first published data on this metal. The similarities

between the optical conductivity curves of terbium and gadolinium led to conclusions on the possible electronic configurations of the two metals. The good agreement between the simple theory and experimental results lends credibility to the energy band structure calculations used in the model. Difficulties were encountered in distinguishing between causes of differences in different observers results. The matter remains largely unresolved (and has been for decades). However, the obvious differences in surface preparation could be singled out as a major likely cause. It can, on the basis of the results obtained in this work, be stated that optical constants measured on films prepared under carefully maintained clean conditions and measured using optimized techniques yield new information on the rare earth metals terbium and gadolinium. This information is consistent with recent energy band calculations. In addition it was observed that the interpretation of the general shape of the rare earth optical conductivity curves could be made in terms of non-k-conserving transitions.

Additional work was carried out on copper and gold and reasonable agreement obtained with results of measurement using different techniques on surfaces prepared by different methods. New structure was observed in the optical conductivity curve of copper and this agreed extremely well with theoretical predictions based on energy band structure calculations. However, the results on copper and gold remain somewhat tentative. Further extensions of this work are desirable. The extension of the spectral range to

to infra-red regions should lead to new information particularly concerning the free electron behaviour of the metals. Low temperature measurements (at present being performed) may be expected to lead to fundamental information on the magnetic properties of the rare earths. Optimized techniques may also resolve the narrow transitions from the 4f levels. Because of the observed structure obtained in this work it is thought that studies at higher energy resolution should prove profitable, particularly in relation to 4f → 4f transitions. In view of the good agreement obtained with theory in this series of experiments it is felt that there is some justification for the re-evaluation of the optical constants of some other metals in the hope that a somewhat better agreement with theory may be obtained than has been observed in the past. Magneto-optical studies are at present being considered and the techniques established for optical constant determinations will be incorporated into such studies. However, in view of the discussion in Chapter VII, perhaps the most important future step to be taken is to perform experiments on single crystals of the rare-earth metals. This view has also been stated by Schuler. Coupled with accurate selection rules, experiments should be able to assign individual transitions to structure in the optical conductivity curves. At this stage we note that band structure calculations converge to better than 0.01 eV, and coupled with improved energy resolution, experiments on single crystals should provide a better experimental check

on the starting potential used in the band structure calculation than has yet been achieved. From the theoretical point of view it is to be hoped that band structure calculations for the remaining rare earth metals become available and that, at the time of calculation, the appropriate band symmetries are deduced. (Unfortunately this seems to be one of the very few fields where this knowledge is important). Work of the type performed by Mueller on the calculation of optical conductivities may also prove useful.

Thin film properties have not been discussed in this work and it is thought that such a study might prove worthwhile.

Throughout this work there has been a deficiency of information on the structure and condition of the surface being measured. Almost all other work on optical constants also suffers from this defect. The problems related to electron-optical surface studies are formidable. For example, the studies must usually be carried out in reflection and resulting diffraction patterns are of poor visibility. In general, specimens have to be removed from the ultra-high vacuum environment and placed in a conventional electron microscope. This inevitably leads to doubts concerning the correlation between properties as measured in the microscope and properties at the time of the optical measurements. The interaction of a high energy electron beam with the specimen surface is also likely to cause changes in the specimen surface. In recent years several new techniques for surface study have been developed.

The relevant new techniques may be summarized as follows. Low energy electron diffraction (L.E.E.D.) allows the first few layers of a surface to be studied using the diffraction pattern obtained from appropriately scattered electrons incident normally on the surface. Interpretation of the L.E.E.D. patterns is, at present, difficult. Reflection high energy electron diffraction (R.H.E.E.D.) allows the structure of the specimen surface to be studied to a greater depth. Glancing incidence high energy electrons are used to produce a diffraction pattern resulting from the first few atomic layers. This technique has been used to observe the absorption of oxygen on the surface of nickel. Auger electron spectroscopy is effectively a technique which can be used for the non destructive chemical analysis of surfaces. The technique depends on an energy analysis of electrons emitted from atoms by a radiationless process resulting from the rearrangement of orbital electrons after an electron has been removed from an inner shell. Systems which allow these studies to be carried out in ultra-high vacuum are now commercially available but to date there has been no attempt to perform optical experiments at the same time as the detailed surface analysis which is now possible.

ACKNOWLEDGEMENTS

I wish to acknowledge the help and encouragement received from colleagues over the last three years. In particular I wish to thank Dr. A.J. Taylor, Mr. N. Chandler and Mr. W. Hasaan who all have, at various times, been co-users of the U.H.V. equipment. Some of the work on sensitivities was done in conjunction with Dr's A.J. Taylor and R.F. Miller and more recently Mr. W. Hasaan. I acknowledge their help particularly with the collection of the large body of data used in the work. Dr. F.G. Kingston of the Department of Computing and Statistics, Royal Holloway College, was largely responsible for making the FORTRAN language intelligable to me. I wish to thank all the technical staff at Royal Holloway College for their patient help. In particular, I wish to thank Mr. G. Hayward who built most of the apparatus used in this work and who also produced some of the diagrams used here. Mrs. S. Hayward has typed this thesis from an almost illegible first copy and deserves sincere thanks.

My supervisor, Dr. R.F. Miller has been a constant source of encouragement and has provided me with many things to think about throughout this work. I wish to acknowledge the help given to me at the start of this work by the late Professor S. Tolansky. Finally I wish to thank my wife, Carolyn, for her tolerance and help particularly during the writing of this thesis.

REFERENCES

Armaly, B.F. Ochoa J.G. Look D.C. Applied Optics 11, 12, 2907 (1972)

Avery, D.G. Proc. Phys. Soc. B65, 425 (1965)

Bennet, H.L. Silver M. Ashley E.J. J.O.S.A. 53, 1089 (1963)

Blodgett, A.J. Spicer W.E. Phys. Rev. 146, 390, (1966)

Blodgett, A.J. Spicer W.E. Yu.A.C. "Optical properties and electronic structures of metals and alloys" ed F. Abeles North Holland (1966)

Bode, H.W. "Network analysis and feedbask amplifier design" Van Nostrand (1945)

Boukaert, L.P. Smoluchowski R., Wigner P. Phys. Rev. 50, 58, (1936)

Burdick, G.A. Phys. Rev. 179, 138, (1968)

Dimmock, J.O. Freeman A.J. Phys. Rev. letters 14, 1066, (1964)

Dimmock, J.O. Freeman A.J. "Optical properties and electronic properties of metals and alloys" ed F. Abeles North Holland (1966)

Dresselhaus, G. Solid St. Commun. 7, 419 (1969)

Drude, P. Ann. Physik. 1, 566, (1900)

Duffendack, O.S. Picard R.G. J. Appl. Phys. 14, 291, (1943)

Greenward, D.A. Proc Phys. Soc. A71, 585 (1958)

Harrison W.A. "Solid state theory" Magraw Hill (1970)
Heavens O. "Proc Phys Soc B65 658 (1952)
Heavens, O. "Optical properties of thin solid films" Butterworths (1959)

Hodgson, J.N. Cleyet B. J. PHYS. C. 2, 2, 97 (1969)

Humphreys- Owen, S.P.F. Proc. Phys. Soc. 77, 949 (1961)

Jackson, T. Phys. Rev. 178, 3, 949, (1969)

Keeton S.C. and Louks T. Phys. Rev. 168, 672, (1969)

References (Contd.)

Kittel, C. "Quantum Theory of Solids" Wiley (1963)

Kolb D.M. J.O.S.A. 62, 599, (1972)

Kress, K.A., Lapeyre. J.O.S.A. 60, 1681, (1970)

Kubo R. J. Phys. Soc. Japan 12 570 (1957)

Landau and Lipshiptz "Electrodynamics of continuous media" Perganon Press (1960)

Levinstein, H. J. Appl. Phys. 20 306 (1949)

Lorentz, H.A. "Theory of electrons" Teulner Leipzig (1906)

Miller R.F., Taylor A.J. J. Phys. D., 4, 1419, (1971)

Mott, N., Jones H. "Theory of the properties of metals and alloys" Oxford (1936)

Mueller F.M. and Phillips J.C. Phys. Rev. 157, 600, (1967)

Pells G.P. J. Sci. Instrum., 44, 997 (1967)

Pells G.P. Shiga M. J. PHYS. C. 2, 2, 1847 (1969)

Pells G.P. Shiga M. J. PHYS. C. 2, 2, 1835 (1969)

Petrakian J.P. J.O.S.A. 62, 3, 401, (1972)
Pierls R.E. "Quantum theory of solids" Oxford (1955)

Pincherle L. Reports on progress in physics, 13, 355 (1960)

Query M.R. J.O.S.A. 59, 876, (1969)

Query M.R. Curnutte B. Williams D. J.O.S.A. 59, 1299 (1969)

Roberts R.W. Brit. J. Appl. Phys. 14, 537 (1963)

Schuler C. "Optical Properties and Electronic properties of metals and alloys" ed F. Abeles (1966)

Schultz L.G. J.O.S.A. 44, 357 (1954)

Slater J.C. Phys. Rev. 51, 846, (1937)

Taylor A.J. Ph.D thesis London University (1972)

Tolansky S. "Multiple Beam Interferometry of surfaces and films" Dover (1970)

References (Contd.)

Wilkinson J.H. Numerische Mathematick 1,150 (1959)

Zener. C. Nature 132, 968 (1933)

Appendix 1.

Listing of subroutine GENAT (chapter 2)

```
      SUBROUTINE GENAT(RHO,RPE,RPA,THETA,SRRI,INT)
      COMMON RR,RI
  100 FORMAT(10A4HTEST)
      INT=1
      PROD=RR*RI
      WORST=0.
    1 CONTINUE
      GRPE=RPE+RHO
      DO 10 I=1,100
      GRPA=(RPA-ABS(RHO))+ABS(RHO)*FLOAT(I)/50.
      CALL SOLVE(GRPE,GRPA,THETA,SRR,SRI)
      IF(SRR.EQ.-2.) GO TO 30
      A1=PROD-SRR*SRI
      IF(A1.GT.0.) GO TO 10
      A1=ABS(A1)
      IF (A1-WORST) 10,10,2
    2 WORST=A1
      GO TO 10
   30 INT=-1
   10 CONTINUE
      RHO=-RHO
      IF(RHO.LT.0) GO TO 1
    3 CONTINUE
      GRPA=RPA+RHO
      DO 20 I=1,100
      GRPE=(RPE-ABS(RHO))+ABS(RHO)*FLOAT(I)/50.
      CALL SOLVE(GRPE,GRPA,THETA,SRR,SRI)
      IF(SRR.EQ.-2.) GO TO 40
      A1=PROD-SRR*SRI
      IF(A1.GT.0.) GO TO 20
      A1=ABS(A1)
      IF(A1-WORST) 20,20,4
```

```
    4 WORST=A1
      GO TO 20
   40 INT=-1
   20 CONTINUE
      RHO=-RHO
      IF(RHO.LT.0) GO TO 3
      DRRI=WORST*100./PROD
      RETURN
      END
```

Listing of subroutine ANGL (chapter 3)

```
      SUBROUTINE ANGL(CHECK,SOLVE,THETA1,THETA2,RHO1,RHO2,RR,RI)
C                RATIOS AND ANGLES OF INCIDENCE ARE INPUTED
C                     REAL AND IMAGINARY PARTS OF REFRACTIVE INDEX ARE RETURNED
C
C     SET TEST PARAMETER AND STARTING VALUE FOR PARALLEL COMPONENT
      TEST=1.0E+07
      RPA1=0.0000000
      RHO=-1.0000000000000000
C     SET STEP SIZE
       STEP=.01
      STEP=STEP*.1
   10 CONTINUE
C SEE IF ROUTINE HAS CONVERGED
      IF(TEST.LE..001) GO TO 40
C        RESET RPA AND CHECK THAT STILL IN RANGE
      RPA1=RPA1+STEP
       IF(RPA1.GT.1.) GO TO 50
C        CALCULATE RPE FROM INPUT RATIO
      RPE1=RPA1*RHO1
C SOLVE FOR N AND K AND VERIFY THAT STILL IN VALID REGION
      CALL SOLVE(RPE1,RPA1,THETA1,RR,RI)
      IF(RR.EQ.-2.) GO TO 70
C        CALCULATE RATIO AT SECOND ANGLE AND COMPARE WITH TEST PARAMETER
      CALL CHECK(THETA2,RPE,RPA,RR,RI)
```

```
      RHO=RPE/RPA
      A1=ABS(RHO2-RHO)
      IF(A1.LT.TEST) GO TO 20
      GO TO 30
C  SET NEW VALUE FOR TEST PARAMETER AND CONTINUE SEARCH
   20 TEST=A1
      GO TO 10
C     GO BACK TWO STEPS ADJUST STEP SIZE AND CONTINUE SEARCH
   30 RPA1=RPA1-2.0*STEP
      RPE1=RPA1*RHO1
      CALL SOLVE(RPE1,RPA1,THETA1,RR,RI)
      CALL CHECK(THETA2,RPE,RPA,RR,RI)
      RHO=RPE/RPA
      TEST=ABS(RHO2-RHO)
      STEP=.1*STEP
      GO TO 10
C     RETURN TO MAIN PROGRAM
   40 CONTINUE
      GO TO 60
   50 PRINT 200
  200 FORMAT(1X,'REFLECTION COEFF. OUT OF RANGE')
   60 CONTINUE
      GO TO 80
C SEE IF TEST POINT HAS CROSSED VALID REGION
   70 IF(TEST.EQ.1.0E+07) GO TO 10
      GO TO 30
   80 CONTINUE
      RETURN
      END
```

The optimum angle of incidence for determining optical constants from reflectance measurements

R. F. MILLER, A. J. TAYLOR and L. S. JULIEN

Department of Physics, Royal Holloway College, University of London, Englefield Green, Surrey

MS. received 9th July 1970

Abstract. The shape of the boundary enclosing analytical solutions to the generalized Fresnel reflectance equations for n and k in terms of reflectances and angle of incidence has been investigated and the optimum angle of incidence for experimental measurement determined to be 74°. The distribution of reflectance values for fixed n and k for which the method is accurate to within $\pm 0{\cdot}05$ has been deduced to be $n < 3{\cdot}0$ and $k < 3{\cdot}2$.

1. Introduction

In order to investigate the optical constants of metals, it was desired to determine n, the refractive index, and k, the extinction coefficient, by measuring the reflectances $R_\parallel$ and $R_\perp$ of light polarized respectively parallel and perpendicular to the plane of incidence, at an angle of incidence θ. The generalized Fresnel equations correlating these quantities have been solved analytically by Querry (1969) for all angles except 0° and 45° and can therefore be used to evaluate n and k as required.

Since the experimental method consists of measuring $R_\perp$ and $R_\parallel$ for a given θ, it is of interest (*a*) to determine which value or values of θ give the best sensitivity to changes in n and k, and (*b*) for what ranges of n and k the method is experimentally useful. In the following discussion, it is shown that Querry's analysis can be extended by examining the boundary values for $R_\perp$, $R_\parallel$ and θ which satisfy Fresnel's equations. The useful range of n and k to which the method can be applied is obtained by plotting $R_\perp$ and $R_\parallel$ for a series of fixed n and k, at the optimum θ.

2. Determination of the boundary, in ($R_\perp$, $R_\parallel$, θ) space, enclosing values which satisfy Fresnel's equations

Querry's solution to the Fresnel reflectance equations may be summarized as follows: Making the substitutions

$$F=\frac{(R_\perp+1)}{(R_\perp-1)} \tag{1}$$

$$G=\frac{(R_\parallel+1)}{(R_\parallel-1)} \tag{2}$$

and putting

$$Q=\frac{(F-G)\sin\theta\cot 2\theta}{GF+(1-F^2)\cos^2\theta-1} \tag{3}$$

$$P^2=-Q^2-2FQ\cos\theta-\cos^2\theta \tag{4}$$

into Fresnel's reflectance equations in the form

$$R_\perp=\frac{(Q-\cos\theta)^2+P^2}{(Q+\cos\theta)^2+P^2} \tag{5}$$

$$R_\parallel=R_\perp\frac{(Q-\sin\theta\tan\theta)^2+P^2}{(Q+\sin\theta\tan\theta)^2+P^2} \tag{6}$$

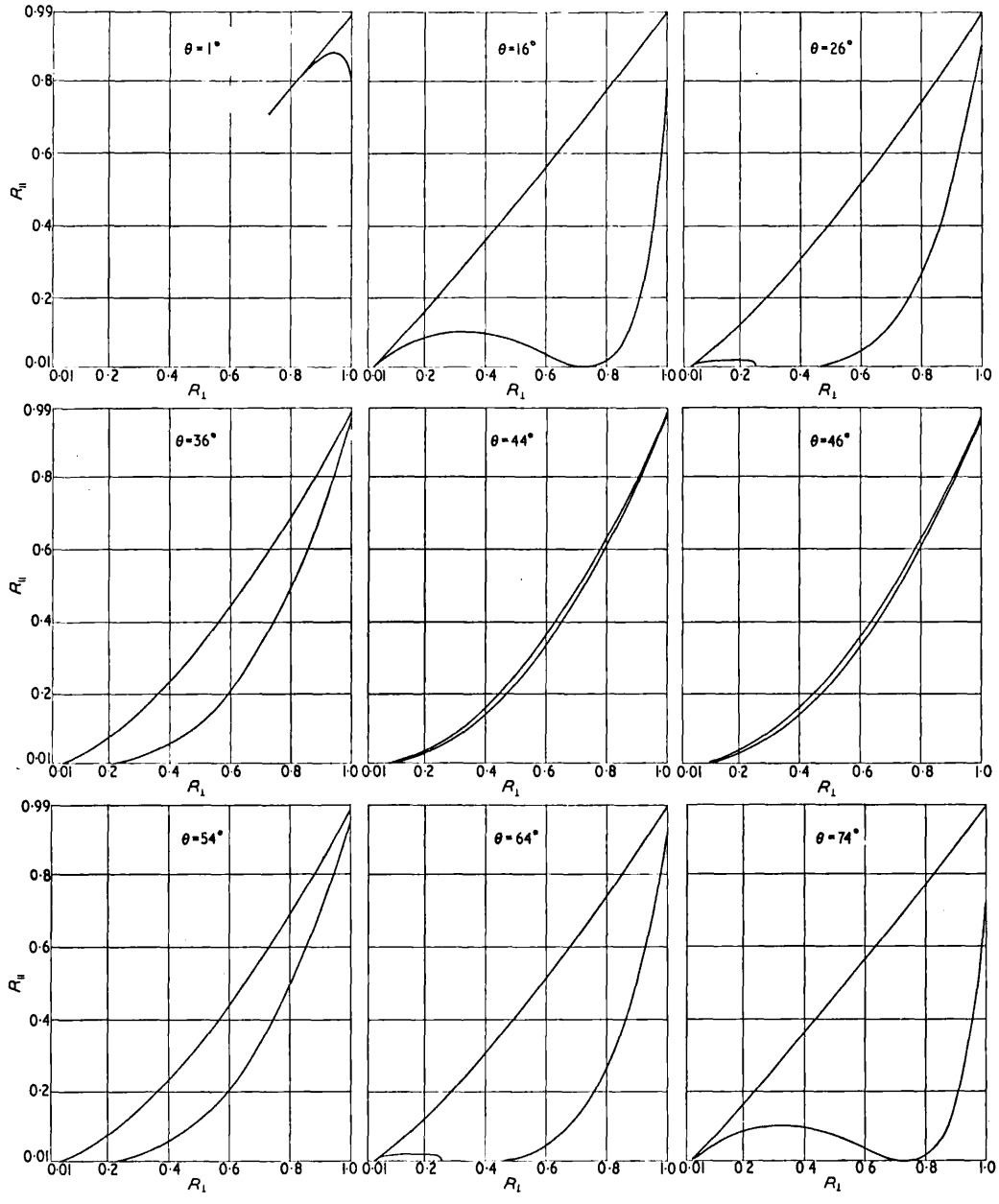

Figure 1. Boundaries enclosing all possible solutions to the Fresnel reflectance equations.

then

$$(Q^2-P^2)=n^2-k^2-\sin^2\theta \tag{7}$$

and

$$QP=nk \tag{8}$$

F and G are functions of the observables $R_{\perp}$ and $R_{\parallel}$ only. Therefore P and Q can be calculated for a given θ, and by substituting in (7) and (8), n and k are obtained.

Equation (3) shows Q to be real, and therefore real n and k are only obtained for real P in (8). It follows that solutions satisfying the Fresnel equations are only obtained for $P^2>0$. The condition $P^2=0$ delineates a boundary for these solutions, and it is readily shown that on one side of this boundary P is indeed imaginary, i.e. the boundary does not merely indicate a zero minimum value for P^2. Substituting for Q from (3) into (4) we get:

$$P^2=-\left(\frac{(F-G)\sin\theta\cot 2\theta}{GF+(1-F^2)\cos^2\theta-1}\right)^2-\frac{2F\cos\theta(F-G)\sin\theta\cot 2\theta}{GF+(1-F^2)\cos^2\theta-1}-\cos^2\theta. \tag{9}$$

Rearranging,

$$\begin{aligned}P^2=&G^2\{\sin^2\theta\cot^2 2\theta+F^2\cos\theta(\cos\theta-2\sin\theta\cot 2\theta)\}\\&+G[2F\cos\theta(\cos\theta-\sin\theta\cot 2\theta)\{(1-F^2)\cos^2\theta-1\}\\&+2F\sin\theta\cot 2\theta(F^2\cos\theta-\sin\theta\cot 2\theta)]\\&+F^2\sin^2\theta\cot^2 2\theta+2F^2\cos\theta\sin\theta\cot 2\theta\{(1-F^2)\cos^2\theta-1\}\\&+\cos^2\theta\{(1-F^2)\cos^2\theta-1\}^2.\end{aligned} \tag{10}$$

P^2 is thus a quadratic function of G, which changes sign when

$$aG^2+bG+c=0 \tag{11}$$

where a, b and c are the functions of F and θ indicated by equation (10). The solutions of (11), when transformed to the ($R_\perp$, $R_\parallel$, θ) space, via (1) and (2), bound the region for which all real n and k values may be obtained. This boundary also represents the condition $k=0$, since if

$$P^2=\tfrac{1}{2}[\{(n^2-k^2-\sin^2\theta)^2+4n^2k^2\}^{1/2}-(n^2-k^2-\sin^2\theta)]=0 \tag{12}$$

then

$$4n^2k^2=0 \tag{13}$$

and therefore

$$k=0 \tag{14}$$

i.e. the boundary values of $R_\perp$ and $R_\parallel$ are those corresponding to perfect dielectrics.

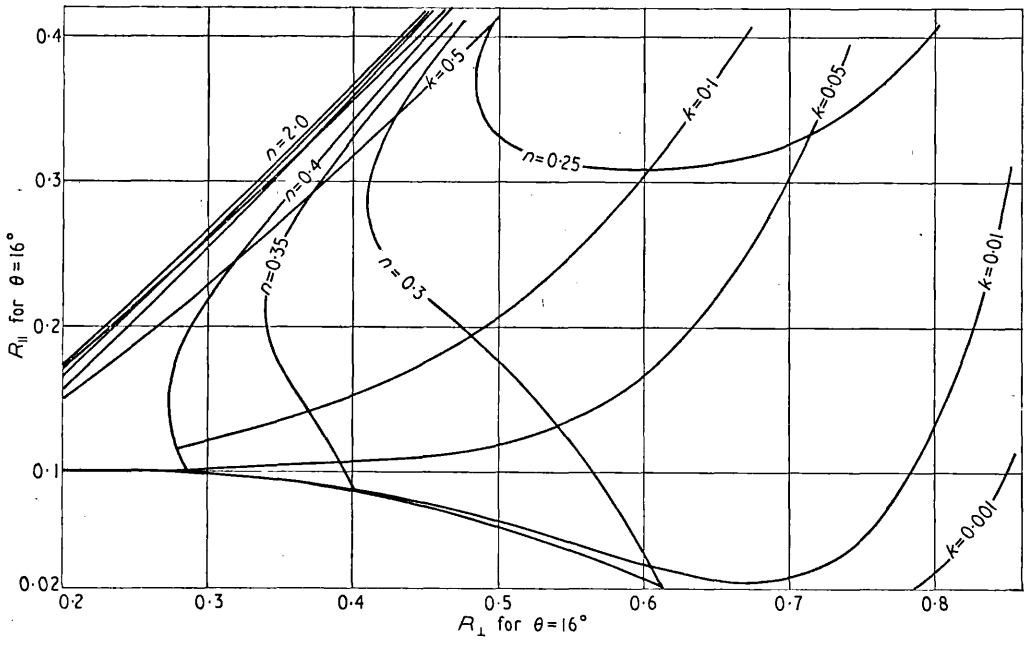

Figure 2. Distribution of n and k loci for $\theta=16°$.

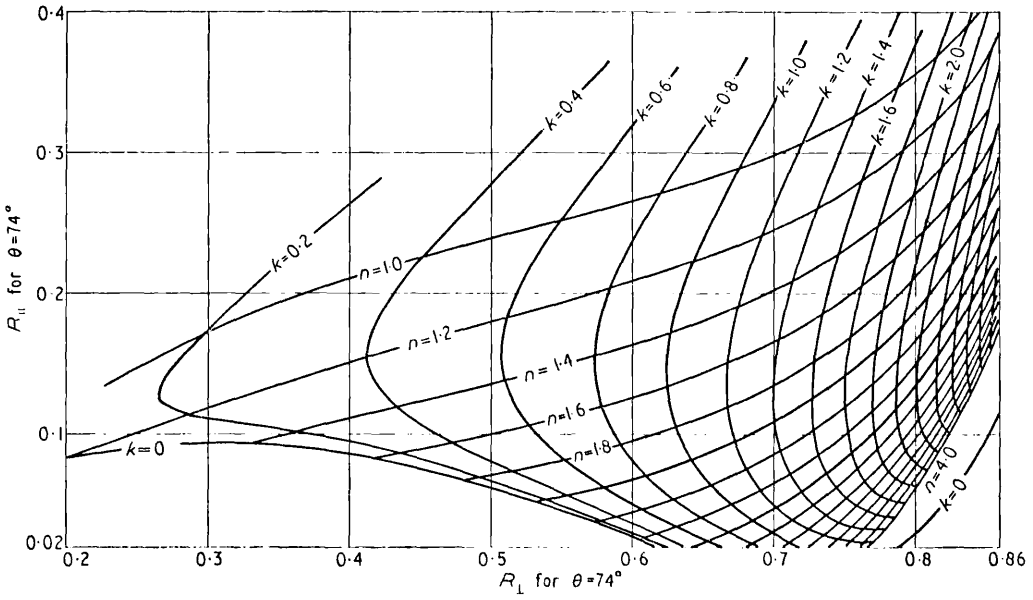

Figure 3. Distribution of n and k loci for $\theta=74°$.

Figure 1 shows sections of the boundary within which solutions for real n and k exist, for a range of angles θ between 0 and 90°, obtained by computer, using the $P^2 \geqslant 0$ condition. Loci have also been plotted of $R_{\perp}$ and $R_{\parallel}$ values for which n or k are fixed, and it is found that the distributions of these n and k loci are similar within the ranges $0° < \theta < 45°$ and $45° < \theta < 90°$ (figures 2 and 3).

The 'bunching' of n and k loci which occurs near the upper boundary for $0° < \theta < 45°$ changes to the lower boundary for $45° < \theta < 90°$ as θ passes through 45°. This bunching is associated with high values of n, and arises from the rapid approach of Q to $+\infty$ as Q changes sign:

$$(Q^2)_{P^2=0} = n^2 - k^2 - \sin^2\theta. \tag{15}$$

If the $Q>0$ boundary is close to one of the $P^2=0$ solutions, then $k^2 \to 0$ in (15). For $(Q^2)_{P^2=0}$ to go to $+\infty$, n^2 must tend to $+\infty$.

3. Sensitivity of n and k to $R_{\perp}$ and $R_{\parallel}$

All points $(R_{\perp}, R_{\parallel})$ generated by all possible n and k, for a given θ, are contained in the area enclosed by the $P^2=0$ boundary transformed to the $R_{\perp}$, $R_{\parallel}$ plane. The most sensitive measurements of n and k can therefore be performed for angles θ such that this area is largest, since the largest change in $R_{\perp}$ and $R_{\parallel}$ will be produced at these angles for a given change in n and k. Numerical integration shows that the maximum area, and therefore the best values of θ, occurs at 16° and 74° (figure 1). Empirical observation, rather than exact analysis, has previously indicated the most sensitive angle to be about 70° (Humphreys-Owen 1961). The area of the bounded region is in any case stationary with respect to θ at 16° and 74°, and therefore small changes in θ near these values will not greatly affect the results.

The distributions of n and k loci within the bounded regions at the best angles demonstrate the ranges of n and k to which the method may usefully be applied. In figure 2, for $\theta=16°$, the loci corresponding to values of n and k which are of practical interest are so close together that accurate determination from measurements of $R_{\perp}$ and $R_{\parallel}$ are impossible. Figure 3 shows 74° to be practically useful, the distribution being such that $R_{\perp}$ and $R_{\parallel}$ are sensitive to n and k values normally observed.

The precise range of n and k for which the method is acceptably sensitive can be found by determining the $R_\perp$ and $R_\parallel$ values for which an acceptable uncertainty in n and k produce a typical experimental uncertainty in $R_\perp$ and $R_\parallel$. Assuming n and k are required within $\pm 0{\cdot}05$, and the reflectances are measurable to within $\pm 0{\cdot}004$, the method is found to be applicable for $n < 3{\cdot}0$ and $k < 3{\cdot}2$. This region of usefulness is included in figure 3.

4. Conclusion

The shape of the boundary in ($R_\perp$, $R_\parallel$, θ) space, which includes all possible solutions for n and k from the Fresnel reflectance equations has been determined. Consequently the optimum angle θ, for the determination of n and k, from measurements of $R_\perp$ and $R_\parallel$ has been found to be 74°, and the useful ranges of n and k to which the method is applicable have been found to be $n < 3{\cdot}0$ and $k < 3{\cdot}2$.

Acknowledgments

We wish to thank Dr F. G. Kingston for assistance with the computing, and the Science Research Council for an SRC Studentship (AJT).

References

QUERRY, M. R., 1969, *J. Opt. Soc. Am.*, **59**, 876–7.
HUMPHREYS-OWEN, S. P. F., 1961, *Proc. Phys. Soc.*, **77**, 949–57.

J. Phys. D: Appl. Phys., 1971, Vol. 4. Printed in Great Britain

An analysis of the errors in optical constants obtained from reflectance measurements

R. F. MILLER, L. S. JULIEN and A. J. TAYLOR

Department of Physics, Royal Holloway College, University of London, Englefield Green, Surrey

MS. received 2nd March 1971

Abstract. For n and k in the ranges $1{\cdot}0 \leqslant n \leqslant 4{\cdot}0$, $1{\cdot}0 \leqslant k \leqslant 4{\cdot}0$, a computer study has been made of the way in which large errors in n and k may arise from errors in reflection coefficients, when the latter are measured at angles of incidence other than 74°. It is shown, as an example, that at near normal incidence errors in the product nk of $\pm 76\%$ are possible for $n=2{\cdot}00$, $k=3{\cdot}00$ when the measured reflection coefficient is in error by $\pm 0{\cdot}001$.

1. Introduction

In a previous paper (Miller *et al.* 1970) the general solution to the Fresnel reflectance equations (Querry 1969) was used to obtain an optimum angle of incidence, 74°, for measuring optical constants n and k from reflectance measurements. We now investigate in more detail how changes in the values deduced for n and k, produced by small changes in the measured reflection coefficients $R_\perp$ and $R_\parallel$, depend on the angle of incidence θ. $R_\perp$ and $R_\parallel$ are the respective reflection coefficients for incident light polarized perpendicular and parallel to the plane of incidence. The values of n and k were selected to be in the ranges $1{\cdot}0 \leqslant n \leqslant 4{\cdot}0$, $1{\cdot}0 \leqslant k \leqslant 4{\cdot}0$ (ie values relevant to the optical properties of metals in the visible region). Computer programs, written for a CDC 6600 computer, allowed a study of a large number of combinations of the parameters concerned. In particular, reflection coefficients measured near normal incidence have been shown to be insensitive to changes in n and k. Specific examples are used to illustrate our work.

2. Method for error investigation

The basis of the method is shown in figure 1. For an arbitrary value of θ, the bounded region in the $(R_\perp, R_\parallel)$ plane includes all values of $R_\perp$ and $R_\parallel$ which will give solutions to the Fresnel equations. A point P within this boundary is related to unique values of the optical constants n_0 and k_0 via the generalized Fresnel reflectance equations. If there is an uncertainty in the reflection coefficients of $\pm \Delta R$, then the extreme deviant values of optical constants, n and k, will be obtained from points lying on the perimeter of a square of edge $2\Delta R$ drawn with P as centre. These values of n and k are computed for 400 equally spaced points on the perimeter, assuming $\Delta R = \Delta R_\perp = \Delta R_\parallel$, independent of $R_\perp$ and $R_\parallel$.

The product of the optical constants nk was chosen as a suitable parameter for the investigation because of its relevance to band structure calculations. The fractional error in the product n_0k_0 for a point on the square is given by

$$\sigma = \frac{n_0k_0 - nk}{n_0k_0}.$$

Products nk for which σ took the largest positive and negative values were determined using a computer search technique. The values of σ associated with these nk products represent the maximum positive and negative errors resulting from uncertainties $\pm \Delta R$ in the reflection coefficients.

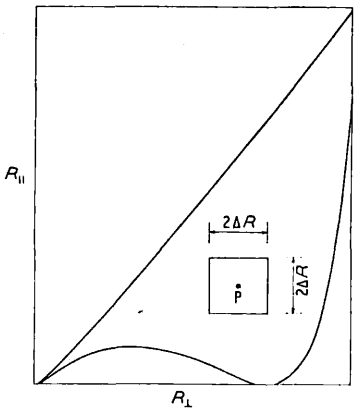

Figure 1. Boundary enclosing all possible solutions to the Fresnel reflectance equations, for an arbitrary value of θ.

3. Angular dependence of σ

The method described in the previous section was used to calculate σ for a large number of combinations of n_0 and k_0 in the ranges $1{\cdot}0 \leqslant n_0 \leqslant 4{\cdot}0$, $1{\cdot}0 \leqslant k_0 \leqslant 4{\cdot}0$ and for angles of incidence in the range $0 < \theta < \pi/2$ ($\theta \neq \pi/4$). We choose $n_0 = 2{\cdot}00$ and $k_0 = 3{\cdot}00$ to typify our results. The point $n_0 = 2{\cdot}00$, $k_0 = 3{\cdot}00$ lies close to the upper boundary of the valid region in ($R_{\perp}$, $R_{\parallel}$) space for values of $\theta < \pi/4$, and close to the lower boundary for values of $\theta > \pi/4$ (see figures 1, 2 and 3 of our previous paper).

Figure 2 shows the variation with θ of the largest positive and negative percentage errors in the product n_0k_0 for $\Delta R = \pm 0{\cdot}000\,05$. The latter value appears to be the best accuracy currently obtained in reflectance measurements. The two broad minima (figure 2) are in accordance with the results shown in our previous paper which clearly identified two regions of maximum sensitivity at $\theta = 16°$ and $\theta = 74°$. Furthermore, the shallower of the two minima occurs for large θ (shown in our previous paper to be that region of θ most sensitive for the determination of optical constants from reflectance measurements in the range $n_0 \leqslant 3{\cdot}0$ and $k_0 \leqslant 3{\cdot}2$). This broad shallow minimum indicates the existence of a large range of θ at which accurate determinations of n_0 and k_0 may be made. Catastrophic behaviour occurs as θ approaches 0° and 45°: σ increases significantly and, beyond the points at which the curves are discontinued, the possibility exists of values of $R_{\perp}$ and $R_{\parallel}$,

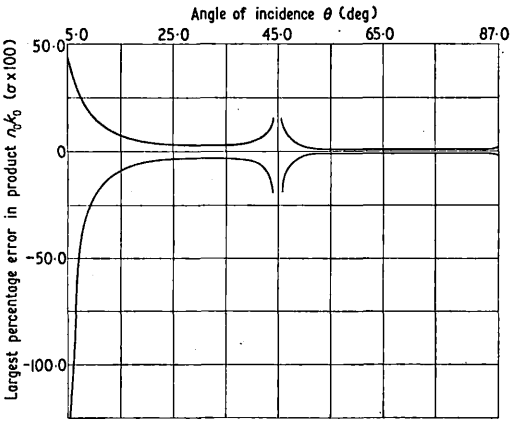

Figure 2. Angular dependence of the largest percentage error in the product n_0k_0 (ie $\sigma \times 100\%$, for $\Delta R = \pm 0{\cdot}00005$, $n_0 = 2{\cdot}00$, $k_0 = 3{\cdot}00$).

within the range $\pm \Delta R$, to produce non-valid solutions to the Fresnel equations (eg negative values for k).

For a modest degree of accuracy $\Delta R = \pm 0{\cdot}001$ and the same optical constants $n_0 = 2{\cdot}00$ and $k_0 = 3{\cdot}00$, figure 3 shows a shape similar to figure 2. However, the minima have sharpened and there is a dramatic increase in σ as θ approaches 0° and 45°. Parts of the

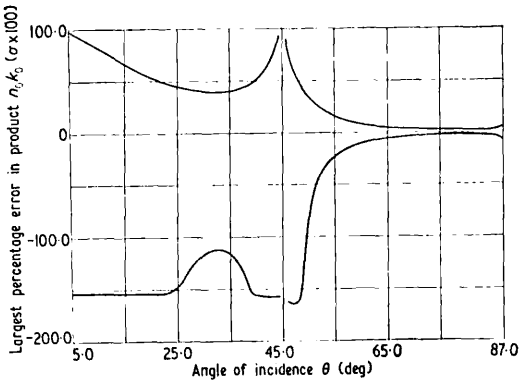

Figure 3. Angular dependence of the largest percentage error in the product n_0k_0 (ie $\sigma \times 100\%$, for $\Delta R = \pm 0{\cdot}001$, $n_0 = 2{\cdot}00$, $k_0 = 3{\cdot}00$).

negative curve in figure 3 show little variation with σ for $\theta < 45°$. In our previous paper (Miller *et al.* 1970) we have shown that for $\theta = 16°$ the point $n_0 = 2{\cdot}00$, $k_0 = 3{\cdot}00$ will be near to a boundary in the $R_\parallel$, $R_\perp$ plane. We showed that close to such a boundary $n \to \infty$, $k \to 0$. Further numerical work showed that the product nk passes through a maximum near this boundary. For $\Delta R = \pm 0{\cdot}001$, $n_0 = 2{\cdot}00$, $k_0 = 3{\cdot}00$, the perimeter of the test square approaches the $(R_\parallel, R_\perp)$ boundary and therefore the computer search technique locates the above maximum for certain values of θ. From figure 3 it is seen that the maximum in the nk product maintains a fairly constant value in this range of θ. Even so, the individual errors associated with n_0 and k_0 may still increase rapidly. For different values of n_0 and k_0 our work indicates that the general shape of the σ against θ curves remains the same, but differs only in detail.

Previous work has indicated that $\theta = 74°$ is the best angle for determining optical constants from reflectance measurements. In figure 4 the angular positions at which minimum σ

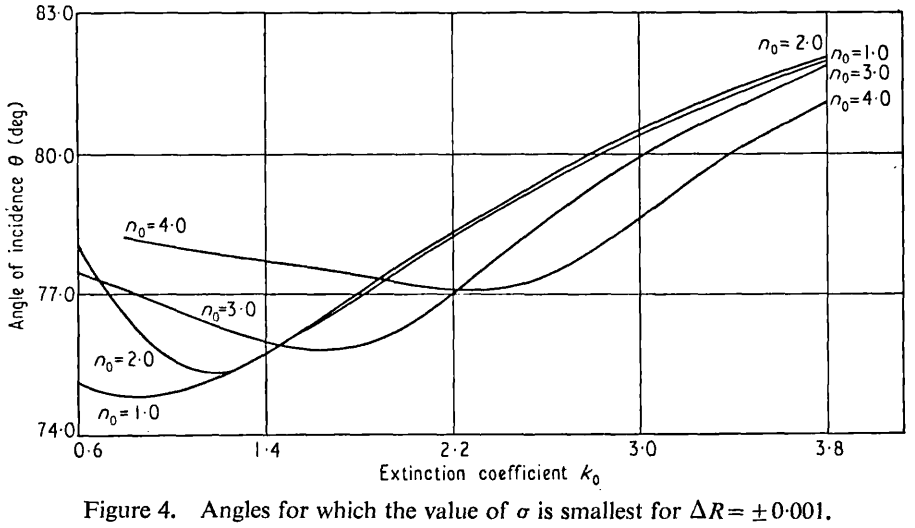

Figure 4. Angles for which the value of σ is smallest for $\Delta R = \pm 0{\cdot}001$.

occur have been plotted for a number of combinations of n_0 and k_0 for $\Delta R = \pm 0{\cdot}001$. If, for example, $n_0 = 2{\cdot}00$ and $k_0 = 3{\cdot}00$, figure 4 shows 80·5° to be the angle of incidence for greatest sensitivity. If this angle is used instead of the 'optimum' 74°, figure 3 shows the gain in accuracy in $n_0 k_0$ to be only 0·5%.

4. Variation of σ with ΔR

It was of practical interest to see how the value of σ varied with known errors ΔR in the reflection coefficient. Figure 5 shows the results of this study for the optimum angle 74° and for $n_0 = 2{\cdot}00$ and $k_0 = 3{\cdot}00$. For ΔR less than $\pm 0{\cdot}005$ the positive and negative portions of the graph are symmetrically placed about the line $\sigma = 0$, and σ varies linearly with ΔR. Above this value of ΔR the negative portion of the curve varies more rapidly, owing to the 'bunching' effect of the constant n and k curves shown on a plot of $R_\perp$ against $R_\parallel$ at 74° (see figure 3 of our previous paper).

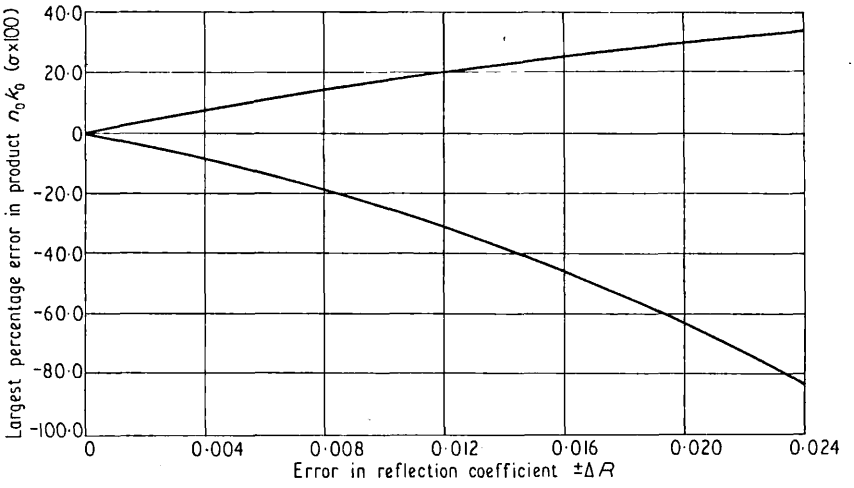

Figure 5. Variation of σ with ΔR for $n_0 = 2{\cdot}00$, $k_0 = 3{\cdot}00$, $\theta = 74°$.

5. Normal incidence measurements

In this section we shall consider the errors likely to occur in normal incidence reflection methods for obtaining the optical constants n_0 and k_0. Such methods measure one reflection coefficient for a range of optical frequencies ω. At normal incidence $R_\perp = R_\parallel = R$ and an ancillary relationship between R and ω is used to obtain n_0 and k_0. A suitable method is based on the Kramers–Kronig (KK) dispersion relation.

The equations relevant at normal incidence are

$$n_0 = \frac{1-R}{1+R-2R^{1/2}\cos\phi} \tag{1}$$

and

$$k_0 = \frac{-2R^{1/2}\sin\phi}{1+R-2R^{1/2}\cos\phi}. \tag{2}$$

These follow directly from the Fresnel reflectance equations if we express the complex reflection amplitude in the form $R^{1/2}\,e^{i\phi}$, where ϕ is the phase change on reflection. The dispersion relation between ϕ at a particular frequency ω_0 and the measured reflection coefficients may be expressed in the form (Bode 1945, p. 335)

$$\phi(\omega_0) = \frac{1}{\pi}\int_0^\infty \ln\left|\frac{\omega+\omega_0}{\omega-\omega_0}\right| \frac{\mathrm{d}}{\mathrm{d}\omega}(\ln R_\omega^{1/2})\,\mathrm{d}\omega. \tag{3}$$

The difficulties associated with this method are well known. Calculations based on the considerations of the foregoing sections show that values of n_0 and k_0 obtained by the KK method are subject to large inherent errors.

'Normal incidence' measurements are made at angles as high as 12° (Kress and Lapeyre 1970); at these angles it is assumed $R_\perp = R_\parallel$. For $\theta = 12°$, figure 3 shows that for a small change in reflection coefficient ($\Delta R = \pm 0{\cdot}001$) there is a large error in the product $n_0 k_0$. This means that the measured reflection coefficients are insensitive to the values of n_0 and k_0. The following numerical example will emphasize this fact.

When $n_0 = 2{\cdot}00$ and $k_0 = 3{\cdot}00$, the values of $R_\perp$ and $R_\parallel$ at $\theta = 12°$ are 0·563 and 0·548 respectively. If we assume $\Delta R = \pm 0{\cdot}001$, $R_\perp$ and $R_\parallel$ may become, as an extreme example, 0·564 and 0·547 respectively, and the resulting values of n_0 and k_0 will be 0·760 and 1·934. The corresponding value of σ expressed as a percentage is 76%, which shows that a change in n_0 and k_0 of this size will not change the value of the reflection coefficients by more than the uncertainty ΔR. Hence, there is a host of n_0 and k_0 values contained within the range determined by ΔR and therefore the substitution of measured reflection coefficients into equations (1), (2) and (3) are likely to lead to erroneous values of n_0 and k_0. The same calculation performed at $\theta = 74°$ gives σ, expressed as a percentage equal to 2·7%.

6. Conclusions

The angular dependence of the errors in optical constants ($1{\cdot}0 \leqslant n_0 \leqslant 4{\cdot}0$, $1{\cdot}0 \leqslant k_0 \leqslant 4{\cdot}0$) obtained from reflectance measurements has been determined, and shown to be large for angles well removed from the optimum region about 74°. In particular, it has been shown that reflectances measured at near normal incidence are inherently insensitive to wide variations in n_0 and k_0. This insensitivity may be a contributory factor to the wide discrepancies observed between the results obtained by near normal incidence and other methods for optical constants (Robin 1966, p. 208).

Acknowledgments

We wish to thank the Science Research Council for an SRC studentship awarded to one of us (AJT).

References

Bode, H. W., 1945, *Network Analysis and Feedback Amplifier Design* (New York: Van Nostrand).
Kress, K. A., and Lapeyre, G. J., 1970, *J. Opt. Soc. Am.*, **60**, 1681–4.
Miller, R. F., Taylor, A. J., and Julien, L. S., 1970, *J. Phys.* D: *Appl. Phys.*, **3**, 1957–61.
Querry, M. R., 1969, *J. Opt. Soc. Am.*, **59**, 876–7.
Robin, S., 1966, *Optical Properties of Metals and Alloys*, ed. F. Abelès (Amsterdam: North Holland).

J. Phys. D: Appl. Phys., Vol. 5, 1972. Printed in Great Britain. © 1972

A new computational method of obtaining optical constants from reflectance ratio measurements

R F MILLER, L S JULIEN and A J TAYLOR
Department of Physics, Royal Holloway College, University of London, Englefield Green, Surrey

MS received 25 August 1972

Abstract. A rapid accurate computational procedure has been devised for obtaining n and k from reflectance ratio values measured at two angles of incidence, θ_1 and θ_2. This technique has been used to study the sensitivity of the reflection ratio method, and it is shown that the errors are less than 2% in the product nk ($nk \leqslant 6$), when the reflection ratios are in error by $\pm 0{\cdot}005$, or θ_1 and θ_2 are in error by $\pm 0{\cdot}1°$, for measurements in the angular ranges $58° \leqslant \theta_1 \leqslant 67°$ and $80° \leqslant \theta_2 \leqslant 81°$.

1. Introduction

Optical constants n and k of bulk materials and opaque films can be obtained from measurements of the ratio $R_\perp/R_\parallel$ at two angles of incidence θ_1 and θ_2, where $R_\parallel$ and $R_\perp$ are the reflection coefficients for incident light polarized parallel and perpendicular to the plane of incidence. The experimental advantages of this method have been discussed by Avery (1952).

In addition, it should be pointed out that the method is particularly suitable for measurements on a sample in vacuum when the source and detector optics are outside the vacuum system. Whereas the windows must be calibrated for most other methods of obtaining n and k under these conditions, this is not necessary for the reflection ratio method, because the optical geometry is identical for each component in the ratio, provided that the light passes normally through nondichroic windows.

Although Avery's original graphical method has been improved (Miller and Taylor 1971), the processing of the experimental data by this means in order to obtain n and k can be inconvenient and tedious, especially if a full-sensitivity study is required. Kolb (1972) has obtained an analytical solution for the ratio method, and we have also derived such a solution, but both are computationally longer and more complicated than the method described below.

We have developed a computational procedure for obtaining n and k from measured reflection ratios which is rapid, accurate and convenient, and which enables the sensitivity of the reflection ratio method to be studied.

2. The computational procedure

The procedure is based on the analytical solutions to the generalized Fresnel reflectance equations (Querry 1969). Querry's analysis enabled equations for n and k to be written in

terms of $R_\parallel$, $R_\perp$ and one angle of incidence, θ. Figure 1 shows two bounded regions in $(R_\parallel, R_\perp, \theta)$ space enclosing all possible solutions to the reflectance equations for two angles of incidence, θ_1 and θ_2 (Miller *et al* 1970). Let us suppose that the ratios $(R_\perp/R_\parallel)_{\theta_1}$ and $(R_\perp/R_\parallel)_{\theta_2}$ are measured at θ_1 and θ_2. These ratios are the slopes of lines 0A and 0B passing through the origins of the $(R_\parallel, R_\perp)$ diagrams for θ_1 and θ_2 respectively. Consider the line 0A of slope $(R_\perp/R_\parallel)_{\theta_1}$. Each point on this line within the enclosed region corresponds to a different (n, k) pair given by solutions to the Fresnel reflectance equations. The measured ratio $(R_\perp/R_\parallel)_{\theta_2}$ may be used to isolate a unique (n, k) pair in the following way. Pairs of (n, k) values at θ_1 are used to generate a fan of lines such as 0C, 0D, 0E, 0F of figure 1(*b*).

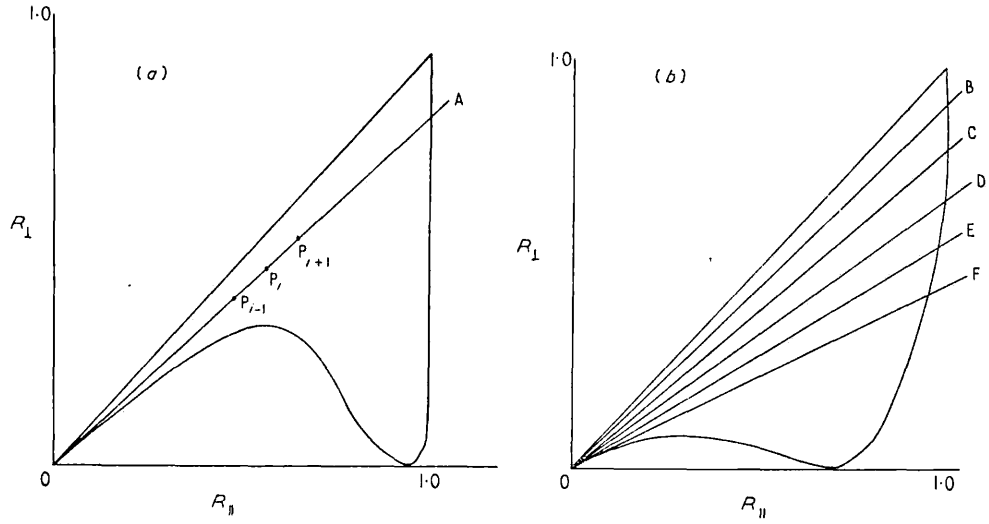

Figure 1. Bounded regions in $(R_\parallel, R_\perp, \theta)$ space for two angles of incidence, θ_1 and θ_2, showing lines of slope equal to reflection ratios.

Each line has a different slope $R_\perp/R_\parallel$, and only one (0B) will correspond to the measured ratio $(R_\perp/R_\parallel)_{\theta_2}$. The (n, k) pair generating this line is the required solution. This method of solving the reflection ratio equations is particularly convenient for digital computation.

Starting at the origin 0 on the line 0A, values of n and k are calculated at a number of equispaced points $P_1, P_2, P_3, \ldots, P_i, \ldots, P_j$ along 0A, and for each point the slope of the line at θ_2 is computed. The calculation proceeds in this way until the quantity δm, defined as | calculated slope − observed slope $(R_\perp/R_\parallel)|_{\theta_2}$, starts to increase. If the calculation has proceeded to a point P_i on 0A, and at this point there is an increase in δm, the calculation is then restarted at a point P_{i-2} on 0A. The step size, defined as the length 0A/j, is reset to 0A/fj, where f is an arbitrary reduction factor—in our case we put $f=10$. The calculations are allowed to proceed until δm reaches some arbitrarily small value, and are then stopped. The point on 0A at which calculation ceases thus corresponds to the desired solutions for n and k. In practice, the calculation is stopped when δm is approximately equal to the experimental error in the measured ratios. An example of the speed and accuracy of this computational procedure is demonstrated for $n=2$, $k=3$ by setting the limit on δm to 0·001. The initial step size was 0·01 of the $R_\perp$ axis, and we set $f=10$. Solutions accurate to 1 part in 3000 were obtained in less than 0·05 s (computing time required for a CDC 6600 computer using a FORTRAN IV compiler).

3. The sensitivity of the reflection ratio method

The rapid convergence of this computational procedure allows a comprehensive study to be made of the sensitivity of the reflection ratio method. In a previous paper (Miller *et al* 1971), a method for studying the sensitivity of n and k to $R_\parallel$ and $R_\perp$ was developed. We used a quantity σ which was defined as the fractional error introduced into the product nk by known errors in $R_\parallel$ and $R_\perp$. For the ratio method the definition of σ remains the same but the coefficients $R_\parallel$ and $R_\perp$ are replaced by the ratios $(R_\perp/R_\parallel)_{\theta_1}$ and $(R_\perp/R_\parallel)_{\theta_2}$. We have used these previously described computational techniques to investigate the variation of σ with changes in the quantities θ_1, θ_2, $(R_\perp/R_\parallel)_{\theta_1}$ and $(R_\perp/R_\parallel)_{\theta_2}$ for combinations of n and k in the ranges $1 \leqslant n \leqslant 4$, $1 \leqslant k \leqslant 4$.

Table 1. Optimum regions of θ_1 and θ_2 for an error of $\pm 0{\cdot}005$ in the reflection ratios $(R_\perp/R_\parallel)_{\theta_1}$ and $(R_\perp/R_\parallel)_{\theta_2}$

Value of n	Value of k	Optimum region for θ_1	Optimum region for θ_2	Error in product nk (σ%)
low; ~ 1	high; ~ 4	$56° \leqslant \theta_1 \leqslant 69°$	$80° \leqslant \theta_2 \leqslant 85°$	$< 2{\cdot}0$
mod; ~ 2	mod; ~ 3	$58° \leqslant \theta_1 \leqslant 69°$	$78° \leqslant \theta_2 \leqslant 85°$	$< 1{\cdot}0$
high; ~ 4	low; ~ 1	$50° \leqslant \theta_1 \leqslant 69°$	$70° \leqslant \theta_2 \leqslant 85°$	$< 0{\cdot}5$

Table 2. Optimum regions of θ_1 and θ_2 for an error of $\pm 0{\cdot}1°$ in the angles of incidence

Value of n	Value of k	Optimum region for θ_1	Optimum region for θ_2	Error in product nk (σ%)
~ 1	~ 4	$50° \leqslant \theta_1 \leqslant 67°$	$77° \leqslant \theta_2 \leqslant 80°$	$< 1{\cdot}0$
~ 2	~ 3	$50° \leqslant \theta_1 \leqslant 67°$	$74° \leqslant \theta_2 \leqslant 81°$	$< 1{\cdot}0$
~ 4	~ 1	$50° \leqslant \theta_1 \leqslant 68°$	$75° \leqslant \theta_2 \leqslant 81°$	$< 1{\cdot}0$

The results are summarized in tables 1 and 2. The quantity σ was calculated for all combinations of θ_1 and θ_2 in the ranges $50° \leqslant \theta_1 \leqslant 69°$ and $70° \leqslant \theta_2 \leqslant 85°$ for each (n, k) pair. In compiling table 1 we assumed errors of $\pm 0{\cdot}005$ in the two ratios and no errors in θ_1 and θ_2 for each (n, k) pair. An error of $\pm 0{\cdot}005$ in the ratios should not be too difficult to achieve experimentally. We were interested in obtaining optimum values for θ_1 and θ_2 for each (n, k) pair. However, there is no dramatic variation of σ with θ_1 and θ_2; and so we chose to represent as optimum those regions of θ_1 and θ_2 in which measurement at any combination of angles would give smaller values of σ than those shown. The value of σ at a given θ_1 and θ_2 was found to be approximately proportional to the known error in the reflection ratios. The range of ratio errors investigated was $\pm 0{\cdot}005$ to $\pm 0{\cdot}01$. The data shown in table 2 were obtained by assuming no errors in the reflection ratios and errors in θ_1 and θ_2 of $\pm 0{\cdot}1°$. Again there was no dramatic variation of σ with θ_1 and θ_2 when these were in error by $\pm 0{\cdot}1°$, but σ was found to vary strongly with θ_1 and θ_2 when these were in error by $\pm 0{\cdot}5°$. For an error in θ_1 and θ_2 of $\pm 0{\cdot}5°$ the optimum regions for θ_1 and θ_2 were shorter in range than those for $\pm 0{\cdot}1°$. As an example, for $n=2$, $k=3$ and $\sigma < 2{\cdot}5\%$; the optimum region for θ_1 was $50° \leqslant \theta_1 \leqslant 60°$, and for θ_2 the single value $\theta_2 = 76°$ was obtained.

If we compare the above reflection ratio method with a direct measurement at one angle, we see that the former has a greater inherent sensitivity to n and k. For example,

figure 5 of Miller *et al* (1971) shows $\sigma \simeq 11{\cdot}1\%$ for $n=2$, $k=3$ when the individual coefficients $R_\parallel$ and $R_\perp$ are in error by $\pm 0{\cdot}005$. Table 1 shows $\sigma < 1\%$ for the same (n, k) pair when the ratios are in error by $\pm 0{\cdot}005$. In addition, the ratio method allows a considerable choice for optimum angles compared with the more rigid requirements of the coefficient method.

4. Conclusions

A new method has been devised for computing n and k from the reflectance ratio data measured at two angles of incidence. The method is convenient, accurate and economical in terms of computer time. This computational procedure has been used to examine the sensitivity of the reflection ratio method, and it is found that errors of less than 2% may be attained in the product nk for $nk \leqslant 6$, when the reflection ratios are in error by $\pm 0{\cdot}005$, or θ_1 and θ_2 are in error by $\pm 0{\cdot}1°$, for measurements in the angular ranges $58° \leqslant \theta_1 \leqslant 67°$ and $80° \leqslant \theta_2 \leqslant 81°$.

The reflection ratio method is thus shown to have a rather greater inherent sensitivity to n and k, and a wider range of optimum angles than a method which measures reflection coefficients $R_\parallel$ and $R_\perp$ at one optimum angle.

References

Avery D G 1952 *Proc. Phys. Soc.* B **65** 425–8
Kolb D M 1972 *J. Opt. Soc. Am.* **62** 599–600
Miller R F, Julien L S and Taylor A J 1971 *J. Phys.* D: *Appl. Phys.* **4** 1100–4
Miller R F and Taylor A J 1971 *J. Phys.* D: *Appl. Phys.* **4** 1419–25
Miller R F, Taylor A J and Julien L S 1970 *J. Phys.* D: *Appl. Phys.* **3** 1957–61
Querry M R 1969 *J. Opt. Soc. Am.* **59** 876–7